MAGNETOTELLURIC IMAGING OF DÜZCE FAULT

by

Tülay Kaya

B.S., Geophysical Engineering, İstanbul University, 2000

Submitted to Kandilli Observatory and Earthquake
Research Institute in partial fulfillment of the
requirements for the degree of
Master of Science

Graduate Program in Geophysics
Boğaziçi University

2007

MAGNETOTELLURIC IMAGING OF DÜZCE FAULT

APPROVED BY

Yrd. Doç. Dr. S. Bülent Tank.....
(Thesis Supervisor)

Prof. Dr. Niyazi Türkelli….....

Prof. Dr. İlyas Çağlar…….....

DATE OF APPROVAL.....

Dedicated to my father

ACKNOWLEGEMENTS

Firstly, I would like to thank my supervisor Assist. Prof. Dr. S. Bülent Tank for his support and valuable advices throughout this thesis. He has always been helpful for me to understand every part of this study and interpret correctly my results. I'm grateful his useful comments, discussions and improvement of my knowledge about this subject.

The data used in this study were obtained from a joint project, funded by TUBITAK, as collaboration between Boğaziçi University, Kandilli Observatory and Earthquake Research Institute and National Academy of Sciences of Ukraine. I thank to Assoc. Prof. Dr. M. Kemal Tunçer, who is director of the project in Turkish side, for the opportunity to join the field works of this project and use the data of the project. I also thank to him for his suggestions in this research.

I would like to thank to members of the Boğaziçi University, Geophysics Department for their support during my academic life here. My special thanks to Tuna Eken, Birsen Can, Fatih Bulut, Özlem Kurtuluş, Elif Tolak, and Gonca Örgülü for their friendship and encouraging comments during my thesis. They have always been ready to help me whenever I need.

I should express my deepest gratitude to my family. My father and my mother, Cemal and Bahar, and my sisters, Türkan and Nuray provided me with their love and endless patient. They have always encouraged me to overcome the problems and make progress in life. I will always be grateful to them.

During the first field campaign of data acquisition, Alberta University provided this project with two MT recorders. I also want to thank, Prof. Dr. İlyas Çağlar from İstanbul Technical University and Martyn Unsworth from Alberta University for this support.

ABSTRACT

MAGNETOTELLURIC IMAGING OF DÜZCE FAULT

The highly active North and East Anatolian Faults have contributed to the occurrence of the most destructive earthquakes in Turkey for years. One of these devastating earthquakes, Düzce earthquake, took place on Düzce fault, at the western part of the North Anatolian Fault (NAF) at northwestern Turkey, in 1999. Seismological studies related to Düzce earthquake (Mw: 7.2) revealed the phenomena that the western and eastern parts of the epicenter ruptured with distinct velocities from each other. It is obvious that with their capability to identify the electrical resistivity variation between the neighboring structures and the efficiency in resolving the electrical resistivity structure of the Earth, electromagnetic (EM) methods have been preferred for solving geophysical problems. For this reason during this study, one of the EM methods, magnetotelluric (MT) method was applied with the aim of finding a relationship between the phenomena related to Düzce earthquake and electrical properties of the region. Magnetotelluric data within the frequency range between 320-0.0005 Hz were acquired along two parallel profiles at the west and the east of Düzce earthquake's epicenter, DW and DE, respectively. Both profiles crossed Düzce basin and Düzce fault in the north and NAF in the south. DW contained twelve sites and was ~35 km long while DE contained 11 sites and was about ~40 km long. The effects of galvanic distortions produced by near surface inhomogeneities were retrieved from MT data by Groom and Bailey (1989) decomposition and as a result of this analysis geo-electric strike was found to be N72˚E and N70˚E for DW and DE, respectively, which is consistent with the geology. MT data were analyzed for both TE (electrically polarized), and TM (magnetically polarized) modes by two-dimensional inversion modeling using the code developed by Ogawa and Uchida (1996). According to the inversion results of the DW and DE, some outcomes which may explain the velocity phenomena existing on the western and eastern parts of the Düzce earthquake's epicenter obtained.

ÖZET

DÜZCE FAYININ MANYETOTELLÜRİK GÖRÜNTÜLENMESİ

Aktivitesi yüksek olan Kuzey ve Doğu Anadolu Fayları yıllarca Türkiyedeki yıkıcı depremlerin oluşumuna neden olmuştur. Bu harabedici depremlerden biri olan Düzce depremi 1999 yılında Türkiye'nin kuzeybatısında, Kuzey Anadolu Fayı'nın (KAF) batı kısmında, Düzce fayı üzerinde meydan geldi. Düzce depremi (Mw: 7.2) ile ilgili sismolojik çalışmalar episantr'ın batı ve doğu kısımlarının birbirinden farklı hızlarla yırtıldığı olgusunu açığa çıkardı. Çok açıktır ki, yakın yapılar arasındaki özdirenç değişimini belirlemedeki kapasiteleri ve yerin özdirençli yapılarının çözümlenmesindeki etkinlikleri ile elekromanyetik (EM) yöntemler jeofizik problemlerinin çözümünde tercih edilmiştir. Bu nedenle bu çalışma esnasında, Düzce depremi ile ilgili olgu ve bölgenin elektriksel özellikleri arasında bir ilişki bulmak amacıyla EM yöntemlerden biri olan manyetotellürik (MT) yöntem uygulandı. Düzce depreminin episantr'ının sırasıyla batısında ve doğusunda iki paralel profil boyunca, DW ve DE, 320-0.0005 Hz frekans aralığında MT verisi toplandı. Her iki profilde kuzeyde Düzce fayını ve Düzce havzasını, güneyde ise KAF'ı kesti. DE ~40 km uzunlukta ve 11 istasyon içerirken DW ~35 km uzunluktaydı ve 12 istasyon içerdi. Yüzeydeki bozucu etkilerden kaynaklanan galvanik bozunmanın etkisi Groom ve Bailey (1989) ayrıştırması kullanılarak MT verisinden atıldı ve bu analiz sonucunda bölge jeolojisi ile uyumlu sırasıyla DW ve DE için K72˚D'lik ve K70˚D'lik doğrultular bulundu. MT verisi Ogawa ve Uchida (1996) tarafından geliştirilen iki-boyutlu (2-B) evirme (ters çözüm) modellemesi kullanılarak hem TE (elektriksel olarak polarize olmuş) hem de TM (manyetiksel olarak polarize olmuş) modu için analizİ yapıldı. DW ve DE profillerinin ters evrişim sonuçlarına göre, Düzce depremi episantr'ının batı ve doğu kısımlarında meydana gelen hız olgusunu açıklayabilecek bazı sonuçlar elde edildi.

TABLE OF CONTENTS

LIST OF FIGURES

LIST OF TABLES

LIST OF SYMBOLS / ABREVIATIONS

EM	Electromagnetic
TDEM	Time Domain EM
FDEM	Frequency Domain EM
NAF	North Anatolian Fault
DF	Düzce fault
DW	Western profile
DE	Eastern profile
Hz	Hertz (Unit of frequency)
Re	Real
Im	Imaginary
1D	One-dimensional
2D	Two-dimensional
3D	Three-dimensional
TE	Transverse electric mode (**E** polarization)
TM	Transverse magnetic mode (**B** polarization)

E	Electric field
H	Magnetic field
B	Magnetic induction
D	Dielectric displacement
J	Electric current density
m	Empirical coefficient
f	Frequency
T	Period
z	Depth
k	Wave number
Z	Plane wave impedance
T_x and T_y	Magnetic transfer functions

R	Rotation matrix
R^T	Transpose of R
C	2x2 distortion tensor
g	Site gain (in Groom and Bailey Decomposition)
t	Twist (in Groom and Bailey Decomposition)
e	Shear (in Groom and Bailey Decomposition)
m	Model parameter
F(m)	Model response
d	Measured data
S	Data misfit
w	Weighting matrix
A	Jacobian matrix
h	Roughening vector
C	Roughening matrix
G	Static shift
sm	Smoothing parameter
ss	Static shift parameter

ρ	Electrical resistivity
Ωm	Electrical resistivity unit (Ohm-m)
σ	Electrical conductivity
ρ_{w}	Electrical resistivity of the fluid
ρ_a	Apparent resistivity
Φ	Porosity
ε	Dielectric permittivity
μ	Magnetic permeability
∇	Nabla Symbol
ω	Angular frequency
φ	Phase
δ	Skin Depth
λ	Wavelength
κ	Skewness

μ	Bahr's 1D parameter
η	Regional skew
Σ	Bahr's 2D parameter
ϕ	Rotation angle
α	Decomposition parameter

1. INTRODUCTION

The Earth has been the fundamental subject for the geoscientists for years. Different methods are used to reveal the construction of the Earth in applied geophysics such as gravity, magnetic, electric, seismic, and electromagnetics. These methods determine the physical properties of the Earth by searching the distinct physical parameters. In this thesis, an electromagnetic method the magnetotelluric method is used to depict the electrical resistivity distribution of a target region.

The Earth materials may have electrical resistivities ranging from a few to several thousands Ωm (Haak & Hutton, 1986). Electromagnetic (EM) methods, based on the variations of the electric (**E**) and magnetic (**H**) fields within the Earth, aim to display the electrical resistivity (ρ) (or its inverse, conductivity (σ)) distribution of the Earth. With their capability to identify resistivity variations between the neighbouring structures and their knowledge of the resistivity structure of the Earth materials, EM methods have been used for a long time for different purposes. Some applications of EM methods are a mineral exploration, groundwater surveying, geothermal resource investigations, contaminated land mapping, detection of geological and artificial cavities, and location of geological faults (Tezkan, B., 1999).

Due to the source used in the application of EM methods, they are classified as natural source or controlled source EM methods. The natural EM signals come from variety of sources such as electrical storms in the lower atmosphere and solar activities in magnetosphere (Vozoff, 1972). Some examples of the sources used in controlled source EM methods are radio transmitters, electric dipoles and loop of wire. Besides the source type classification, EM methods are also classified as Time Domain EM (TDEM) or Frequency Domain EM (FDEM) methods according to data acquisition systems used.

Magnetotelluric method (MT) is a natural source EM method because of the fact that its source comes from the natural EM signals. Although MT data are acquired in the time domain, they are processed in the frequency domain. MT methods have broad field of applications for solving geophysical problems, such as investigation of geothermal systems (Wei *et al.*, 2001; Çağlar and İşseven, 2004), active volcanoes (Ogawa *et al.*, 1999; Aizawa, *et al.*, 2005), petroleum exploration (Constable *et al.*, 1998), crustal structures (Wannamaker and Doerner, 2002; Gürer *et al.*, 2004), marine studies (Key and Constable, 2002), mantle properties (Jones, 1999; Simpson, 2002), and active faults (Unsworth *et al.*, 2000; Tank *et al.*, 2005; Ritter *et al.*, 2005).

It is obvious that once the devastating Düzce earthquake (1999) occurred on the Düzce fault, north branch of the North Anatolian Fault (NAF) at NW Turkey, Düzce fault has attracted the attention of many geophysicists. On the evidence of some studies, basic parameters of Düzce earthquake and Düzce fault (DF) have been obtained (Ayhan *et al*., 2001; Akyüz *et al.*, 2002; Bürgmann *et al.*, 2002; Bouchon *et al.*, 2002; Çakır *et al.*, 2004; Birgören *et al.*, 2004). Bouchon *et al.*, (2002), Bouin *et al.*, (2004), and Birgören *et al.*, (2004) claimed that the western and eastern parts of the epicenter ruptured with distinct velocities from each other. This velocity property of Düzce earthquake also observed during İzmit earthquake in 1999 (Bouchon *et al.*, 2002) had an initiative effect on this study because using the relation between seismic velocity and electrical conductivity of the Earth's subsurface, MT method could be a new approach to the velocity phenomena occurred on during Düzce earthquake.

In this thesis, MT method has been applied to demonstrate resistivity variations on both sides of the Düzce earthquake's epicenter which may explain the occurrence of the large rupture velocity difference between the western and eastern parts of the epicenter during the earthquake (Bouchon *et al*., 2002; Bouin *et al*., 2004; Birgören *et al*., 2004). Firstly, at the western side of the epicenter, MT data have been obtained along the profile crossing the Düzce basin, DF and NAF from the north to the south. The data were processed to obtain electrical resistivity distribution of the region versus depth from the observed apparent resistivity and the phase values. The results of the western profile (DW)

such as transition from the resistive layer to the conductive subsurface structure beneath the Düzce basin supported the straightness of the claim concerning Düzce earthquake. After this, the acquisition of data from the eastern profile (DE) became more essential. The data set obtained on the DE profile being parallel to the DW, has been processed by the same method.

In the following chapter, Chapter 2, basic information concerning MT method is given. In Chapter 2, firstly, source types of MT method are presented with the theory on which MT method is based. Some basic concepts in MT method such as MT impedance tensor, apparent resistivity, phase, skin depth and induction vectors are determined in this part. Chapter 2 also contains information about the decomposition and dimensionality estimation of the MT data with different approaches, and theory of the data modeling. In the following chapter, tectonics and geology of the study area, Düzce, and additionally, previous studies about Düzce earthquake are given. Chapter 4 demonstrates an important part that is field procedure including instrumentation. Every step of MT method mentioned in Chapter 1 was applied to the observed data obtained from both DW and DE profiles in Chapter 5. These steps include acquisition, interpretation and process of observed data to obtain the models of the subsurface structure. Subsequently, in Chapter 6, outcomes of the application of MT method on DW and DE profiles are discussed and in conclusion, the results of this study are given.

2. THE MAGNETOTELLURIC (MT) METHOD

The MT method is termed as a passive electromagnetic method since it uses natural source with the aim of imaging the subsurface of the Earth together with the electrical resistivity distribution of the medium. These natural electromagnetic (EM) sources in the frequency range of 10^{4} Hz to 10^{-4} Hz originates from plasma processes in the Earth's magnetosphere and the lightning discharges in the Earth's ionosphere (Vozoff, 1972, 1991; Kaufman and Keller, 1981).

Putting the MT method into practice starts with recording electric (**E**) and magnetic (**H**) fields on the Earth's surface since it depends on the variations of these fields in the subsurface (Tikhonov, 1950; Cagniard 1953). Due to this dependency, by using amplitude, phase, and directional relationships between the observed electric and magnetic fields, the electrical resistivity of the subsurface can be found out, and the target structure beneath the Earth can be imagined by means of the MT method (Vozoff, 1972, 1991).

One major advantage of the MT method is that the subsurface structure can be deduced from depth of a few tens of meters to several kilometers without needing unnatural sources or including huge environmental effects (Vozoff, 1972). But yet, for two-dimensional (2D) case that will be given in detail in progressing parts some distortions may occur on the MT data; such as due to the effects of galvanic distortions, the profile may have an orientation apart from the geo-electric strike or perpendicularity between the electric and magnetic fields may deviate. However, these undesirable effects can easily be removed from observed data by several methods (Groom and Bailey, 1989; Chave and Smith, 1994; McNeice and Jones, 2001). The outcome of the decomposition gives the undistorted observed data which is used in modeling of the subsurface.

The summarized methodology of the MT method including definition of its source type, theory of the method, procedure to obtaining undistorted variables of the Earth from observed values after eliminating undesirable effects, and revealing the model of the target subsurface structure will be described in this chapter.

2.1. Source and Theory of the MT Method

2.1.1. Source of the MT Method

Due to the dependency on the natural fields, the MT method does not require power supplies or current control systems such as other EM methods. Natural signals of the EM fields come from a tremendous variety of sources and frequency ranges. However, in this range, the MT method attends to the part of frequency range and two source regions, atmosphere and magnetosphere (Vozoff, 1972, 1991). From 10 KHz to 1 Hz, natural source of the MT fields are formed by the worldwide electrical thunderstorm activities existing within the lower atmosphere. On the other hand, at frequencies below 1 Hz, the major part of the fields due to current flow in the ionized layers surrounding the Earth is constituted by solar activity in the magnetosphere (Kaufman and Keller, 1981; Vozoff, 1972, 1991).

The region of space taking part behind the bow shock, the interface between the Sun and Earth's magnetic field deflecting the solar wind, and covering the Earth is called magnetosphere (Figure 2.1.). This region contains some gasses such as oxygen and nitrogen. These gasses decreasing in density with elevation have a significant feature. They are ionized by ultraviolet and other solar radiation. While the high-pressure below 100 km forces the ions to recombine, above 100 km, charged particle density increases rapidly up to about 250 km. When it reaches 250 km elevation, charged particle density starts to decline again, and at the same time, pressure and particle density decreases.

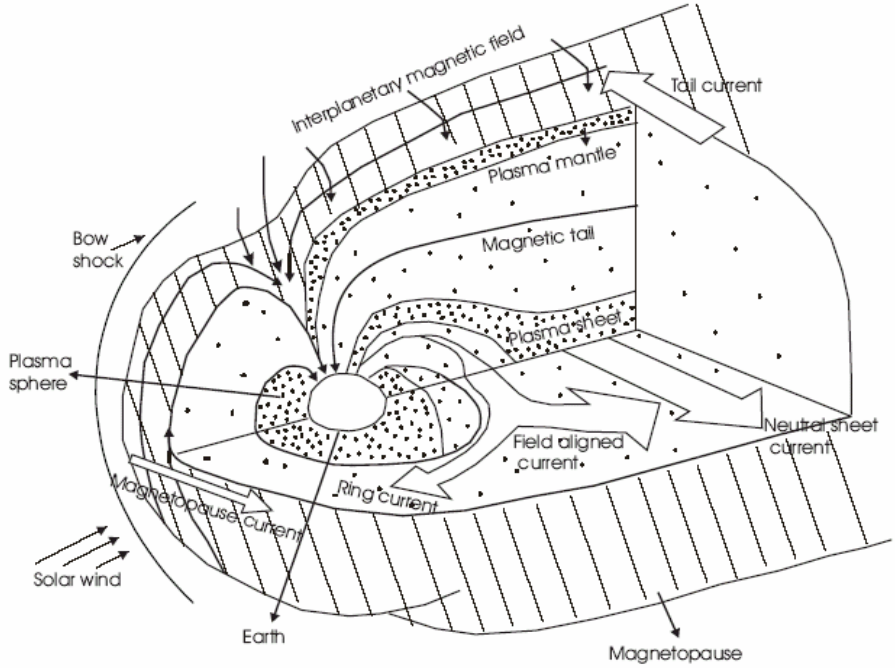

Figure 2.1. The magnetospheric current systems (redrawn from Vozoff, 1991).

This region (about from 100 km to 250 km) having relatively high electrical conductivity is called the ionosphere (Vozoff, 1991). Within the magnetosphere including the atmosphere together with ionosphere, the main magnetic field is trapped by solar wind, plasma flow of the Sun. In respect to the properties of the magnetosphere, the interaction of the Earth's magnetic field with the solar wind causes micropulsations as source of the MT method (Kaufman & Keller, 1981).

Another natural source of the MT method is lightning activities, which are meteorological events. Lightning generally consists of sequences of discharges for the frequency ranging from 10^4 to 1 Hz. These discharge sequences are called as strokes and 3 or 4 of them constitute flashes. Occurrence frequency of lightning flashes around the world varies between nearly 100 and 1000 Hz and this is an important component of EM fields (Vozoff, 1972, 1991).

Near 1 Hz, observing accurate MT data is not easy because the signals coming from the frequency range greater than 1 Hz (or less than 1 Hz) lose their effect near this frequency. MT method penetrating so deep and getting the information related to deeper subsurface structures gives better estimation of subsurface.

2.1.2. Theory of the MT method

In order to understand the MT method, electromagnetic waves must be perceived completely. An electromagnetic wave propagates in space with its two components, which are the electric (**E**) and magnetic (**H**) fields. These two components are functions of time (or frequency), and have special positions in space. They oscillate at right angles to each other and to the direction of propagation defining a plane wave (Vozoff, 1991; Kaufman & Keller, 1981; Cagniard, 1953; Tikhonov, 1950). Schematic electromagnetic wave is shown in Figure 2.2 with its two components, magnetic and electric fields.

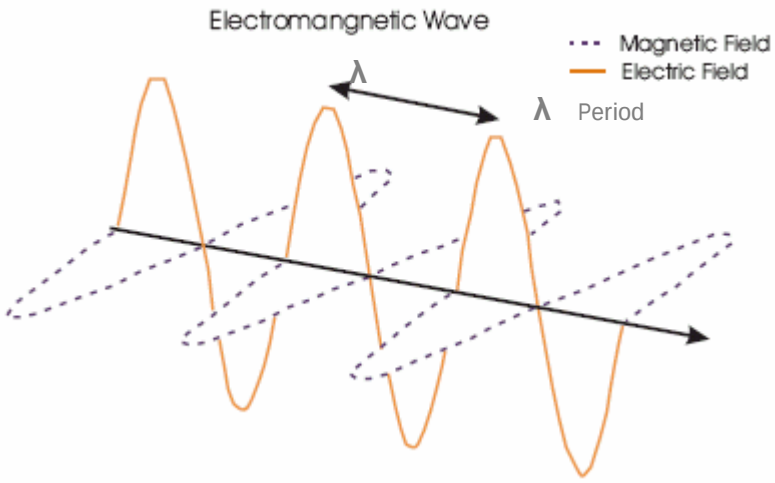

Figure 2.2. An electromagnetic wave with its components.

Wherever signals come from (natural or artificial sources), it is supposed that the electromagnetic (EM) waves, penetrating into the Earth's crust, behave almost like plane waves (Vozoff, 1972, 1991). While some parts of these waves reflect once they reach to

the surface, some of them propagate vertically downward into the Earth (Cagniard, 1953). Figure 2.3 represents the propagation of EM waves into the Earth.

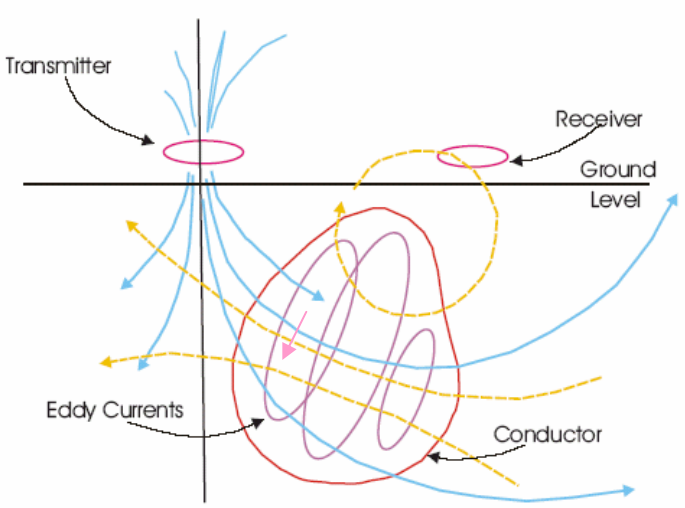

Figure 2.3. EM induction theory. Primary and secondary fields are represented by straight blue and dashed yellow lines, respectively.

According to EM induction theory, the signal coming from transmitter (red field of Figure 2.3) diffuses through the Earth to the electrical conductor. At that moment, time varying primary magnetic field (blue field) from transmitter interacts with the conductor and induces telluric (Eddy) currents, obeying Faraday's law shown by purple colored line. These currents obeying Ampere's law cause the conductor to transmit a secondary time varying magnetic field which propagates to the receiver (yellow field). Due to these properties of EM wave, after measuring the electric and magnetic variations simultaneously on the Earth's surface, the electrical resistivities of the subsurface structure (as a function of frequency) can be obtained by applying some computation techniques on observed data (Tikhonov, 1950; Cagniard 1953; Kaufman and Keller, 1981).

The electric current induced in the subsurface is not only related to the EM field, but also to the electrical resistivity of the rocks. The resistivity of a rock is significantly

depending on the connectivity and contents of the pore volume between the minerals, high saturation of fluids, and partial melting of rock. The relation between the rock resistivity, fluid conductivity, and the porosity for saturated porous materials is given by Archie's well-known empirical law (Archie, 1942):

$$\rho = \rho_w . \Phi^{-m} \tag{2.1}$$

where ρ and ρ_w are the electrical resistivities of the rock and the fluid, respectively, m is the empirical coefficient determined from the laboratory experiments, Φ is the porosity, (Archie, 1942).

The crustal rocks having a wide range of electrical resistivity with the changes of permeability, porosity, fluid saturation, and salinity are significant for the MT method since they are sensitive to the structural state of rocks (Table 2.1).

Table 2.1. Resistivity values of several crustal rocks (Jones, 1999).

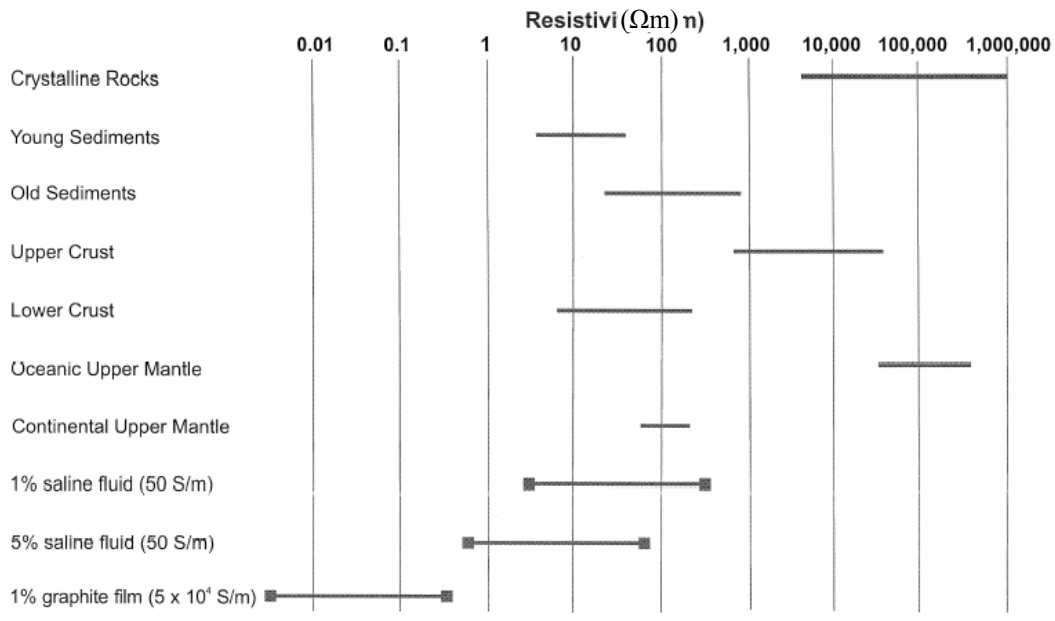

2.2. Basic Principles of the MT Method

2.2.1. Maxwell's Equations and EM Wave Equations

2.2.1.1. Maxwell's Equations. The basic concept of Maxwell's work was that the equations describing the behavior of electric and magnetic fields were consistent with the equation of charge conservation only for a steady state. After this realization he eliminated this inconsistency for the case of nonsteady state by adding a new term, which involves time rate of change of the electric field **E** (Maxwell, 1864; Ward and Hohmann, 1987). Therefore, Ampere's law, varying electric field produces a magnetic field, was proved by Maxwell with addition of this new term, $\partial \mathbf{D}/\partial t$. The relation between the electric and magnetic fields and their connection with charges (at the rest and moving) are seen in the Table 2.2.

Table 2.2. Relation of electric and magnetic fields with charges.

Electric Fields caused by	Magnetic Fields caused by
Stationary charges	Moving charges
Changing magnetic field	Changing electric field

Consequently, Maxwell reconstructed the laws of Faraday, Ampere and Gauss and put them into four equations to convey the construction of the electromagnetic waves. Today, these four equations are known as Maxwell's equations. Maxwell's equations in time-domain for an isotropic and homogenous media can be expressed as (Ward and Hohmann, 1987):

$$\nabla \times \mathbf{E} = -\frac{\partial \mathbf{B}}{\partial t} \tag{2.2}$$

$$\nabla \times \mathbf{H} = \mathbf{J} + \frac{\partial \mathbf{D}}{\partial t} \tag{2.3}$$

$$\nabla \cdot \mathbf{D} = \rho \tag{2.4}$$

$$\nabla \cdot \mathbf{B} = 0 \tag{2.5}$$

In the equations above, **E** is the electric field intensity in V/m, **H** is the magnetic field intensity in A/m, **B** is the magnetic induction in Wb/m^2 or Tesla, **D** is the dielectric displacement in C/m^2, **J** is electric current density in A/m^2, and ρ is the electric charge density C/m^3 (Ward and Hohmann, 1987).

The first equation of Maxwell comes from Faraday's law, which says that the time varying magnetic field produces an electric field. The subsequent one is Ampere's law corrected by Maxwell by adding the time varying electric field (**D**=ε**E**). This equation demonstrates that magnetic field intensity result from effects of the current density and time varying electric field. The other two equations, Gauss's law for the electric field (2.4) and for the magnetic field (2.5), give the boundary conditions of electromagnetic fields. Such as, the third equation of Maxwell implies that electric fields have source coming from electric charges, whereas the last equation underlines that there is no source charges for magnetic fields. The connections between the electric and the magnetic fields with medium parameters are given as;

$$\mathbf{D} = \varepsilon\, \mathbf{E}, \tag{2.6}$$

$$\mathbf{B} = \mu\, \mathbf{H}, \tag{2.7}$$

$$\mathbf{J} = \sigma\, \mathbf{E}. \tag{2.8}$$

In these equations, ε is the dielectric permittivity F/m, σ is the electric conductivity S/m, and μ is the magnetic permeability H/m. The third equation of Maxwell, equation 2.4,

is representation in the static case but in dynamic case, in which the MT theory is interested, it becomes,

$$\nabla \cdot \mathbf{E} = 0 \tag{2.9}$$

Once Fourier transformation is applied to equations 2.2 and 2.3 and constitutive relations (2.6, 2.7, and 2.8) are used, Maxwell equations in the frequency domain are obtained as;

$$\nabla \times \mathbf{E} = -i\omega\mu\mathbf{H} \tag{2.10}$$

$$\nabla \times \mathbf{H} = (\sigma + i\varepsilon\omega)\mathbf{E} \tag{2.11}$$

$$\nabla \cdot \mathbf{E} = 0 \tag{2.12}$$

$$\nabla \cdot \mathbf{B} = 0 \tag{2.13}$$

2.2.1.2. EM Wave Equation To obtain electromagnetic wave equation in time domain for the electric and the magnetic fields, firstly the curl of equations (2.2) and (2.3) is taken (Ward and Hohmann, 1987).

$$\nabla \times (\nabla \times \mathbf{E}) = \nabla \times \left(-\frac{\partial \mathbf{B}}{\partial t} \right) \tag{2.14}$$

$$\nabla \times (\nabla \times \mathbf{H}) = \nabla \times \left(\mathbf{J} + \frac{\partial \mathbf{D}}{\partial t} \right) \tag{2.15}$$

By substituting the equations (2.6), (2.7), and (2.8) into the equations (2.14) and (2.15), and rearranging them it is obtained that;

$$\nabla \times (\nabla \times \mathbf{E}) = -\mu \frac{\partial}{\partial t}(\nabla \times \mathbf{H}) \tag{2.16}$$

$$\nabla \times (\nabla \times \mathbf{H}) = \sigma \nabla \times \mathbf{E} + \varepsilon \frac{\partial}{\partial t}(\nabla \times \mathbf{E}) \tag{2.17}$$

Due to the quantities $\nabla \times \mathbf{E}$ and $\nabla \times \mathbf{H}$ given in the equations (2.2) and (2.3), respectively, equations (2.16) and (2.17) are converted to (Ward and Hohmann, 1987);

$$\nabla \times (\nabla \times \mathbf{E}) = -\mu\varepsilon \frac{\partial^2 \mathbf{E}}{\partial t^2} - \mu\sigma \frac{\partial \mathbf{E}}{\partial t} \tag{2.18}$$

$$\nabla \times (\nabla \times \mathbf{H}) = -\mu\varepsilon \frac{\partial^2 \mathbf{H}}{\partial t^2} - \mu\sigma \frac{\partial \mathbf{H}}{\partial t} \tag{2.19}$$

Using vector identity $\nabla \times \nabla \times \mathbf{a} \equiv \nabla\nabla \cdot \mathbf{a} - \nabla^2 \mathbf{a}$ and having the knowledge that $\nabla \cdot \mathbf{E} = 0$ and $\nabla \cdot \mathbf{H} = 0$ for homogenous regions, equations (2.18) and (2.19) become;

$$\nabla^2 \mathbf{E} = \mu\sigma \frac{\partial \mathbf{E}}{\partial t} + \mu\varepsilon \frac{\partial^2 \mathbf{E}}{\partial t^2} \tag{2.20}$$

$$\nabla^2 \mathbf{H} = \mu\sigma \frac{\partial \mathbf{H}}{\partial t} + \mu\varepsilon \frac{\partial^2 \mathbf{H}}{\partial t^2} \tag{2.21}$$

Equations (2.20) and (2.21) give the wave equations of the electric and magnetic fields in time domain, respectively. When Fourier transformation of these equations is taken with respect to time, wave equations in the frequency domain are obtained as (Ward and Hohmann, 1987);

$$\nabla^2 \mathbf{E} = -\left(\mu\varepsilon\omega^2 - i\mu\sigma\omega\right)\mathbf{E} \tag{2.22}$$

$$\nabla^2\mathbf{H} = -\left(\mu\varepsilon\omega^2 - i\mu\sigma\omega\right)\mathbf{H} \tag{2.23}$$

or

$$\nabla^2\mathbf{E} = -k^2\mathbf{E} \tag{2.24}$$

$$\nabla^2\mathbf{H} = -k^2\mathbf{H} \tag{2.25}$$

in which,

$$k^2 = \mu\varepsilon\omega^2 - i\mu\sigma\omega \tag{2.26}$$

In equations from (2.20) to (2.23), the effect of displacement current can be neglected and equations from (2.20) to (2.23) may be written as

$$\nabla^2\mathbf{E} = \mu\sigma\frac{\partial\mathbf{E}}{\partial t} \tag{2.27}$$

$$\nabla^2\mathbf{H} = \mu\sigma\frac{\partial\mathbf{H}}{\partial t} \tag{2.28}$$

$$\nabla^2\mathbf{E} = i\mu\sigma\omega\mathbf{E} \tag{2.29}$$

and

$$\nabla^2\mathbf{H} = i\mu\sigma\omega\mathbf{H} \tag{2.30}$$

The wave number k is given related to these equations as $k = \left(-i\mu\sigma\omega\right)^{1/2}$ (Keller and Frischknecht, 1977). Equations 2.27 through 2.30 represent diffusion equations. All these equations give the fundamentals of the MT theory.

2.2.2. Assumptions in the MT method

In the magnetotelluric theory, it is presumed that an electromagnetic wave behaves almost like a plane wave and the Earth is horizontally layered (Vozoff, 1972). Under these assumptions, the solutions of the electromagnetic wave equations are given as (Ward and Hohmann, 1987);

$$\mathbf{E} = \mathbf{E}_0^+ e^{-i(kz-\omega t)} + \mathbf{E}_0^- e^{i(kz+\omega t)} \tag{2.31}$$

and

$$\mathbf{H} = \mathbf{H}_0^+ e^{-i(kz-\omega t)} + \mathbf{H}_0^- e^{i(kz+\omega t)} \tag{2.32}$$

The first terms within the right hand sides of both these equations represent the part of the field which decreases with increasing depth (z). On the contrary, the second terms represent the part of the field which increases with increasing z. In these equations, wave number k that is a complex number is given as

$$k = \gamma - i\Gamma \tag{2.33}$$

in which γ and Γ are both real numbers given by the equations below as (Stratton, 1941; Ward and Hohmann, 1987);

$$\gamma = \omega \left\{ \frac{\mu\varepsilon}{2} \left[\left(1 + \frac{\sigma^2}{\varepsilon^2 \omega^2} \right)^{1/2} + 1 \right] \right\}^{1/2}, \tag{2.34}$$

and

$$\Gamma = \omega\left\{\frac{\mu\varepsilon}{2}\left[\left(1+\frac{\sigma^2}{\varepsilon^2\omega^2}\right)^{1/2}-1\right]\right\}^{1/2}. \tag{2.35}$$

Once conduction currents dominate over displacement currents, γ and Γ become identical real quantities defined by (Ward and Hohmann, 1987)

$$\gamma = \Gamma = \left(\frac{\omega\mu\sigma}{2}\right)^{1/2} \tag{2.36}$$

and, the wave number k is written as

$$k = \gamma(1-i) \tag{2.37}$$

Due to the property of the electromagnetic energy that dissipates as heat with increasing depths, the second terms in equations 2.31 and 2.32 are unrealistic and the solutions of equations may be rewritten using properties of γ and Γ (Ward and Hohmann, 1987);

$$\mathbf{E} = \mathbf{E}_0^+ e^{-i\gamma z} e^{-\gamma z} e^{i\omega t}, \tag{2.38}$$

and

$$\mathbf{H} = \mathbf{H}_0^+ e^{-i\gamma z} e^{-\gamma z} e^{i\omega t}. \tag{2.39}$$

From the equations it is seen that; first of all, decrease of $e^{-\gamma z}$ as z gets larger represents attenuation in the EM waves. Secondly, the first exponential term, $e^{-i\gamma z} = \cos(\gamma z) - i\sin(\gamma z)$, and the third exponential term, $e^{i\omega t} = \cos(\omega t) + i\sin(\omega t)$, mean that the wave varies sinusoidally as a function of depth, z and time, t, respectively (Ward and Hohmann, 1987).

2.2.3. The MT Impedance Tensor

In the MT method, simultaneous variations of the natural electromagnetic field in the three perpendicular magnetic (H_x, H_y, and H_z) and two horizontal electric components (E_x, and E_y) are measured on the surface (Tikhonov, 1950). It is seen from the equations that the electric and magnetic fields decrease when the depth (z) gets increase. At the surface of the Earth ($z = 0$), perpendicular components of two fields (equations 2.38. and 2.39) can be expressed like;

$$E_x(0) = E_0 e^{i\omega t} \tag{2.40}$$

and

$$H_y(0) = H_0 e^{i\omega t} \tag{2.41}$$

or

$$H_y(0) = (i\omega\mu)^{-1}\partial E_x / \partial z \tag{2.42}$$

In these equations, indices x and y represent two horizontal components of the electric and magnetic fields being perpendicular to each other, and E_0 includes information concerning the primary and secondary parts of the electric field. Unfortunately, the primary

field changing with time is unknown in this method, so, the ratio of the components E_x to H_y not depending on the intensity of the primary field is taken in order to remove the effect of the primary field (Cagniard 1953; Kaufman and Keller 1981).

$$\frac{E_x}{H_y} = \frac{\omega\mu}{k} \tag{2.43}$$

The general form of this equation is given as $Z_{ij} = \mathrm{E}_i / \mathrm{H}_j$ and Z is called plane wave impedance, the ratio of the one horizontal component of the electric field to the perpendicular component of the magnetic field. Indices *i* and *j* are the symbols of the perpendicular components, *x* and *y*. Rearranging equation (2.43), the relation of the impedance with conductivity of the subsurface structure can be obtained like;

$$Z_{xy} = \frac{E_x}{H_y} = \frac{\omega\mu}{(i\omega\mu\sigma)^{\frac{1}{2}}} \tag{2.44}$$

Substituting the values of $\omega = 2\pi/T$, $\mu = 4\pi.10^{-7}$ H/m and $\sigma = 1/\rho$ into the equation (2.44), the amplitude of the Z is obtained as;

$$\left|Z_{xy}\right| = \left|Z_{yx}\right| = 2\pi\left(\frac{\rho}{5T}\right)^{1/2}.10^{-3}\,\Omega \tag{2.45}$$

The relation of the electric and the magnetic fields given by a linear formulation and represented with the impedance tensor are shown in equations (2.46) and (2.47), respectively (Cantwell, 1960; Vozoff, 1991).

$$E_x = Z_{xy} H_y + Z_{xx} H_x \tag{2.46a}$$

$$\mathrm{E_y} = \mathrm{Z_{yx}\,H_x} + \mathrm{Z_{yy}\,H_y} \tag{2.46b}$$

$$\begin{pmatrix} \mathrm{E_x} \\ \mathrm{E_y} \end{pmatrix} = \begin{pmatrix} \mathrm{Z_{xx}} & \mathrm{Z_{xy}} \\ \mathrm{Z_{yx}} & \mathrm{Z_{yy}} \end{pmatrix} \begin{pmatrix} \mathrm{H_x} \\ \mathrm{H_y} \end{pmatrix} \tag{2.47}$$

The equation (2.47) is the general appearance of impedance tensor. This tensor representation, in which each term is frequency dependent, changes related to the medium being one or two dimensional that will be mentioned in Chapter 2.3. In the impedance tensor, the diagonal elements are called auxiliary impedances where off-diagonal elements are the principal impedances.

2.2.4. Apparent Resistivity and Phase

The MT results are commonly presented in terms of apparent resistivity, ϱ_a (Ωm), and phase, φ (degree), curves against logarithmic frequency (or period values). Variation of the apparent resistivity values versus frequency is obtained from impedance values. From equation of the impedance tensor for the surface of a horizontally-layered medium (2.44), the impedance tensor for a half-space can be written as;

$$\left|Z(\omega)\right| = \left(\omega\mu\rho\right)^{\frac{1}{2}} \tag{2.48}$$

Rearranging the terms in Equation (2.48) the general form of resistivity formula is obtained;

$$\rho(\omega) = \frac{1}{\omega\mu}\left|Z(\omega)\right|^2 \tag{2.49}$$

Once the medium is not homogeneous, the resistivity values are called apparent resistivity and can be represented as (Cagniard, 1953);

$$\rho_a(\omega) = \frac{1}{\omega\mu}\left|\frac{E_x}{H_y}\right|^2 \qquad \text{or} \quad \rho_a(\omega) = \frac{1}{\omega\mu}\left|\frac{E_y}{H_x}\right|^2 \tag{2.50}$$

The simple form of apparent resistivity is obtained by substituting the values of angular frequency, $\omega = 2\pi / T$, and magnetic permeability, $\mu = 4\pi 10^{-7}\,\mathrm{H}/m$, into the equation (2.50);

$$\rho_a \approx \frac{T}{5}\left|\frac{E_x}{H_y}\right|^2 \text{ (Vozoff, 1972)} \tag{2.51}$$

where T is the period of the electromagnetic field oscillation, and ρ_a is the apparent resistivity in km. Here, it is seen that the apparent resistivity value both depends on the ratio of the electromagnetic field components and the frequency of the signal. Thus, for each frequency of the signal, apparent resistivity values of the medium can be computed.

The other significant parameter in the MT method, phase, can be expressed as (Kaufman and Keller, 1881);

$$\varphi = \arg(Z) = \arg\left(\frac{Z_{imag}}{Z_{real}}\right) \tag{2.52}$$

Phase defined as the argument of the impedance, gives the phase difference between the electric and the magnetic field components. In homogeneous half space, apparent resistivity giving the absolute specific value of the medium is equal to the true resistivity and the phase has a constant value 45˚ (Vozoff, 1991).

2.2.5. Skin Depth

In the equations (2.38) and (2.39), the term $e^{-\gamma z}$ represents the decrease in the strength of the EM field by the motion of the field trough positive direction of z (down into the Earth). In the case of the amplitude of the electromagnetic field is attenuated to e^{-1} of the surface value, depth (z) becomes equal to the value of γ, 1/δ. This relation can be shown as;

$$e^{-\gamma z} = e^{-1} \tag{2.53}$$

By using the definition of γ given in equation (2.36), the definition of δ, inverse of γ, is obtained as (Vozoff, 1991);

$$\delta = \sqrt{\frac{2\rho}{\omega\mu}} \tag{2.54}$$

where ω is angular frequency and μ is magnetic permeability of the medium for a homogeneous half-space model. It is derived from these solutions that in passing through the Earth, EM wave inside an isotropic Earth is attenuated depending on the period, T (sec) (or its inverse frequency, f (Hz)), of the waves and resistivity, ρ (Ωm) of the Earth. The depth at which EM waves attenuate is defined by a term skin-depth, δ (m), and the formula:

$$\delta \cong 503\sqrt{\frac{\rho}{f}} = 503\sqrt{\rho T} \quad \text{(Ward and Hohmann, 1987)} \qquad (2.55)$$

The equation (2.56) indicates that for mapping deeper structures, measurements at higher periods are needed (Figure 2.4).

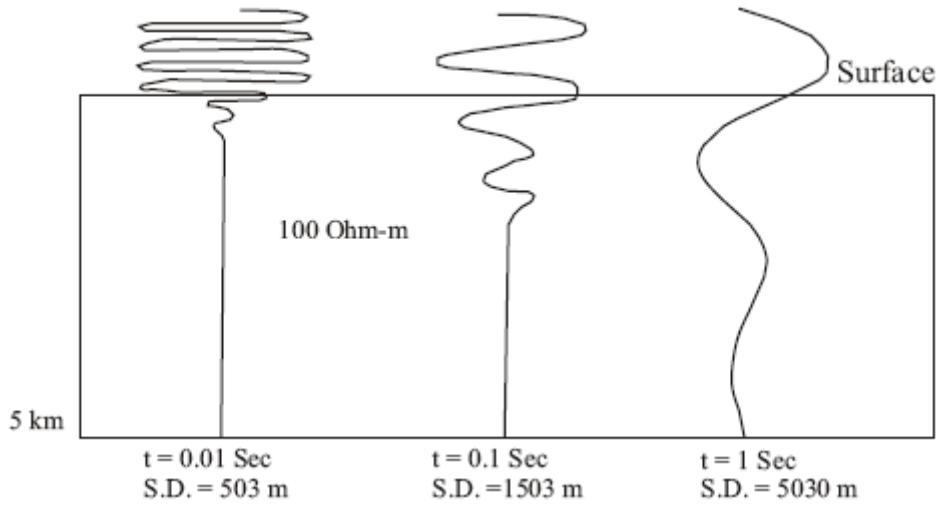

Figure 2.4. Attitude of EM wave via variant periods in the same medium (100 Ωm).

In addition to the first outcome of equation (2.55), other result of it is that for a primary field of a given period, the induced EM fields penetrate to a larger depth in a more

resistive medium. The penetration of the EM wave related both to the frequency and resistivity values is demonstrated in Figure 2.5.

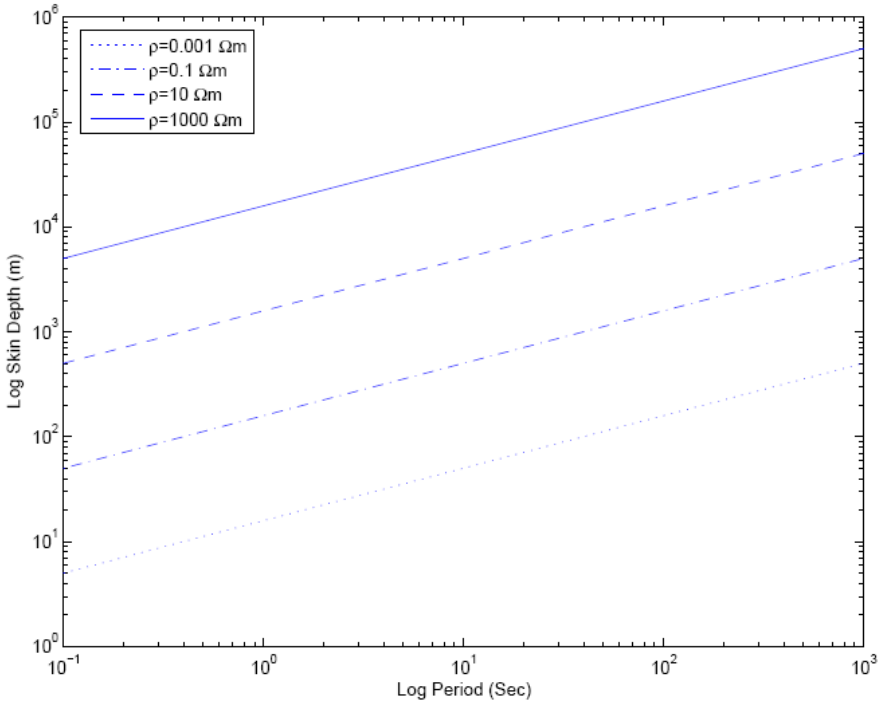

Figure 2.5. Skin depth variation as a function of period and resistivity.

In the equations 2.38 and 2.39, the term $e^{-iz\alpha}$ can also be presented using skin depth as $e^{-iz/\delta}$. This term represents the change of phase with depth, z. When $z_2 = 2\pi\delta$, phase of the field components changes by 2π. Then, the distance z_2 is called wavelength, λ, of the EM wave and shown as (Kaufman and Keller, 1981);

$$\lambda = 2\pi\delta \tag{2.56}$$

2.2.6. The Induction Vectors

Besides from the apparent resistivity and phase curves, there is another graphical representation of the conductivity distribution related to the subsurface structure. This representation is also obtained from observed data like the two others and is called induction arrows. Induction arrows obtained from transfer functions (tipper) give the information concerning conductivity of subsurface. Therefore, before determining induction arrows, definitions of transfer functions, must be given.

The relation between the horizontal and vertical components of the magnetic induction is demonstrated as (Parkinson, 1959);

$$B_z = T_x B_x + T_y B_y \tag{2.57}$$

Here, B_x, B_y, and B_z are the horizontal and vertical components of the magnetic induction, respectively, where T_x and T_y are the complex magnetic transfer functions, induction vectors. These vectors are horizontal vectors with a magnitude

$$T_x = T_{zx} = \frac{H_z}{H_x} \tag{2.58}$$

$$T_y = T_{zy} = \frac{H_z}{H_y} \tag{2.59}$$

The combination of these transfer functions' real and imaginery parts gives the real and imaginery induction arrows. The length of the arrows is given as;

$$\left(\mathrm{Re}\,T_{\mathrm{x}}^{2}+\mathrm{Re}\,T_{\mathrm{y}}^{2}\right)^{\frac{1}{2}} \tag{2.60}$$

$$\left(\mathrm{Im}\,T_{\mathrm{x}}^{2}+\mathrm{Re}\,T_{\mathrm{y}}^{2}\right)^{\frac{1}{2}} \tag{2.61}$$

for the real and imaginary arrows, respectively. The azimuths of the real and imaginary arrows are represented , respectively, as;

$$\tan^{-1}\left(\frac{\mathrm{Re}\,T_{\mathrm{y}}}{\mathrm{Re}\,T_{\mathrm{x}}}\right) \tag{2.62}$$

$$\tan^{-1}\left(\frac{\mathrm{Im}\,T_{\mathrm{y}}}{\mathrm{Im}\,T_{\mathrm{x}}}\right) \tag{2.63}$$

The arrows indicate lateral variations in conductivity. They may point toward the regions of higher conductivity, Parkinson convention (Parkinson, 1959), or higher resistivity, Wiese convention (Wiese, 1962) related to the choice of convention (Jones, 1986). In the two-dimensional (2D) case, real and imaginary induction arrows are seen as parallel or anti-parallel to each other.

2.3. Dimensionality and Decomposition of the MT Data

The dimensionality in the MT method represents the variation of the conductivity of the subsurface structure. The conductivity variation may be only the function of depth or both depth and the horizontal components. If the conductivity variation within the Earth is only the function of depth, $(\sigma(z))$, the medium is one dimensional (1D). If this variation depends on both the depth and one of the horizontal components, (either $\sigma(x,z)$ or $\sigma(y,z)$), the medium is called two dimensional (2D). And lastly, if the variation is the

function of both two horizontal components together with depth, in this case, the medium is said three dimensional (3D) (Vozoff, 1991).

The general representation of the MT impedance tensor is given by a 2x2 tensor;

$$Z = \begin{bmatrix} Z_{xx} & Z_{xy} \\ Z_{yx} & Z_{yy} \end{bmatrix} \tag{2.64}$$

In the case of one-dimensionality, the diagonal components of the impedance tensor are zero, $Z_{xx} = Z_{yy} = 0$, and off diagonal elements have the equation that $Z_{xy} = -Z_{yx}$ where the tensor relations of the electric and magnetic fields are represented as $E_x = Z_{xy} H_y$ and $E_y = Z_{yx} H_x$. On the other hand, in two-dimensional case, there are two circumstances. If one of the components (either *x* or *y*) is parallel to the geo-electric strike, that means $Z_{xx} = Z_{yy} = 0$ but $Z_{xy} \neq -Z_{yx}$. If both two components are not parallel to the geo-electric strike, then off diagonal components become $Z_{xx} = -Z_{yy} \neq 0$. If the medium is 3D, in this case, all the components have a value different than zero and each other, $Z_{xx} \neq Z_{xy} \neq Z_{yx} \neq Z_{yy} \neq 0$ (Vozoff, 1991).

Related to the dimensionality of the medium, resistivity and phase equations display variation in representation. When apparent resistivity and phase equations for the general case (3D) are known, in any case, either the medium is 1D or 2D, the apparent resistivity and phase equations can be find out from their general forms. The general formula of the apparent resistivity and phase are given as;

$$\rho = \frac{1}{\omega\mu}\left|Z_{xx}Z_{yy} - Z_{xy}Z_{yx}\right| \tag{2.65}$$

and its phase

$$\phi = \text{ phase of } \left(Z_{xx}Z_{yy} - Z_{xy}Z_{yx}\right) \tag{2.66}$$

Once one of the components is along the geo-electric strike (the 2D case), the calculation turns into a simpler form. Under this circumstance, two-dimensional MT method has two modes. These modes represent measured fields and they are called transverse electric (TE, **E** polarization) and transverse magnetic (TM, **B** polarization) modes (Figure 2.6).

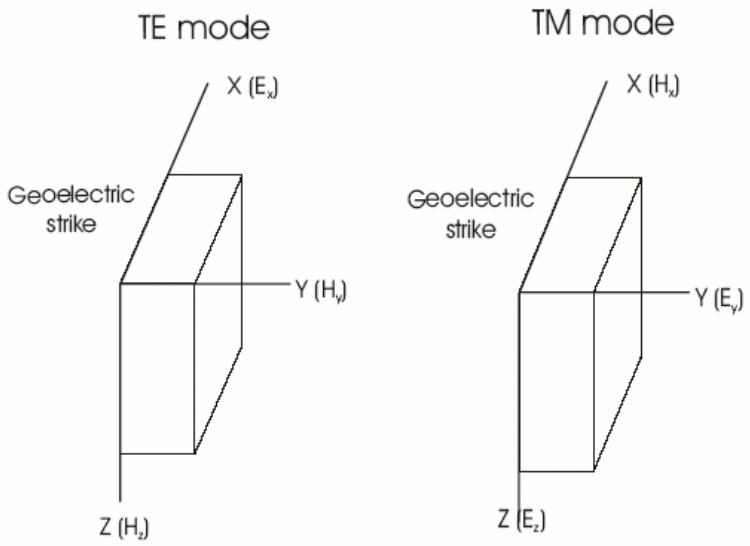

Figure 2.6. Geo-electric strike together with TE and TM modes for 2D medium.

TE mode represents that the electric field is flowing along the geo-electric strike. On the contrary, TM mode demonstrates that the magnetic field is along the geo-electric strike. For the case represented in Figure 2.6, E_x, H_y, and H_z field components comprise the TE mode and apparent resistivity for this mode is calculated from the ratio of E_x to H_y where

E_y, H_x, and E_z field components comprise the TM mode with the calculation of apparent resistivity from E_y to H_x ratio.

In order to be able to mention about TE and TM modes, there must be certainty that the data is 2D. It is obvious that dimensionality analysis of the MT data has a significant role in the MT data processing. Various techniques have been developed by scientists while the MT data processing methods has been improving. There are two essential techniques which are developed by Swift (1967) and Bahr (1991). Both techniques (Swift, 1967; Bahr, 1991) depend on the relation between the elements of the impedance tensor. Apart from determination of dimensionality, there is another important problem in the MT data processing called galvanic effect. This effect which will be given in detail in Chapter 2.3.2 stems from the near surface heterogeneities and cause telluric and magnetic distortions on the MT data (Ogawa, 2002). Galvanic effect must be eliminated to reach true resistivity models of the subsurface.

2.3.1. Swift's Skew and Bahr Parameters

Two significant techniques of dimensionality analysis are obtained as the consequence of so simple relation between the components of the impedance tensor. According to Swift (1967), the diagonal and off-diagonal elements of the impedance tensor are related to each other with a ratio called skew (κ);

$$\kappa = \frac{Z_{xx} + Z_{yy}}{Z_{xy} - Z_{yx}} \tag{2.67}$$

In the equation, κ is the skewness parameter (skew) and it is rotationally invariant tensor. Once the skew nearly equals to zero, $\kappa \leq 0.1$, this represents that the medium is

1D. Whenever it extends this value, the medium departs from 1D case. In 3D case, the skew has a value higher then 0.3, $0.3 < \kappa$ (Ledo, 1998).

Similar to Swift's skew, Bahr's (1991) parameters giving the dimensionality of the medium are related to the components of the impedance tensor. The first of the three parameters of Bahr is μ, one-dimensionality parameter is given by;

$$\mu = \frac{\left(\left[\left[D_1, S_2\right]\right] + \left[\left[S_1, D_2\right]\right]\right)^{1/2}}{\left|D_2\right|} \tag{2.68}$$

where

$$S_1 = Z_{xx} + Z_{yy}, \quad S_2 = Z_{xy} + Z_{yx}, \quad D_1 = Z_{xx} - Z_{yy}, \quad D_2 = Z_{xy} - Z_{yx} \tag{2.69}$$

and,

$$\left[\left[D_1, S_2\right]\right] = \mathrm{Im}\left(S_2 D_1^*\right) = \mathrm{Re}\, D_1\, \mathrm{Im}\, S_2 - \mathrm{Re}\, S_2\, \mathrm{Im}\, D_1 \tag{2.70}$$

$$\left[\left[S_1, D_2\right]\right] = \mathrm{Im}\left(D_2 S_1^*\right) = \mathrm{Re}\, S_1\, \mathrm{Im}\, D_2 - \mathrm{Re}\, D_2\, \mathrm{Im}\, S_1 \tag{2.71}$$

and * indicates complex conjugate. In the case of $\mu \approx 0$, the medium is treated as 1D representing less complex model. Once the value of μ differs from zero, this circumstance indicate that the medium is either two or tree dimensional. The second parameter of Bahr is regional skew, η (Bahr, 1988);

$$\eta = \frac{\left(\left[D_1, S_2\right] - \left[S_1, D_2\right]\right)^{1/2}}{\left|D_2\right|} \tag{2.72}$$

Regional skew gives two-dimensionality and three-dimensionality of the medium. If $\eta = 0$, the medium is 2D, however it goes away from 2D in the case of $\eta > 0$. Once $\eta > 0.3$, the medium becomes 3D. The last parameter of Bahr is two-dimensionality parameter and symbolized by Σ.

$$\Sigma = \frac{\left(D_1^2 + S_2^2\right)}{D_2^2} \tag{2.73}$$

This parameter represents that the medium is 2D once its value is greater than 0.1, $\Sigma > 0.1$.

2.3.2. Galvanic Distortion

Generally, the data obtained during the MT surveys include not only the properties of the real subsurface structure but also the effects of the near-surface inhomogeneities (heterogeneities). By the effect of these heterogeneities the MT responses may be distorted; hence, distortion analysis of the MT data is one of the significant steps in data processing recognized since the 1970's (Berdichevky and Dimitriev, 1976; Larsen, 1977; Groom and Bailey, 1989; Ogawa, 2002). This distortion on the MT data may be telluric or magnetic. Once the magnetic distortion ignored on land observations, only the effect of galvanic distortions exist on the MT data (Ogawa, 2002).

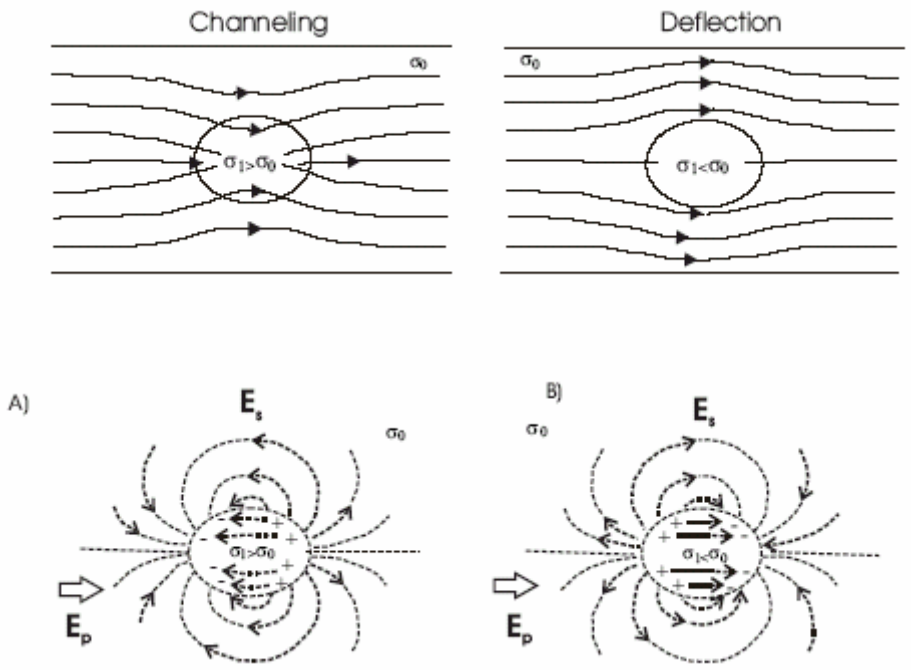

Figure 2.7. Demonstration of galvanic distortion of the electric field. The charge distribution is demonstrated for substances of a conductive (a) and resistive (b) materials (the cases of channeling (top left) and deflection (top right). E_p is the primary electric field directed from left to the right, and E_s is the secondary electric field associated with E_p (redrawn from Jiracek, 1990).

The basic mechanism responsible for the distortion of the electric field is caused by the charge accumulation at the boundaries of the near surface conductivity heterogeneity by the flux of regional current through the heterogeneity (Figure 2.7) (Jiracek, 1990). Distortions of the regional current flow by the effect of the secondary or the scattered electric field produced by the charge accumulation is called galvanic distortions (Caldwell, 2004) and can be classified into two categories as phase mixing and static shift (Ogawa, 2002).

In order to remove the effects of the near-surface heterogeneities, various methods can be exercised (Ogawa, 2002). Some methods are; spatial filtering (Torres-Verdin and Bostick, 1992); using independent information free from the effect of galvanic distortion

like key layer (Jones, 1988), and time-domain sounding together with the MT data (Pellerin and Hohmann, 1990); and lastly eliminating the effect of the static shift in inversion modeling (deGroot-Hedlin, 1991; Ogawa and Uchida, 1996) which is used in this study. On the other hand, to remove the effect of phase mixing (distortion of galvanic orthogonality), Groom-Bailey (1989) decomposition technique which gives the distortion on the direction of the MT data from the geo-electric strike is widely used.

2.3.3. Groom-Bailey Decomposition (1989) and McNeice and Jones Approach (2001)

Once the regional structure is 2D, one of the coordinate axes on survey area must be in parallel to the geo-electric strike. However, in the MT surveys the strike of the MT profile and geo-electric strike of the region generally do not coincide. The reasons are that inadequate information concerning geo-electric strike during field surveys or the effects of galvanic distortions on the MT data. Therefore, defining the geo-electric strike and rotating the coordinate axes on survey area to this direction is essential in the MT data processing.

The rotation of axes had been firstly determined by Swift (1967). Assuming the regional structure is 2D, he defines the rotation of measurement axes (x, y) by an angle ϕ (Figure 2.8) in Cartesian coordinate system as multiplication of the electric and magnetic fields with a rotation matrix (R).

$$\mathbf{E}' = \mathbf{RE} \text{ and } \mathbf{H}' = \mathbf{RH} \tag{2.74}$$

where

$$\mathbf{R} = \begin{bmatrix} \cos\phi & -\sin\phi \\ \sin\phi & \cos\phi \end{bmatrix} \tag{2.75}$$

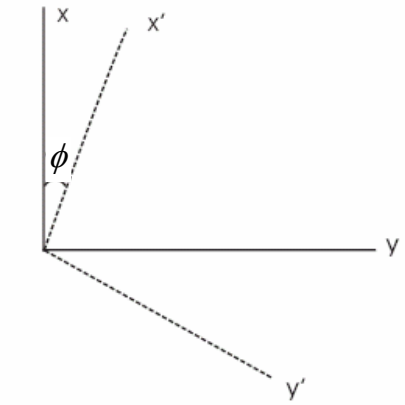

Figure 2.8. Axis rotation from measurement (*x, y*) into the regional axes (*x', y'*) by an angle ϕ (Swift, 1967).

Rotated electric and magnetic fields are obtained from the equation 2.74 and they constitute rotated impedance tensor;

$$E' = Z' H' \tag{2.76}$$

and

$$Z' = RZR^T \tag{2.77}$$

where R^T is transpose of R, which is. $R^T = \begin{bmatrix} cos\phi & sin\phi \\ -sin\phi & cos\phi \end{bmatrix}$

In order to define the geo-electric strike for 2D case, $Z_{xx} = Z_{yy} = 0$ and $Z_{xy} \neq Z_{yx}$, Swift suppose that summation of the auxiliary impedances must be minimized as a function of rotation angle ϕ_0.

$$\left|Z_{xx}(\phi)\right|^2 + \left|Z_{yy}(\phi)\right|^2 \Rightarrow \min \tag{2.78}$$

And also by maximizing $\left|Z_{xy}(\phi)\right|^2 + \left|Z_{yx}(\phi)\right|^2$, Swift gives the strike angle as;

$$4\phi_0 = \tan^{-1} \frac{\left(Z_{xx} - Z_{yy}\right)\left(Z_{xy} + Z_{yx}\right)^* + \left(Z_{xx} - Z_{yy}\right)^*\left(Z_{xy} + Z_{yx}\right)}{\left|Z_{xx} - Z_{yy}\right|^2 - \left|Z_{xy} + Z_{yx}\right|^2} \tag{2.79}$$

where * indicator of conjugate. ϕ_0 , strike angle in the case that distortion is present, will not be the same as true strike angle ϕ . Therefore, the methods which determine true strike after removing the effect of surface heterogenities by decomposing impedance tensor have been developed. One siginificant decomposition method was presented by Groom and Bailey (1989).

Decomposition method of Groom and Bailey (1989) depends on the assumptions that the regional structure is 2D and only distorted by the effect of inductively small local 3D structures. In this case, Groom and Bailey (1989) solve the strike problem using a decomposition technique that separates the parameters of regional and local structures and gives the computation of strike angle.

The basic decomposition model of Groom and Bailey (1989), which is firstly determined by Larsen (1977) (McNiece and Jones, 2001), is given by;

$$\mathrm{Z_m} = \mathrm{RCZ_{2D}R^T} \tag{2.80}$$

In the equation, Z_m and Z_{2D} indicate measured and regional 2D impedance tensor in the strike coordinates, respectively. R^T is transpose of R. C is a 2x2 distortion tensor which is given by;

$$C = gTSA \tag{2.81}$$

where *g* is a scalar quantity termed site gain, T and S are matrices termed twist and shear, respectively, and A is anisotropy tensor. The twist (T) and shear (S) tensors are the determinable parts of the distortion tensor while site gain (g) and anisotropy (A) tensors account for the indeterminable parts which together with termed static shift and scale the apparent resistivity curves. The twist tensor affects the electric field by rotating it through a clockwise angle $\phi_s = \tan^{-1} t$ where *t* is the twist. On the other hand, shear tensor rotate the *x* axis through clockwise by an angle $\phi_e = \tan^{-1} e$ where *e* is the shear (Groom-Bailey, 1989).

Absorbing *g* and *A* into the 2D impedance tensor Z_{2D}, measured impedance tensor Z_m can be rewritten as;

$$Z_m = RTSZ_{reg}R^T \tag{2.82}$$

where Z_{reg} is the scaled regional 2D impedance tensor (gAZ_{2D}). The regional 2D geo-electric strike and information about the regional impedance can be recovered by minimizing least-squared misfit between the decomposition parameters α_0, α_1, α_2, and α_3 obtained from measured impedance tensor (Equations 2.83a-2.83d) and from the model (Equations 2.84a-2.84d.).

$$\alpha_0 = Z_{xx} + Z_{yy} \tag{2.83a}$$

$$\alpha_1 = Z_{xy} + Z_{yx} \tag{2.83b}$$

$$\alpha_2 = Z_{yx} - Z_{xy} \tag{2.83c}$$

$$\alpha_3 = Z_{xx} - Z_{yy} \tag{2.83d}$$

$$\alpha_0 = t\sigma + e\delta \tag{2.84a}$$

$$\alpha_1 = (\delta - et\sigma)\cos 2\phi - (t\delta + e\sigma)\sin 2\phi \tag{2.84b}$$

$$\alpha_2 = -\sigma + et\delta \tag{2.84c}$$

$$\alpha_3 = -(t\delta + e\sigma)\cos 2\phi - (\delta - et\sigma)\sin 2\phi \tag{2.84d}$$

After determination of the parameters of regional and local structures by Groom-Bailey decomposition technique, tensor decomposition analysis has become one of the significant parts of the MT data processing and interpretation (McNeice and Jones, 2001). Between these decomposition methods, presenting tensor decomposition of the MT data for multisite and multifrequency data set, McNeice and Jones (2001) approach used in this study has a special place.

The targets of McNeice and Jones (2001) analysis are; elimination of the effects of galvanic distortion and determination of geo-electric strike not only for one station and one frequency but also for entire data set (McNeice and Jones, 2001). Approach of McNeice and Jones originates from Groom-Bailey decomposition since this method gives the all of the parameters of the decomposition model. While they extend the decomposition of Groom-Bailey for all data set, McNeice and Jones (2001) support that regional strike is usually only well-defined over a small subset of data, and the dependence of model misfit on strike statistically consistent with the entire data set or data subset.

2.4. Theory of the MT Modeling

The subsequent step in the process of the MT data is to convert the apparent resistivity and phase curves into the model of electrical resistivity as a function of depth and horizontal position. This conversion consists of two types operations termed as forward and inverse modeling.

Once ***m*** and **F(m)** denote the model parameters and model response, respectively, the predicted data **D** calculated from the model is given by the equation;

$$\mathbf{D} = \mathbf{F}(\mathbf{m}) \tag{2.85}$$

This relation represents the general form of forward modeling. If there are M data of N measurement for an experiment, the model parameters and observed (measured) data are given as vectors of length M and N, respectively.

$$\mathbf{m}=[m_1, m_2, \dots, d_M]^T \tag{2.86}$$

$$\mathbf{d}=[d_1, d_2, \dots, d_N]^T \tag{2.87}$$

where T refers to transpose. When **d** displays measured data, inverse modeling gives the comparison of the measured and computed data sets as;

$$\mathbf{F}(\mathbf{d}, \mathbf{m}) = \mathbf{d} - \mathbf{F}(\mathbf{m}) \tag{2.88}$$

The matrix representation of this relationship is given as

$$\mathbf{F}(\mathbf{d},\mathbf{m}) = \begin{bmatrix} d_1 \\ d_2 \\ . \\ . \\ d_N \end{bmatrix} - [\mathbf{F}] \begin{bmatrix} m_1 \\ m_2 \\ . \\ . \\ m_M \end{bmatrix} \tag{2.89}$$

In the MT forward modeling; the main target is to compute the resistivity and phase values for resistivity structure given as the Earth model. On the other hand, in the inverse modeling, the observed resistivity and phase values obtained on the surface of the Earth are compared with the calculated parameters obtained from the initial Earth model and the misfit between them is tried to be minimized.

2D inversion code of Ogawa and Uchida (1996) used in this study determines data misfit, **S**, as;

$$\mathbf{S}(\mathbf{m}) = \left|\mathbf{Wd} - \mathbf{WF}(\mathbf{m})\right|^2 \text{ (Ogawa and Uchida, 1996)} \tag{2.90}$$

where

$$\mathbf{m} = \begin{bmatrix} m_p \\ g \end{bmatrix} \tag{2.91}$$

In the equation, $\mathbf{m}_p$ represents the logarithms of block resistivities since the model parametrization is composed of rectangular blocks. The weights symbolized by **W** in the equations are relevant to standard deviations of the data while static shifts, g, is defined one by one for each field site and mode (TE and TM). The data **d** may contain the

logarithm of apparent resistivity and the phase of impedance and even the magnetic transfer function once the accurate data is obtained during field measurements.

Since the problem is non-linear at the beginning of the inversion process, it is linearized by computing the Jacobian and then the data misfit, **S**, is minimized after some iteration of the inversion process. If $\mathbf{m}_{\text{old}}$ describes the model parameters of the previous iterative step within the case **m** is so close to $\mathbf{m}_{\text{old}}$, **S** can be approximated by using the Jacobian matrix **A** as follows;

$$\mathbf{S}(\mathbf{m}) \approx \mathbf{S_0}(\mathbf{m}) = \left| \mathbf{W}\hat{\mathbf{d}} - \mathbf{WAm} \right|^2, \tag{2.92}$$

where

$$\hat{\mathbf{d}} = \mathbf{d} - \mathrm{F}(\mathbf{m}_{old}) + \mathrm{A}\mathbf{m}_{old}, \tag{2.93}$$

$$\mathbf{A} = \left[\frac{\partial F}{\partial m} \right]_{m=m_{old}} \tag{2.94}$$

It is mentioned that constitution of model parametrization comes a number of rectangular blocks. Linear combinations of neighbouring block resistivities (logarithms) form the element of the roughening vector **h** which is formed as

$$\mathbf{h} = \left| \mathbf{C}\mathbf{m}_p \right|^2, \tag{2.95}$$

where **C** is roughening matrix. The difference of the log resistivity of a block from the average log resistivity of its surrounding blocks constitutes the same element of the vector $\mathbf{Cm_p}$. In Ogawa and Uchida's (1996) inversion process the static shift is used as an inversion parameter. Therefore, L_2 norm is defined for the static shift as;

$$G = \sum_{site} \sum_{TE,TM} |g|^2 \tag{2.96}$$

And then, S_o is minimized under the constraints that **h** and **G** are both minimized. This is achieved by minimizing misfit functional **U** as follows for given values of sm^2 and ss^2, Lagrange multipliers;

$$\mathbf{U} = \mathbf{S}_0 + sm^2\mathbf{h} + ss^2\mathbf{G}\,. \tag{2.97}$$

Once it is believed that model parameter are close enough to the real values, inversion is ended off. So that the model parameters are being obtained as a consequence of the inversion as close as possible to their true value.

3. STUDY AREA, DÜZCE

3.1. Geologic and Tectonic Settings of the Study Area

Turkey is one of the seismically active countries in the World. Evolution of the tectonic structure of Turkey is controlled by the movement of Anatolian block and surrounding tectonic plates which are the Eurasian, African, and Arabian plates (Figure 3.1) (Bozkurt, 2001). The Eurasian plate extends from the northwestern Turkey to the Caucasus at northeast while African and Arabian plates located south and southeast Turkey, respectively, move to the north. Relation between northward-moving African and Arabian plates and relatively stable Eurasian plate is the source of two intercontinental strike-slip faults, North Anatolian Fault (NAF) and East Anatolian Fault (EAF) (Bozkurt, 2001).

In the past decade, two primary fault zones, the NAF and the EAF, (Figure 3.1.) give rise to the occurrence of the most destructive earthquakes in Turkey. The NAF that is 1200-km-long east-west oriented fault zone starts from Karlıova in the east (in the late Miocene) and continues until Gulf of Saroz in the northern Aegean Sea. (Bozkurt, 2001; Şengör *et al.*, 2005). This fault zone has right-lateral strike-slip faulting mechanism (Hitchcock et al., 2003) as a consequence of motion of the Anatolian plate to the west relative to the Eurasian plate, which is 18-25 mm/yr (Reilinger *et al.*, 2000). The NAF zone has experienced one or more large earthquakes per decade during its motion from the east to the west (Parsons et al., 2000). West of Bolu, this fault zone splays into two branches to the north and south. Northern branch forms Düzce Fault and southern branch extends through the Lake Abant and Mudurnu Valley (Ayhan et al., 2001; Akyüz et al., 2002; Çakır et al., 2003).

Figure 3.1. Map showing the plate motions which is effective on the tectonics of Turkey (Okay et al., 1999).

Düzce fault, 70-km-long extends from Kaynaşlı in the east to the near Eften Lake in the west (Akyüz *et al.*, 2002). Through the most part of its extension, the Düzce fault has the characteristic properties of the NAF zone, which is east-west oriented right-lateral strike-slip faulting. However, the strike of Düzce fault changes from E-W to NE-SW with the angle of greater than 30° at west of Gölyaka (Çakır et al., 2003). This westernmost segment of the Düzce fault named Karadere segment has ruptured in August, 1999 having approximately 30-km-long. The rupture zone broken as a result of the Düzce earthquake is about 40-km-long (Arpat *et al.*, 1999; Ayhan *et al.* 2001; Akyüz *et al.*, 2002). Düzce earthquake's surface rupture, Düzce basin, southern stand of NAF, and the highland region between the Düzce fault and southern stand of NAF constitute the region on which the MT data acquired and conductivity structure investigated (Figure 3.2).

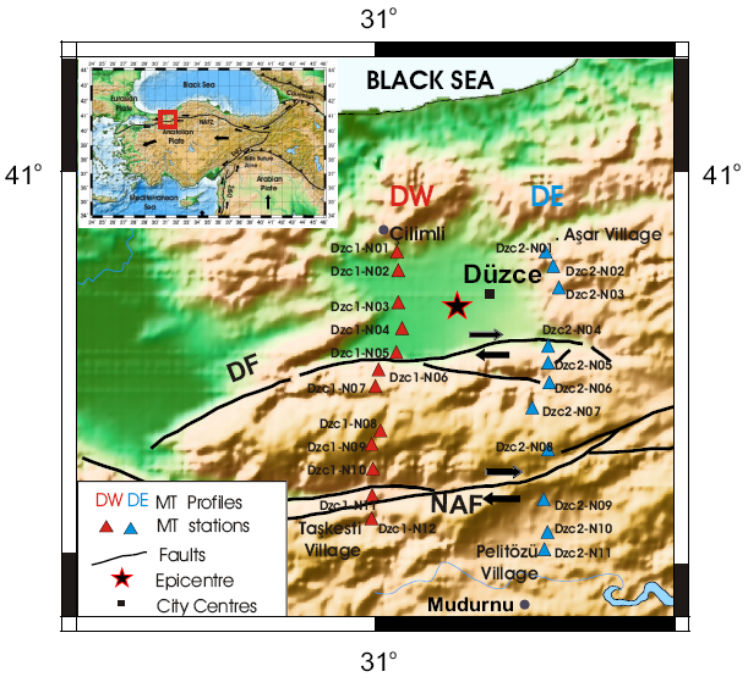

Figure 3.2. The tectonic map of the study area (drawn by GMT). Black line and black arrows represent the fault lines and relative motions of the faults, respectively. Star indicates epicenter of the Düzce earthquake. Red and blue triangles show the Düzce West (DW) and Düzce East (DE) profiles, respectively.

The Düzce basin which has well-proportioned boundaries to the north and to the south with Çilimli and Düzce faults, respectively, has irregular margins to the east and to the west. The Düzce basin, Almacık and south Bolu mountains, taking place between Düzce and Mudurnu valley represent three different tectonic zones in western Turkey all of which are parts of the Pontides (Figure 3.3).

The Pontides extends along northern Turkey. From the north to the south, the İstanbul-Zonguldak zone, the Armutlu-Ovacık zone, and the Sakarya continent are some fragments of the western Pontides, which extend from the Bulgarian Rhodope to the Kargı massif (Yılmaz *et al.*, 1997; Yiğitbaş *et al.*, 1999), and these three zones constrain the target area of this study.

The Düzce basin is located in the İstanbul-Zonguldak zone and it has nearly 260-m-thick younger sedimentary section sitting mainly on Eocene volcanogenic flysch (Şengör et al., 2005) (Figure 3.3). In figure 3.3, the dominant formations that encircles the Düzce basin are denoted with geologic ages. It is seen from the Figure 3.3 that the geologic units observed in the Armutlu-Ovacık zone belong both to the İstanbul-Zonguldak zone and the Sakarya continent.

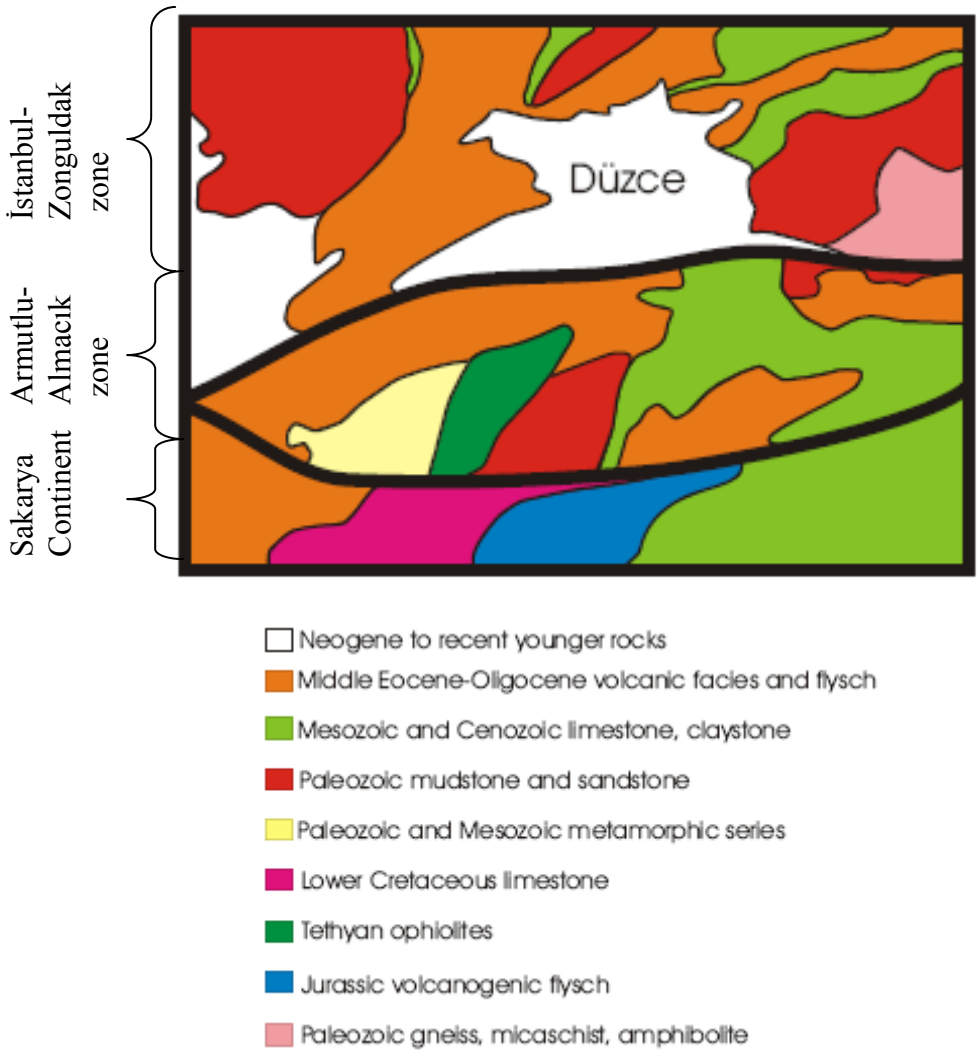

Figure 3.3. Geological map of Düzce and its vicinity (modified from the MTA, 1999 and Yılmaz *et al.*, 1997) with major tectonic divisions of the western Pontides.

3.2. Previous Studies

Occurrence of destructive Erzincan earthquake (Mw: 8.0) 68 years ago, became the starting point of large earthquake sequence on the North Anatolian Fault (NAF) zone from the east to the west (Parsons *et al*, 2000). The Düzce earthquake (Mw: 7.2, 1999) following the disastrous İzmit earthquake (Mw: 7.4, 1999) is the latest large earthquake of this sequence. In order to introduce Düzce earthquake and Düzce fault, the outcomes of some studies relevant to the Düzce earthquake will be presented in this part.

The Düzce fault has already taken attention of geoscientists after the İzmit earthquake as the single unbroken segment on the NAF zone during the east-to-west migration of large earthquakes (Barka, 1999). After the Düzce earthquake, significant parameters relevant to the earthquake and Düzce fault such as magnitude of the earthquake, dip and slip of the fault, and rupture velocity, were well investigated by using geodetic (Ayhan *et al.*, 2001; Bürgmann *et al.*, 2002; Çakır *et al.*, 2003), and seismologic data (Bouchon *et al.*, 2001, Bouin *et al.*, 2004, Birgören *et al.*, 2004).

The bilateral Düzce earthquake beginning on hypocenter and processing on both eastward and westward caused the total ~40-km-long surface rupture (Ayhan *et al.* 2001; Akyüz *et al.*, 2002; Bürgmann *et al.*, 2002). The results of the geodetic and seismologic studies indicate that Düzce earthquake had right lateral strike-slip faulting with normal component. Although dominant strike-slip faulting along the fault rupture was confirmed by all these studies, normal component was controversial matter (Ayhan *et al.* 2001; Akyüz *et al.*, 2002; Bürgmann *et al.*, 2002; Çakır *et al.,* 2003; Bouin *et al.*, 2004). When all these geodetic and seismological studies are considered, it is seen that strike of east-west oriented Düzce fault and dip of the rupture to the north can be given within a range between N75˚E-N105˚E (Ayhan *et al.* 2001; Akyüz *et al.*, 2002; Bürgmann *et al.*, 2002; Çakır *et al.,* 2003; Bouin *et al.*, 2004) and 51˚N-73˚N (Ayhan *et al.* 2001; Bürgmann *et al.*, 2002; Çakır *et al.,* 2003; Bouin *et al.*, 2004), respectively. Existence of the Düzce earthquake's hypocenter at northern of the Düzce fault (40.82˚ N, 31.186˚ E, B.U., Kandilli

Observatory and Earthquake Research Institute) and aftershock distribution (Figure 3.4) are demonstrated by these studies as the clues of the north dipping normal component Düzce fault. Another indicator of the normal component is vertical slip observed during Düzce fault with strike-slip component. All studies suggest that the maximum strike-slip was observed near the central part of the rupture zone close to the hypocenter. The observed maximum right lateral offset was ~500 cm (Ayhan *et al.*, 2001; Akyüz *et al.*, 2002) which gradually descends towards the both edges and towards the deeper parts (Ayhan *et al.*, 2001; Akyüz *et al.*, 2002). On the other hand, the maximum vertical displacement, ~350cm, was observed at the westernmost of the Düzce fault along the southern margin of the Efteni Lake (Akyüz *et al.*, 2002). The Düzce earthquake had the singularity of having the highest slip-to-rupture-length ratio of historic earthquakes existed on NAF (Ayhan *et al.*, 2001).

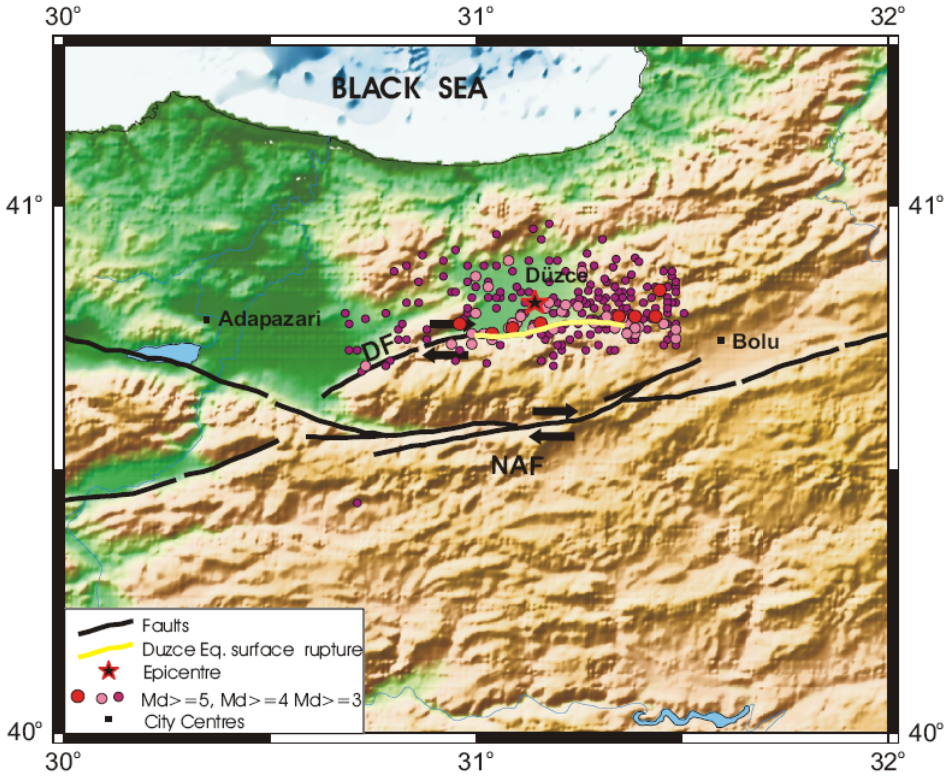

Figure 3.4. Tectonic map of the Düzce region. Black lines show active faults at the region and yellow line represent surface rupture of the Düzce earthquake (Ayhan *et al.*, 2001). The black arrows indicate the direction of the motion. Star demonstrates epicenter of the earthquake. Red, pink, and purple circles are the aftershocks having magnitude Md ≥ 5,

Md ≥ 4, and Md ≥ 3, respectively, (observed for 3 month after main-shock, B.U., Kandilli Observatory and Earthquake Research Institute).

All geodetic and seismologic studies except the study of Çakır *et al.*, (2003) are focusing on that a simple fault ruptured during the Düzce earthquake. However, Çakır *et al.*, (2003) from the modeling of multiple fault rupture, reveal a possibility that the fault broken with the Düzce earthquake under the effect of a near vertical Düzce fault and an old trust fault which dips to the north. In Figure 3.4, study area, the main shock, and aftershock distribution of the Düzce earthquake are shown.

In addition to the studies relevant to the Düzce earthquake and Düzce fault some of which mentioned above, Bouchon *et al.* (2001) focused on the rupture velocity of the Düzce earthquake. With the aim of revealing propagation speed of the rupture during the Düzce earthquake, they used ground motion records obtained at two stations which are located near the edges of the Düzce rupture. They calculated 3.35 sec. and 3.95 sec. time delay, S-P time, at west (Gölyaka) and east (Bolu) stations, respectively. Although the time delay calculated at western station is expected S-P time, the delay time at the eastern station was less than expected, 5.25 sec. (Bouchon *et al.*, 2001). This short time delay obtained toward the east was also confirmed by the study of Bouin *et al.*, (2004). The average rupture velocity between the hypocenter and eastern and western stations were almost 4 km/s (Bouchon *et al.*, 2001, 4.3 km/s; Bouin *et al.*, 2004, 4.1 km/s) and 3km/s (Bouchon *et al.*, 2001), respectively. Under the light of these evidences, it is claimed by Bouchon *et al.* (2001) and Bouin *et al.*, (2004) that the eastern rupture propagated at supershear speed while western rupture propagated at sub-Rayleigh speed.

Another study related to rupture velocity of the Düzce earthquake (Mw: 7.1) was performed using ground motion data by Birgören *et al.* (2004) (Figure 3.5). The results of waveform inversion show that two asperity zones exist on the region. One of these high slip areas, large asperity, appears near the hypocenter area where another, smaller asperity, exists closer to surface in the eastern part of the fault plane. Birgören *et al.* (2004) also

estimated two strong motion generation areas (SMGA) having large slip velocity. These areas have the same location with the asperities with a difference in a negligible amount (Figure 3.6). The results of the study indicate that apparent velocity of rupture propagation between two asperities was 3.2 km/s, and the rupture between the two SMGAs propagated with a velocity nearly S-wave speed. Inside the large SMGA, rupture propagates to the east with a velocity (Vr) 3.5 km/s and to the west 2.9 km/s where inside the small SMGA Vr is estimated as 3.5 km/s. On the other hand, first time window front propagation velocity (FTWFPV) (the propagation velocity of the virtual fastest rupture front) for eastern and western sites was found as 4.8 and 2.9 km/s, respectively. All these results indicate that eastern part of the Düzce rupture propagated partially at supershear velocity (Birgören *et al.*, 2004).

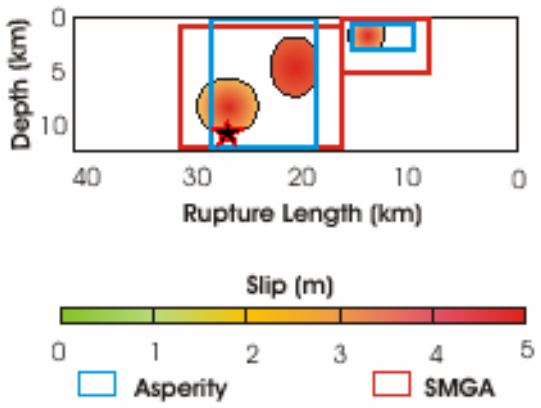

Figure 3.5. Final slip distribution on the fault plane. Slip distribution is seen in full circles. Red and blue rectangles show the SMGAs and asperities, respectively. (Birgören *et al.*, 2004).

4. INSTRUMENTATION AND FIELD PROCEDURE

Magnetotelluric (MT) method does not require artificial sources and it can be used as an effective method to demonstrate the electrical resistivity distribution of the subsurface including the fault zones. There are several examples in the literature that MT method was used as an efficient tool for this aim (Ogawa *et al.*, 2000; Unsworth *et al.*, 2000; Bedrosian *et al.*, 2002; Tank *et al.*, 2005; Ritter *et al.*, 2005). On the evidence of these studies MT method has been applied to the Düzce Fault. In this chapter, the information including the properties of the field instruments used during MT surveys and scheme of the field measurements will be given.

In MT surveys, two (horizontal) components of the electric and three components of the magnetic field are measured simultaneously by MT recorder. At the beginning of the instrument setting, a reference direction being generally geomagnetic north is determined by a compass. For telluric part, five non-polarized electrodes are used (Figure 4.1). Two of these electrodes compose a dipole oriented north-south while the two others composing a second dipole which is oriented east-west. These north-south and east-west oriented dipoles, (one is orthogonal to the other), are generally referred as E_x and E_y dipoles, respectively. This designation comes from the circumstance that they measure the X and Y components of the electric field. The interval between the dipoles has a range from 50 m to 100 m depending on the survey area. The last electrode acts as ground and is placed at the site center. Besides the electrodes, two of the three induction coils are termed as horizontal induction coils (H_x and H_y). Likewise the right angle cross design of the electrodes, horizontal induction coils are located on the field being parallel to the north-south and east-west directions (Figure 4.1). The other induction coil is buried completely in a vertical direction into the ground and so that it is termed as vertical induction coil (Vozoff, 1972).

During data acquisition, the electric and magnetic field components must be measured as accurate as possible. The correct measurement of the data depends on some

necessities concerning the study area and the scheme of the MT instruments. For this reason, it is preferred that the survey area is selected far from the noise factors such as power lines, wire nettings, and long trees. Spreading of the electrodes is under the effect of these situations. The electrodes are buried nearly 25 cm deep in a salty mud to improve contact resistance between the electrode and the ground. The layout of the electric cable has also significance in field measurements.

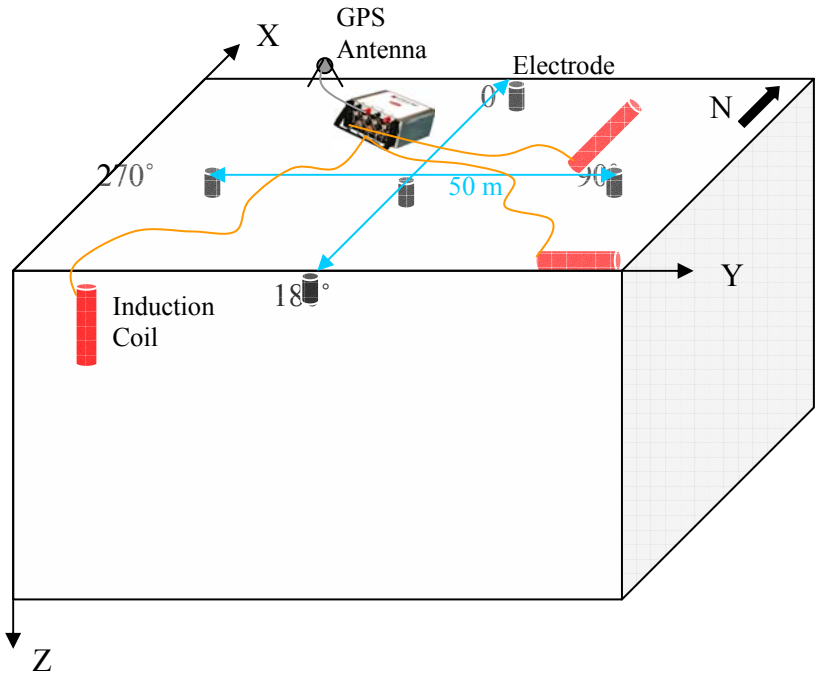

Figure 4.1. Scheme of the MT field measurement. From the figure the general design of the electrodes (black cylinders), induction coils (red cylinders), and other instruments such as data recorder, GPS antenna, and cables used for MT field measurements is seen clearly.

Likewise the layout of the electrodes and cables, the position and orientation of the induction coils claim attention. The north-south (H_x) and east-west (H_y) aligned induction coils are placed in the field with their free end pointing north and east, respectively. Another significant point for induction coils is the interval between them. Once the coils are placed near to each other, they generate additional magnetic fields which disturb the measured data. To avoid these additional magnetic fields, each coil must be separated from

the other by a distance at least 3 m. If the region contains noisy magnetic field, then a region near the survey area which is less noisy with respect to survey site is chosen as a reference site. This technique is called remote reference technique (Gamble et al, 1979). During the survey, the electric and magnetic fields are measured on both the survey and reference sites. In data analysis section, the electric field of the survey site is processed together with the magnetic field of the reference site. It is obvious that in order to avoid problems caused by the data in data processing, the data must be obtained carefully just like in all applied geophysics methods.

5. OBSERVED AND CALCULATED MT DATA

In the previous chapters, the MT method, its process, and field procedure have been given to make clear why MT method is used in this study. This chapter describes the MT data and gives their entire process from the acquisition in raw case on land to the final case which gives the real resistivity model of the target area.

5.1. Data Acquisition

The Düzce survey was conducted as a joint project, funded by TUBITAK, as collaboration between Boğaziçi University, Kandilli Observatory and Earthquake Research Institute and National Academy of Sciences of Ukraine. As a result of data acquisition, processing of observed data, and modeling, electrical resistivity structure of Düzce fault was obtained. The data acquisition stage started in 2005. The aim was to obtain MT data along two parallel north-south oriented profiles one of which is located at west of the epicenter and the other one at east, and both cross Düzce fault and North Anatolian Fault (NAF) from north to the south (Figure 5.1).

The data set in Düzce was obtained in two campaigns. During the first campaign, the MT data were acquired at 12 stations in the west and 5 southern stations of the east profile by three Phoenix Geophysics MTU-5 instruments two of which are supplied by Alberta University, Canada. The first profile was extended from Tepeköy village (Çilimli) at the north to Taşkesti-Ilıca village (Mudurnu) at the south being almost 36 km long with station spacing varying from 1.3 km to 5.7 km (Figure 5.1). At each station, the two electric and three magnetic components were recorded. The electric and magnetic field variations were recorded within the frequency range between 320 Hz to 0.0005 Hz (~1800 s). Simultaneous record of the electric and magnetic field components was achieved using GPS (Global Positioning System) signals. In all stations, the axis orientations of the

recorded components were parallel (E-W) and perpendicular (N-S) to the Düzce fault strike (Figure 4.1) and orientation of the profile was also perpendicular to the geological strike which is strike of the Düzce fault (Figure 5.1). The instruments were left one or if necessary two days in the field for continuous recordings and the data were recorded overnight from 5 p.m. to the 10 a.m. (local time).

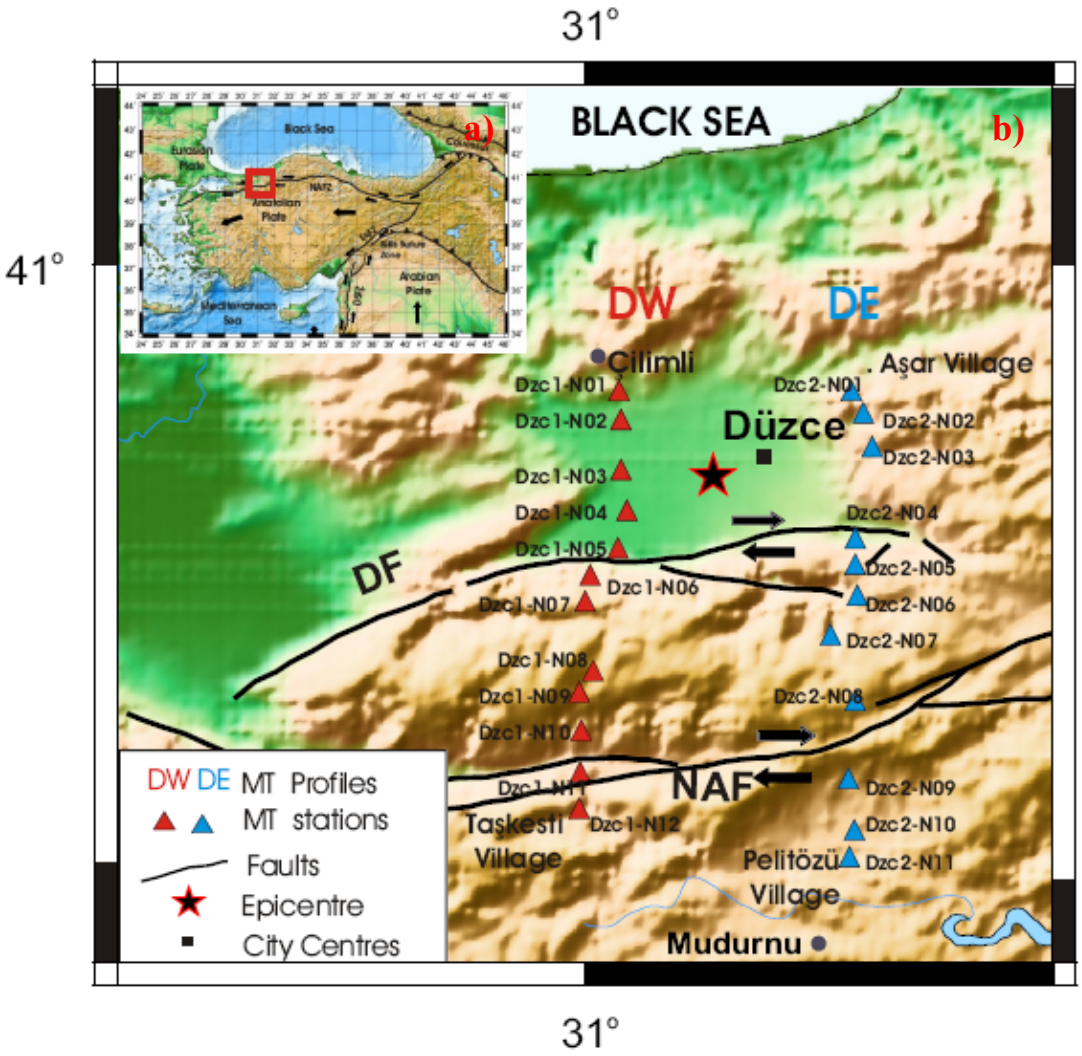

Figure 5.1. a) Tectonic map of Turkey indicating study area with open red square. b) The map of Düzce region shows location of the west (DW) and east (DE) profiles and its tectonics. Red and blue triangles with numbers represent MT stations of the west and east profiles, respectively. Star is the epicenter of 1999 Düzce earthquake (from USGS).

The east profile (DE), was located almost 23 km to the east of DW profile in parallel. The DE profile, almost 41 km long, extended from Aşar village (Yığılca) at the north to the Pelitözü village (Mudurnu) at the south. It is composed of 12 stations with a separation ranging from 2.2 km to 7.3 km. The MT data from southern 5 stations of the DE profile had already been collected in the first campaign. During the second campaign, remaining data were acquired from 7 stations. Finding suitable areas in the forest or areas far from noise sources such as power lines was difficult. Single instrument was used during the second campaign and one of the records being under the effect of high noise was not appropriate to use in processing. Therefore, although the data were collected at 12 stations, just 11 of them could be used for processing. Along the DE profile, the data were recorded within the same frequency range with the DW profile.

5.2. Data Processing

In this part, application of processing steps on real data will be described. In MT data processing, firstly, the data recorded in time domain is transformed into frequency domain by using Fourier transform and apparent resistivity and phase values are calculated. After analysis of apparent resistivity and phase curves, they are plotted versus period. Next, the dimensionality of the data is investigated through tensor decomposition. Following tensor decomposition and strike estimation of the data, modeling and inversions are performed to obtain smoothest and best fitting model to the observed data.

5.2.1. Data in Frequency Domain

5.2.1.1. Apparent Resistivity and Phase Curves. During the MT campaigns, the time variation of the electric and magnetic fields for 23 stations of both profiles were recorded and the data were stored on the removable flash cards. As a first step of the processing, the time domain data were transformed into frequency domain data by using discrete Fourier transform. Following the calculation of the impedance from frequency domain data

(Equation 2.44), apparent resistivity and phase values were obtained (Equation 2.50) and these values were plotted versus period. Once the high scattering and large error bars were observed on the apparent resistivity and phase curves, remote reference technique was applied and the data were reprocessed.

In Figures 5.2 and 5.3, all apparent resistivity and phase curves versus period were plotted for the DW and DE profiles, respectively. The XY curves represent the ratio of the X component of the electric field to the Y component of the magnetic field and YX curves show vice versa. In field, the electric and magnetic field components were set assuming that X represents north-south component and Y represents east-west component.

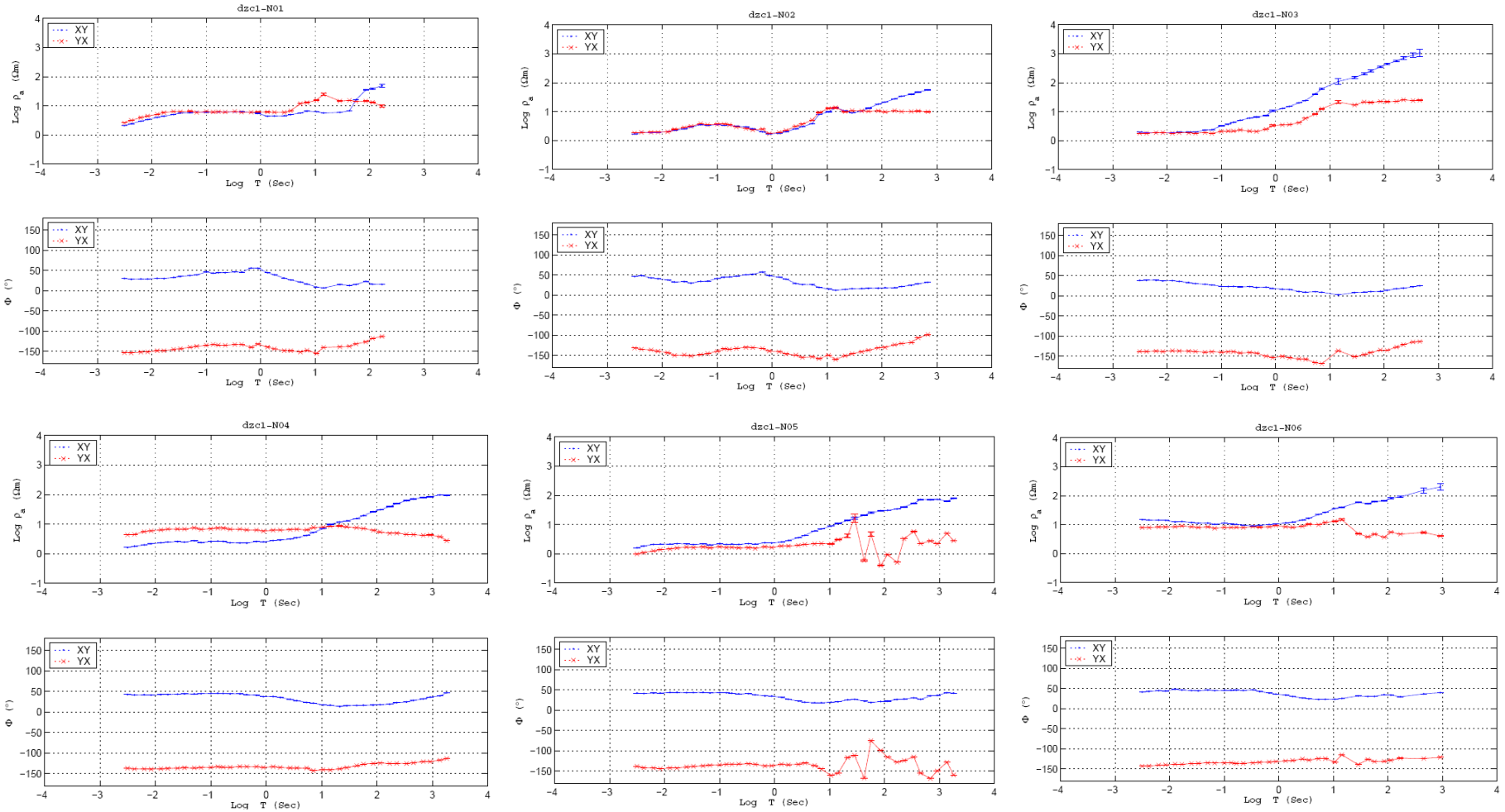

Figure 5.2-a. XY and YX modes apparent resistivity (Log ρ_a) and phase (Φ) responses versus period (Log T) with their error bars estimated for six stations, 1-6, located from the north to the south of the DW profile.

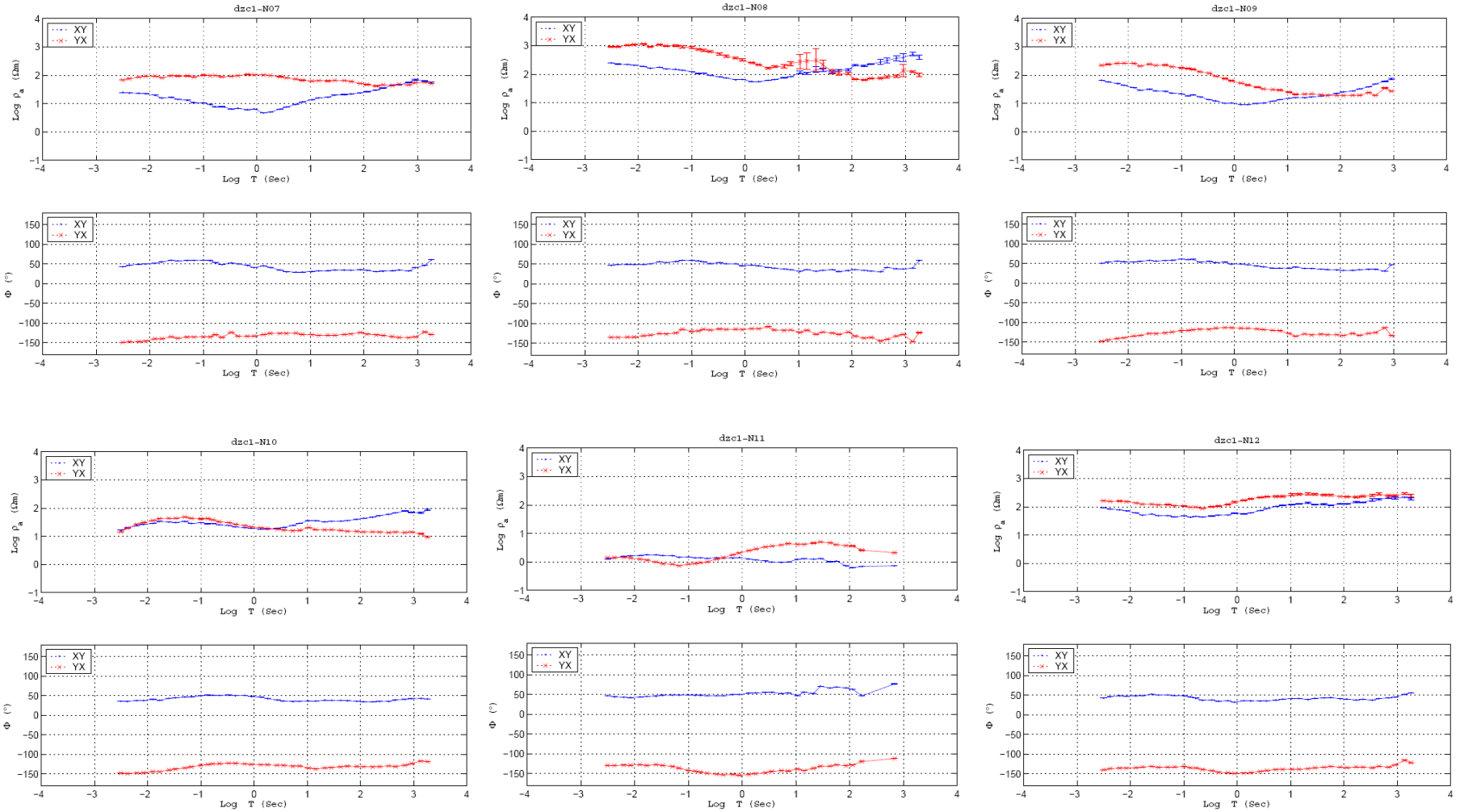

Figure 5.2-b. XY and YX modes apparent resistivity (Log ρ_a) and phase (Φ) responses versus period (Log T) with their error bars estimated for six stations, 7-12, located from the north to the south of the DW profile.

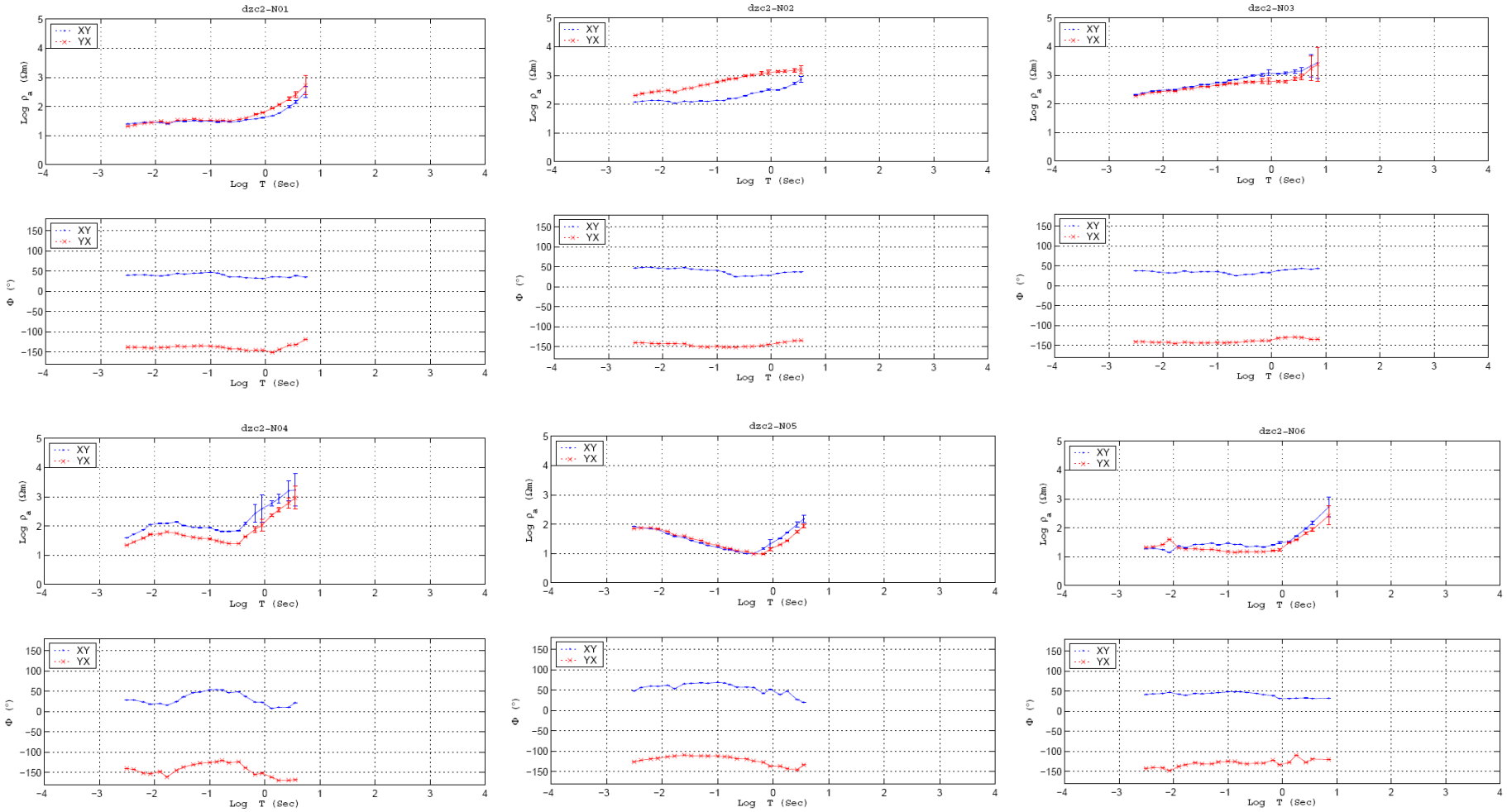

Figure 5.3-a. XY and YX modes apparent resistivity (Log ρ_a) and phase (Φ) responses versus period (Log T) with their error bars estimated for six stations, 1-6, located from the north to the south of the DE profile.

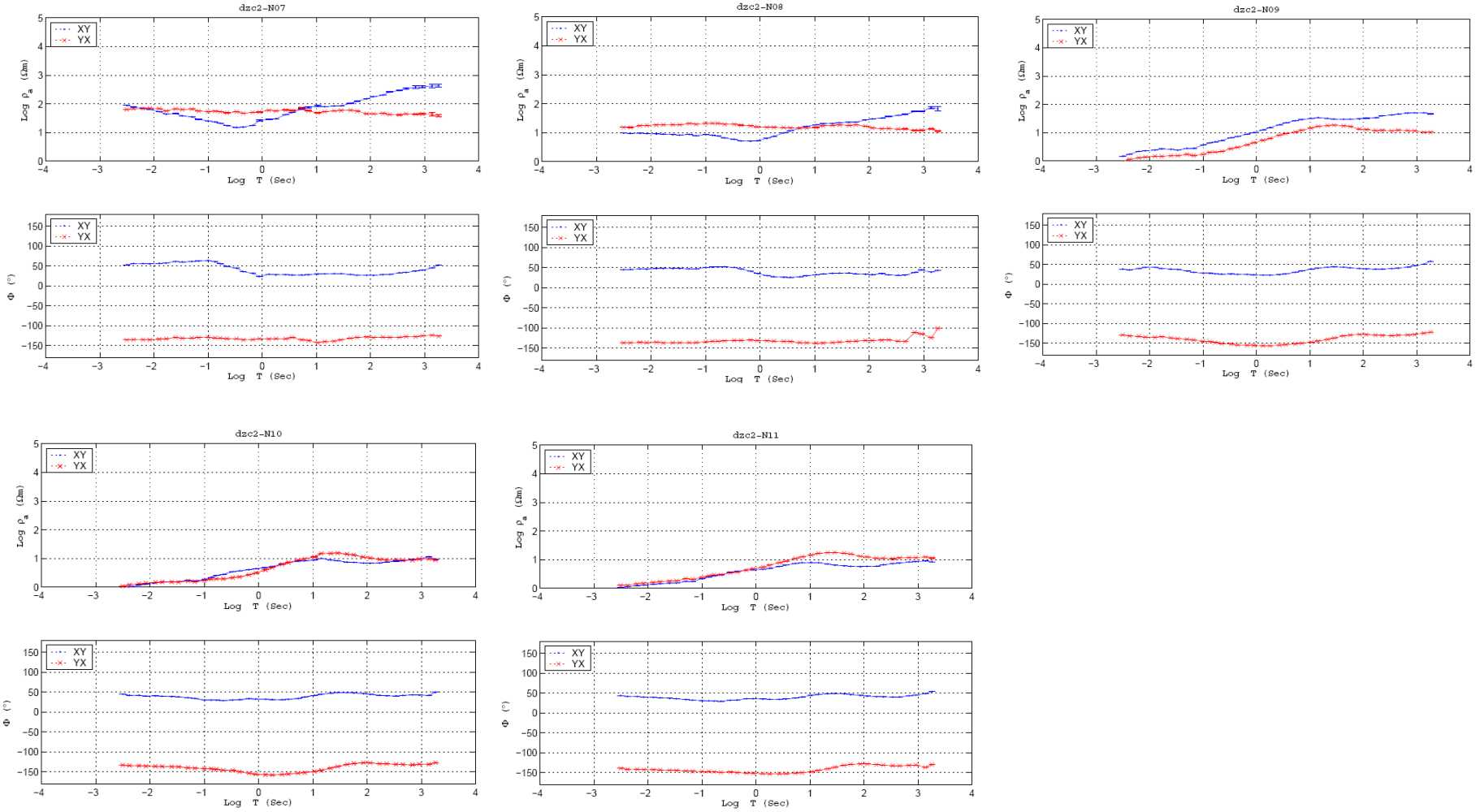

Figure 5.3-b. XY and YX modes apparent resistivity (Log ρ_a) and phase (Φ) responses versus period (Log T) with their error bars estimated for five stations, 7-11, located from the north to the south of the DE profile.

The whole data set was investigated separately and general information about the resistivity feature of the region was obtained (Figures 5.4, 5.5). According to this examination, the apparent resistivity and phase curves could be classified into three groups. In Figures 5.4 and 5.5, apparent resistivity and phase values demonstrated resistivity transition of the basins (Düzce and Mudurnu) and highland (Almacık Mountain) from the north to the south for both the west and east profiles. The consistency of the XY and YX modes for high frequencies takes attention. Because of that XY and YX modes give the resistivity variation of the field for two perpendicular axes; this consistency is an evidence of the one-dimensionality of the medium.

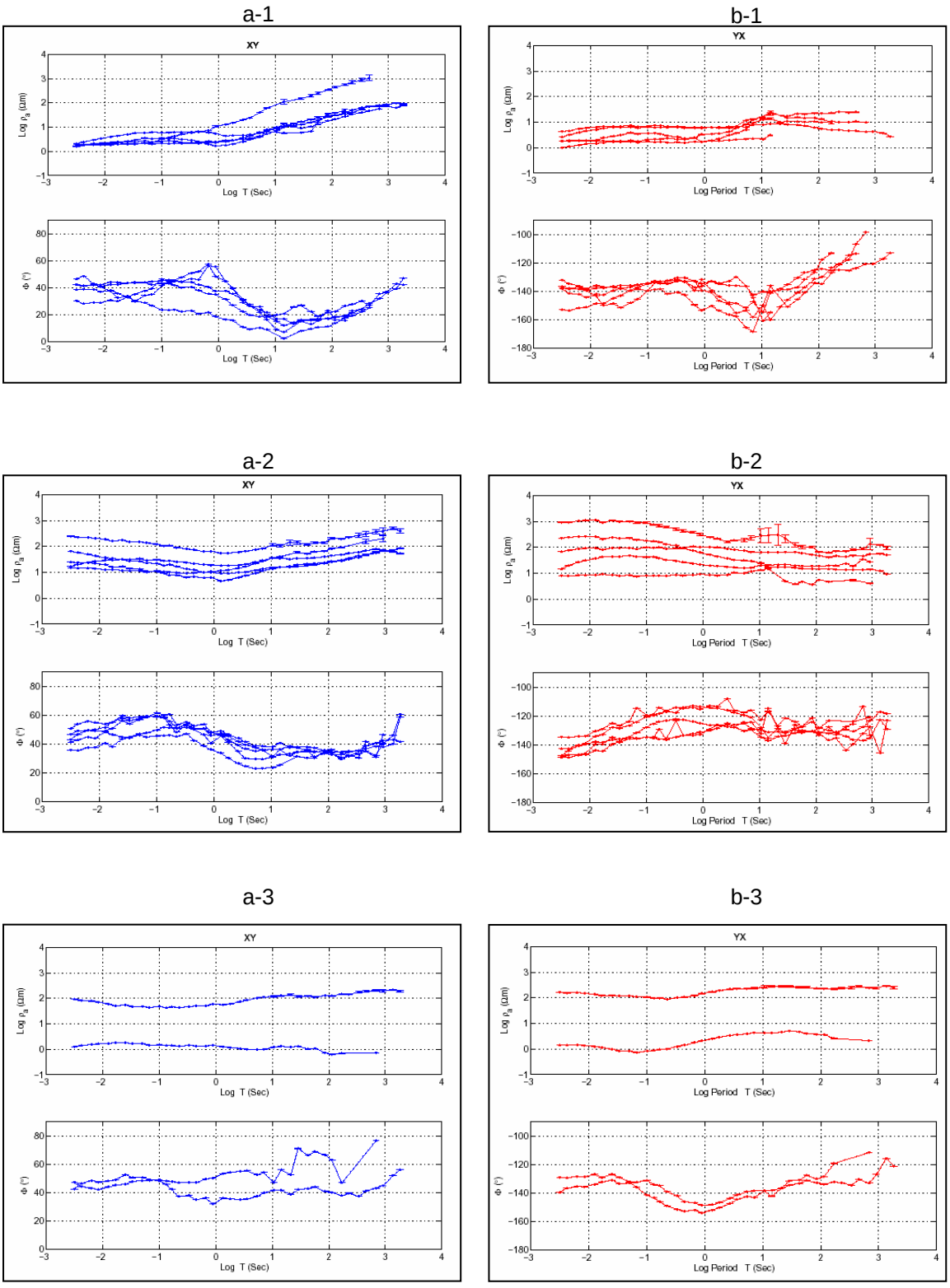

Figure 5.4. Apparent resistivity and phase curves of the a) XY and b) YX modes with their error bars for three groups of the DW profile.

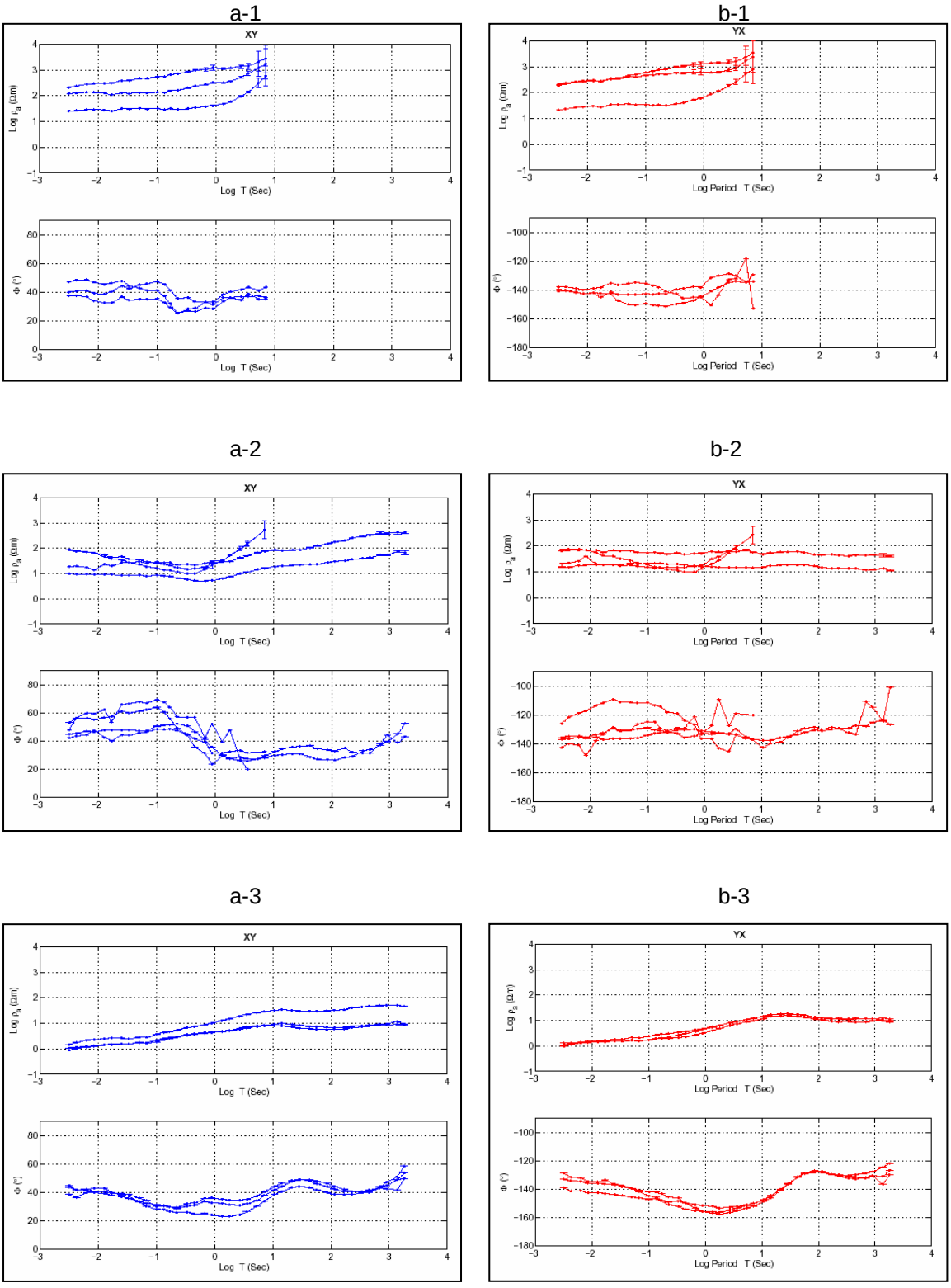

Figure 5.5. Apparent resistivity and phase curves of the a) XY and b) YX modes with their error bars for three groups of the DE profile.

5.2.1.2. Induction Arrows. Another investigation method applied during the analysis of the observed data is to calculate (Chapter 2, Section 2.6) and plot induction arrows. In Figure 5.6, the real induction arrows for three different periods are shown in Parkinson convention. The direction of these arrows demonstrates the conductive structure in the region and their lengths represent magnitudes of the conductor. At T=0.01 sec. (Figure 5.6) induction arrows are under the effect of surface inhomogeneities, therefore they are scattered. But, in periods 1 sec., induction arrows indicate high conductor at the south of the DW profile and at period 100 sec. they denote the NE-SW oriented conductive layer.

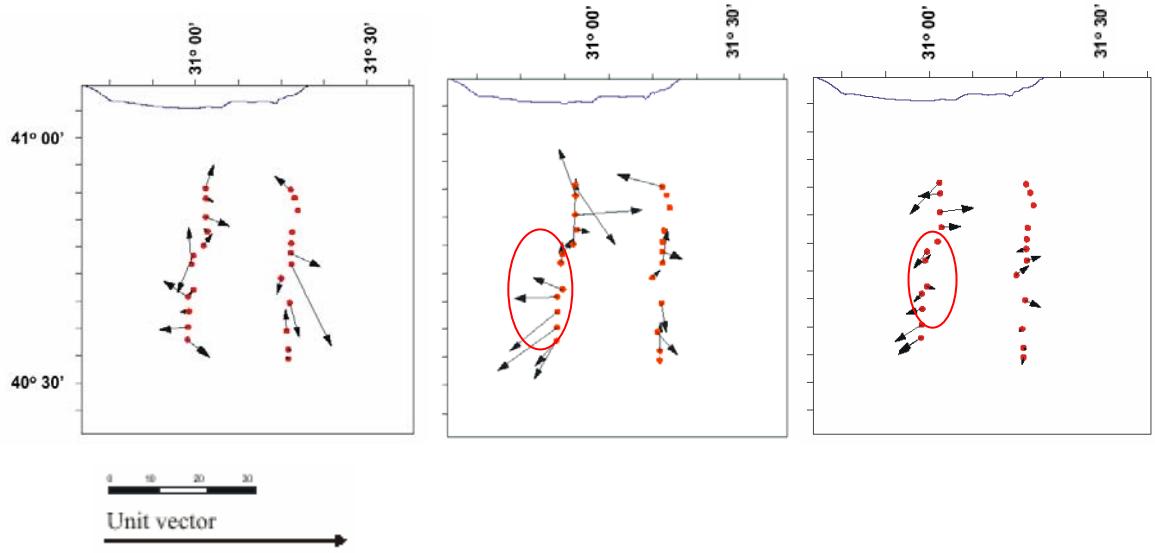

Figure 5.6. Real induction arrows in Parkinson convention at three periods T=0.01 sec., T=1 sec., T=100 sec.

5.2.2. Dimensionality of the Observed Data

After analysis of the apparent resistivity and phase values, as the second step of the MT data processing, dimensionality of the data were investigated. To perform this, the skewness parameter (Swift, 1967), α, was calculated using equation 2.67. In Figure 5.7, variation of the skewness value with period for all stations of the west and east profiles are

shown, respectively. It's seen from the graphs that nearly until 0.1 sec., the data set is almost one-dimensional (1-D) for both DW and DE profiles.

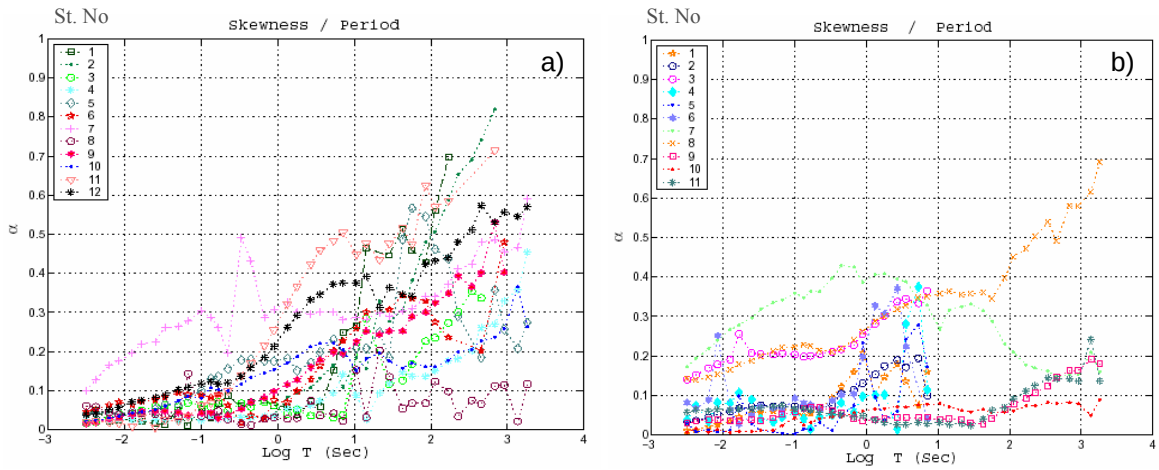

Figure 5.7. Graphs of the skewness parameter, α, versus period for the a) DW and b) DE profiles. Numbers in the legends represent stations in the profiles from the north to the south.

In addition to the skewness parameter, Bahr's dimensionality parameters, μ, Σ, and η were also investigated (Bahr, 1991). Bahr's 1-D parameter, μ, which is a rotationally invariant measure of phase difference in the impedance tensor (Bahr, 1991) was calculated from the equation 2.68 and plotted versus period (Figure 5.8). Once μ=0, it means that the data set is absolutely 1-D. In Figure 5.8, it's clear that for lower periods the data get nearer to one dimensionality where dimensionality increases with period.

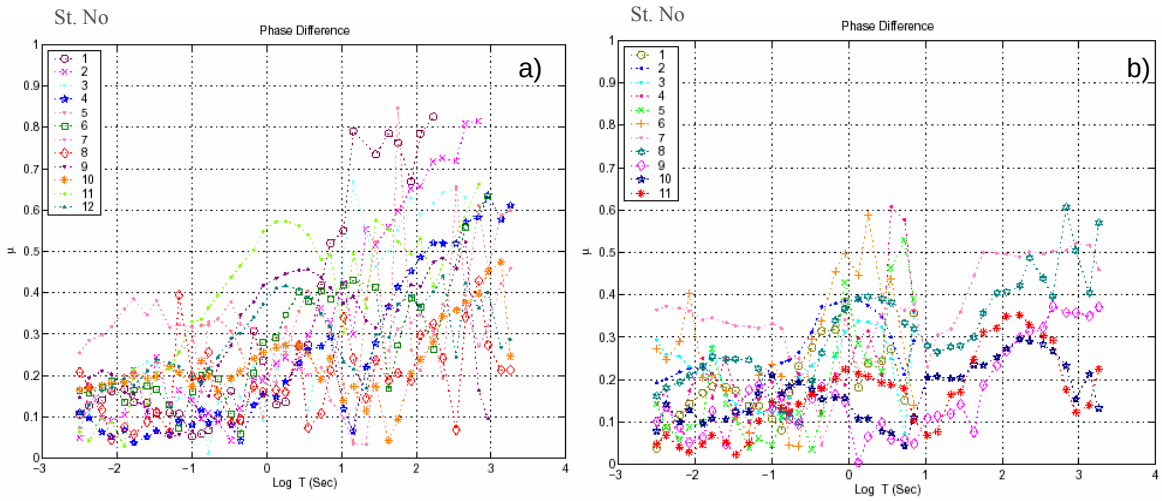

Figure 5.8. Graphs of the 1-D parameter, μ, versus period for the a) DW and b) DE profiles. Numbers in legends represent stations in the profiles from the north to the south.

Bahr's rotationally invariant measure of two-dimensionality, Σ parameter, (Bahr, 1991) was calculated from the equation 2.73 for estimation of dimensionality of the data. In Figure 5.9, Σ is given for all data set. This parameter demonstrates two-dimensionality if its value gets higher than 0.1 (Bahr, 1991). The values of the Σ, plotted on the Figure 5.9-a and 5.9-b for DW and DE profiles, show two-dimensionality of the data after ~0.1 sec.

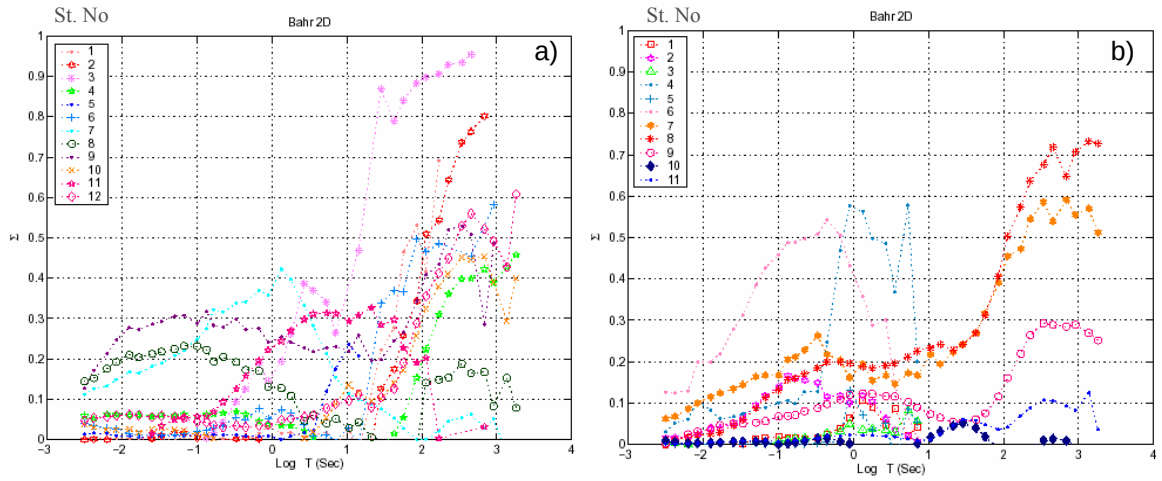

Figure 5.9. Graphs of the Σ parameter versus period for the a) DW and b) DE profiles. Numbers in the legends represent stations in the profiles.

The other dimensionality parameter of Bahr is the regional skew, η. Regional skew gives the information concerning three-dimensionality of the data. Once this parameter has values higher than 0.3, then the data demonstrates three-dimensionality. The three-dimensionality of the Düzce profiles was estimated by calculating η as a function of period (Equation 2.72). The graphs in Figure 5.10 show variation of η with period for all data set. In general, except a few periods, regional skew parameter does not reach the value of 0.3.

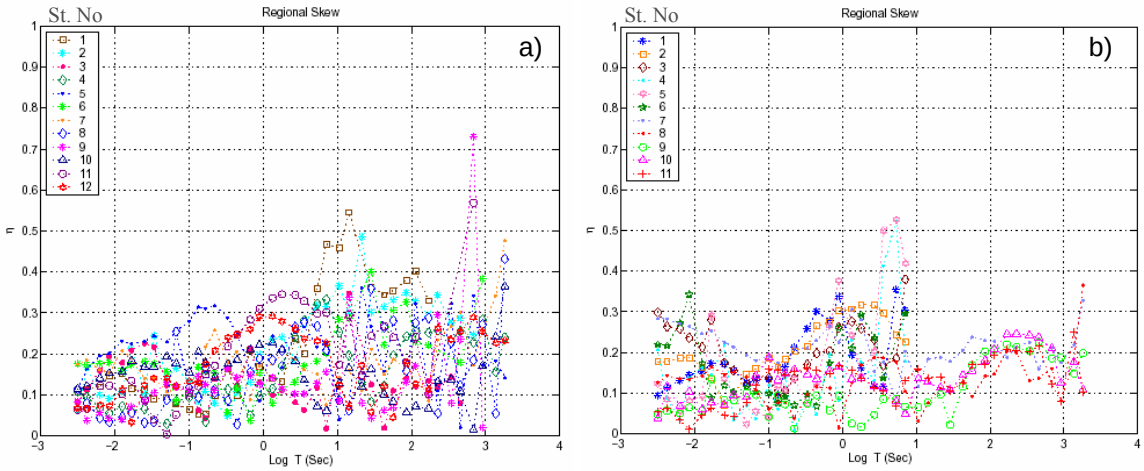

Figure 5.10. Graphs of the 3-D parameter, η, versus period for the a) DW and b) DE profiles. Numbers in legends represent stations in the profiles from the north to the south.

5.2.3. Decomposition and Strike Estimation

The dimensionality analyses represented that the data set was almost two-dimensional. After these analyses, MT data process continued with estimation of the geo-electric strike. To perform this estimation galvanic effect caused by the near surface inhomogenities had to be eliminated; otherwise the geo-electric strike would not be true. Therefore, Groom and Bailey (1989) decomposition analysis (Chapter 2, Section 3.3) was applied. Following this, the strike of the data was calculated using Swift's method (Equation 2.79).

In the application of Groom and Bailey decomposition technique with Swift's method, geo-electric strike values of every station for every period were calculated. After that, McNeice and Jones (2001) approach, which is extended form of Groom and Bailey decomposition, was applied for whole stations and whole periods. This way, geo-electric strike variation of the data for both every separate site and all sites in one profile were obtained.

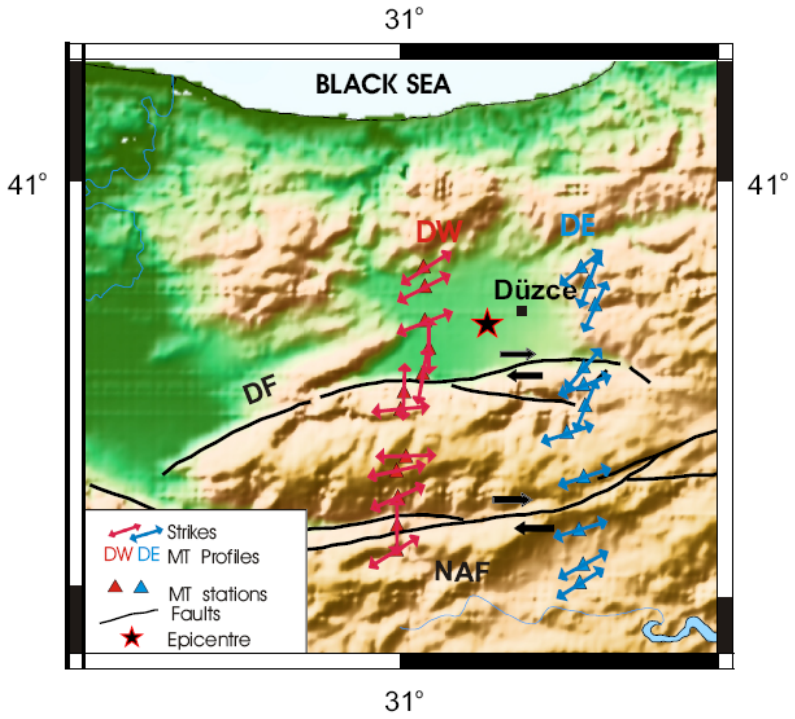

Figure 5.11. The geo-electric strike of the whole frequency band at each station. Pink and blue arrows indicate the DW and DE profiles' strike values, respectively, after Groom and Bailey.

In Figure 5.11, on most of the stations geo-electric strike demonstrates an angle greater than N65˚E. The strike of profiles was estimated as N72˚E and N70˚E for the DW and DE profiles, respectively, (Figure 5.12) by using multisite multifrequency decomposition analysis of McNeice and Jones (2001). These strike values of the undistorted MT data give high consistency with the geological strike.

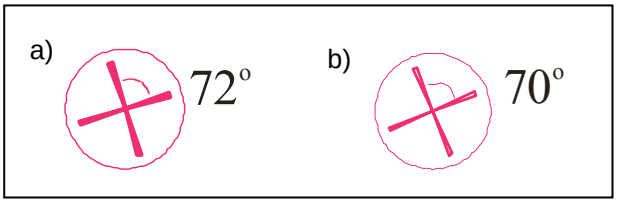

Figure 5.12. Geo-electric strikes of the whole frequency band data for the a) DW and b) DE profiles.

Next, the MT data could be rotated to the geo-electric strike coordinate frame by eliminating twist and shear effects of galvanic distortion, which are mentioned in explanation part of Groom and Bailey (1989) decomposition technique at chapter 2.3.2. Figure 5.13 represents the apparent resistivity and phase curve of the sample station Dzc1-N04, which was located in Düzce basin, calculated before and after tensor decomposition. Once the Figures 5.13-a and 5.13-b are compared, it is clearly seen that because of the N72˚E strike angle, after decomposition, XY and YX components approximately exchanged their position with little magnitude variation in resistivity. After rotating the data with Swift's method, electrically polarized (TE) and magnetically polarized (TM) modes can be defined.

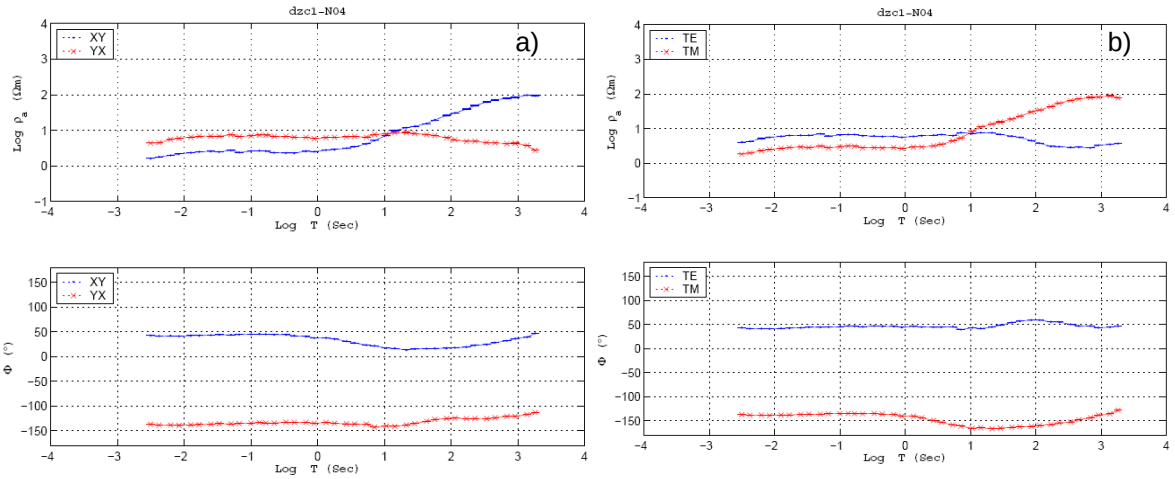

Figure 5.13. Comparison of the MT data a) before and b) after decomposition for the sample station of the DW profile, station Dzc1-N04.

Similar to Figure 5.13, Figure 5.14 shows the variation of the apparent resistivity and phase values after decomposition with 70˚ strike angle for one of the east profile station. Likewise the station dzc-N04, XY and YX modes of the station Dzc2-N07 almost exchanged their values and became TE and TM modes, respectively. Having almost the same resistivity values until 1 sec., TE and TM modes demonstrate the one-dimensionality of the data at this station. The station Dzc2-N07 was located on highlands between Düzce and NAF being nearly at the center of the east profile.

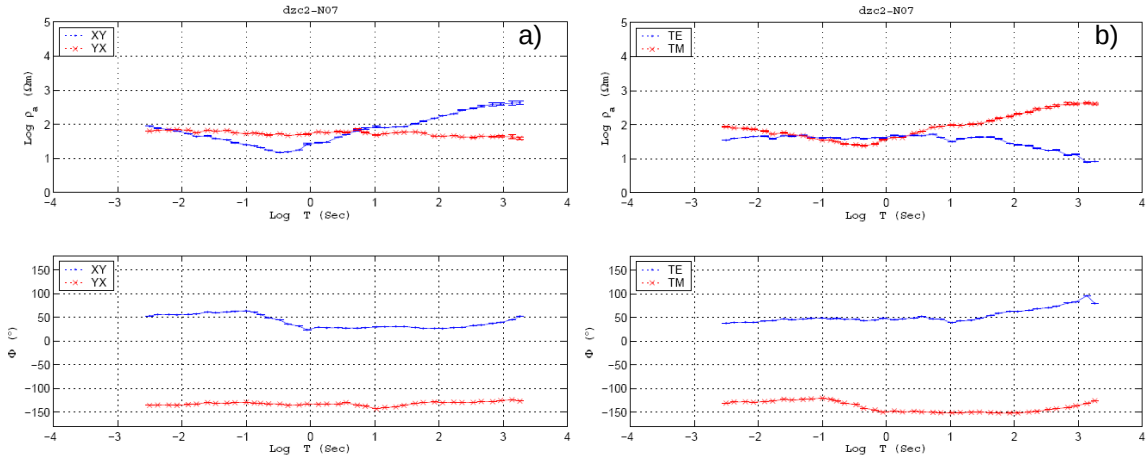

Figure 5.14. Comparison of the MT data a) before and b) after decomposition for the sample station of the DE profile, Dzc2-N07.

Figure 5.15 represents the apparent resistivity and phase curves after Groom and Bailey decomposition (1989) for all stations of the DW profile. In all stations, TE and TM apparent resistivity curves show the same shape until period of 1 sec. As it has been mentioned before, the first five stations from the north to the south has similar low apparent resistivity values ranging from 1 Ωm to 100 Ωm. These five stations are in a group (Figure 5.4-a1, 5.4-b1) which represents resistivity structure of Düzce basin having apparent resistivities between 1-10 Ωm. The next five curves in Figure 5.15 belonging to the stations located between Düzce and NAF are parts of the second group (Figure 5.4-a2, 5.4-b2) representing high mountains with higher apparent resistivity values according to the apparent resistivity values of the first five stations. Apparent resistivity values lower than 10 Ωm is not observed at these stations. The last two graphs showing the apparent

resistivity values of the stations Dzc1-N11 and Dzc1-N12 located at the south of the NAF constitute last group (Figure 5.4-a3, 5.4-b3). Although the resistivity values of the highlands give high resistivities, the decrease in resistivity at station 11 takes attention. Existence of Mudurnu valley at location of station Dzc1-N11 is the result of lower resistivity values observed on this site.

In Figure 5.16, apparent resistivity and phase values of all stations from three groups of the DE profile are represented. Similar to the DW profile, 1-dimensionality of the DE profile is emerged from consistent variations of the TE and TM mode apparent resistivity and phase values until almost 1 sec. in all stations. Since all of the stations are located on highland, higher resistivities according to the DW profile are observed along the DE profile. The increase in apparent resistivity values with period is observed on most of the stations. However, there is a distinct decrease in apparent resistivity values from the north to the south especially at stations located at the south of the NAF where Mudurnu valley exists. Though apparent resistivities do not have values lower than 10 Ωm at stations located northern of NAF, very low resistivity values such as 1 Ωm is observed at southern stations.

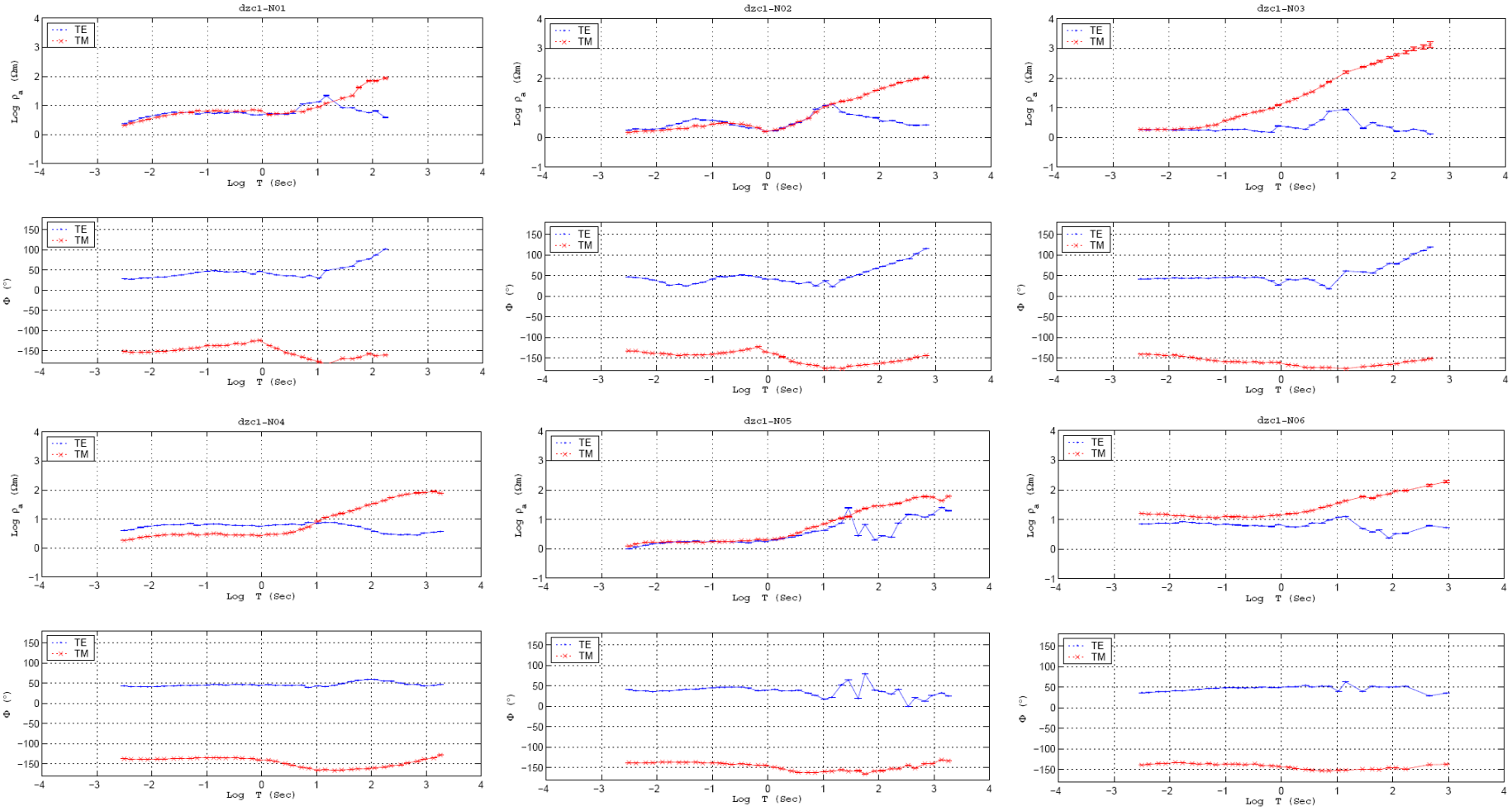

Figure 5.15-a. Apparent resistivity (Log ρ_a) and phase (Φ) curves after decomposition and rotation of stations from Dzc1-N01 to Dzc1-N06 of the DW profile from the north to the south. TE mode is represented in blue and TM mode is represented in red color.

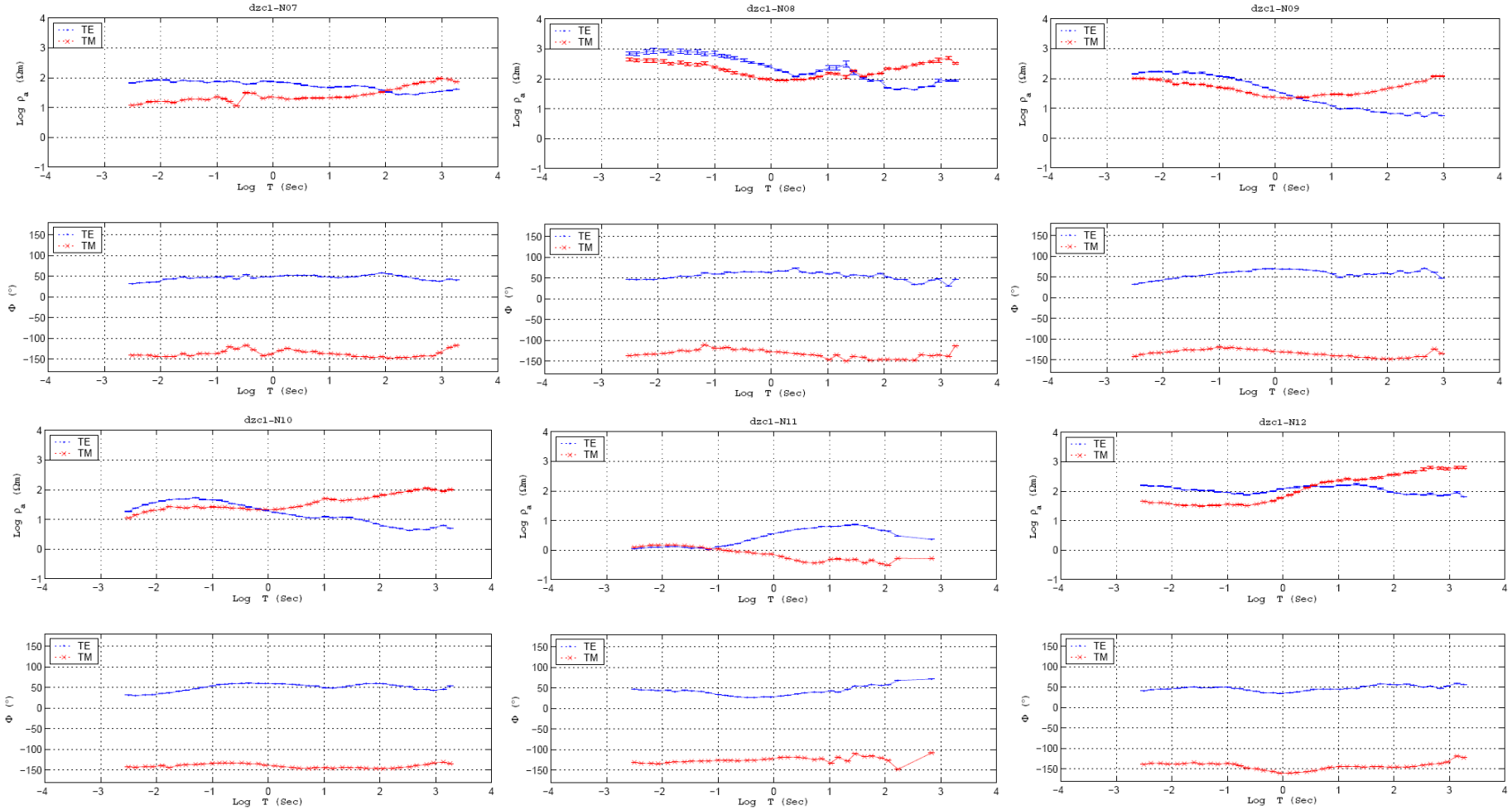

Figure 5.15-b. Apparent resistivity (Log ρ) and phase (Φ) curves after decomposition and rotation of stations from Dzc1-N07 to Dzc1-N012 of the DW profile. TE mode is represented in blue and TM mode is represented in red color.

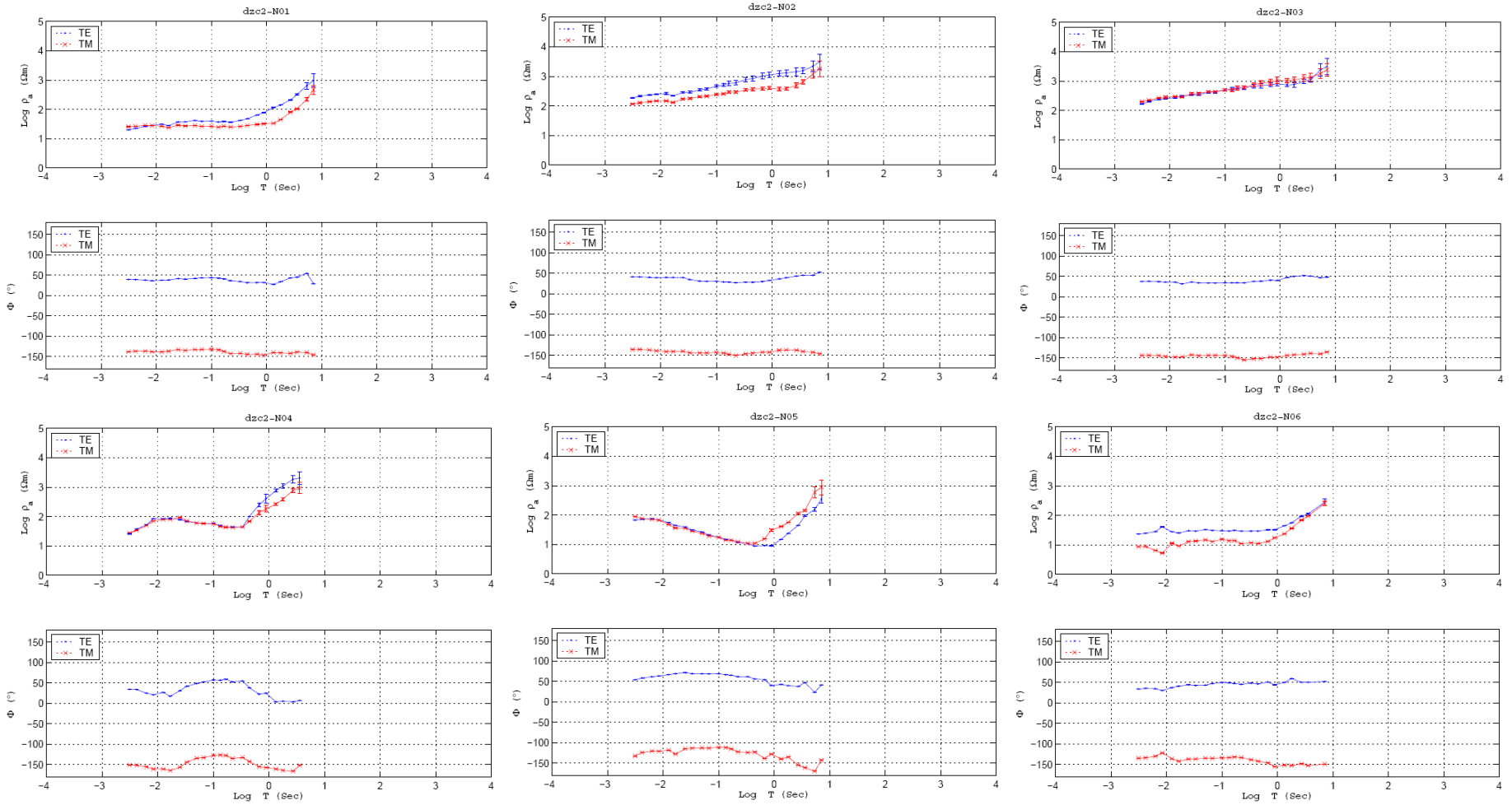

Figure 5.16-a. Apparent resistivity and phase curves after decomposition and rotation of stations from Dzc2-N01 to Dzc2-N06 of the DE profile. TE mode is represented in blue and TM mode is represented in red color.

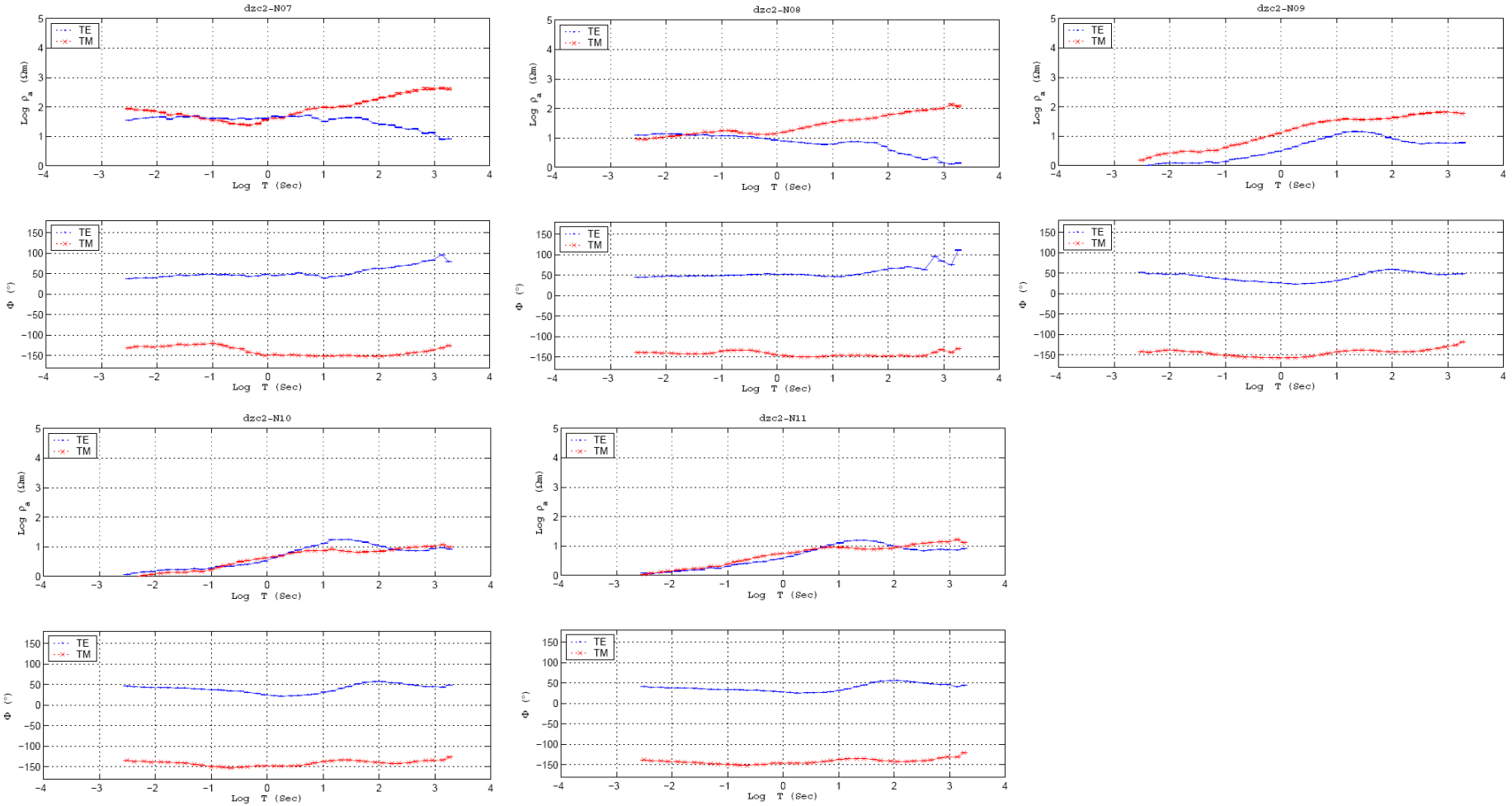

Figure 5.16-b. Apparent resistivity and phase curves after decomposition and rotation of stations from Dzc2-N07 to Dzc2-N11 of the DE profile. TE mode is represented in blue and TM mode is represented in red color.

5.2.4. Inversion of MT Data

In previous part, the target was to analyze the MT responses recorded in the field and to make the data suitable for inversion. For this aim, dimensionality of the data was estimated and two of three effects of galvanic distortion, twist and shear effects, were removed from the data. For the interpretation of the electrical resistivity structure of the field, the MT data had to be converted from frequency domain apparent resistivity and phase into electrical resistivity earth model depending on depth and horizontal distance. Therefore, after the MT data of the DW and DE profiles estimated as two-dimensionally and was rotated to the geo-electric coordinate frames, the data set was inverted by using two-dimensional inversion code of Ogawa and Uchida (1996). The reason why this code was used is that for Tikhonov regularization of the data in inversion process, all inversion codes minimize misfit between the observed and calculated data by using roughness of the model structure as a constraint, addition to roughness, Ogawa and Uchida's code also use static shift as a constraint and minimize the static shift effect in inversion.

In the beginning of inversion process, rotated TE and TM apparent resistivity and phase data were used. Initial model was uniform Earth having electrical resistivity of 100 Ωm. For each of the profiles, many combinations of each parameter in inversion process were tried. The smoothing parameter, *sm*, gave smoother models for its larger values. However, the increase in *sm* value caused higher r.m.s. The smoothest models being in good consistency with the observed data for the DW and DE profiles are obtained (Figure 5.17) for the model parameters given in Table 5.1.

Table 5.1. Inversion parameters used to obtain the smoothest and best fitting models for the west and east profiles.

Inversion Parameters for the west and east profiles	
Input data	TE and TM apparent resistivity (ρ_a) and phase (Φ) values after decomposition without static shift correction
Frequency range	320-0.0005 Hz
Smoothing parameter (sm)	15
Static Shift parameters (ss)	15
Error floor	10% for ρ_a and 5% for Φ (for both modes)
Weighting function (w)	1
Iteration No. (IN)	15
r.m.s.	~2

In Figure 5.17 the optimal resistivity model for the DW profile is shown. The first conductor zone (<4 Ωm) symbolized by C1 exists at south of NAF. This zone located at Mudurnu valley has almost 1 km thickness. To the north of the profiles small resistive layer (R1) is observed. This resistive block is followed by the conductor layer C2 to the north of the DW profile. C2 takes place beneath the Düzce basin and extends until the end of the profile.

Through the deeper parts of the region, a conductor layer (C3) located almost beneath the high mountains is shown. At the deepest parts of the profile a conductor layer (C4) located at ~10 km depth extends from the south edge to the almost center of the profile. At the north edge, between the conductor blocks, a resistor block (R2) is observed.

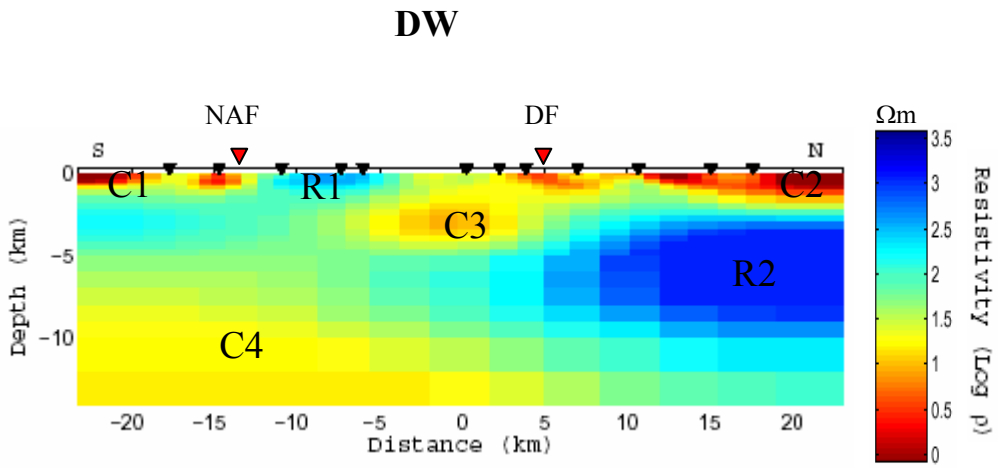

Figure 5.17. Final resistivity model for the DW profile obtained using joint inversion of the TE and TM mode data. Black triangles at the surface represent the MT stations. Red triangles indicate NAF and Düzce fault from the south to the north, respectively. Color variation in models from red to blue denotes increase in resistivity.

Figure 5.18 denotes the final resistivity model for the DE profile. At surface layers of the DE profile, the first conductor zone (<3 Ωm) symbolized by C1 extends from the south edge of the DE profile through the NAF. The thickness of the C1 located at Mudurnu valley is about 1 km.

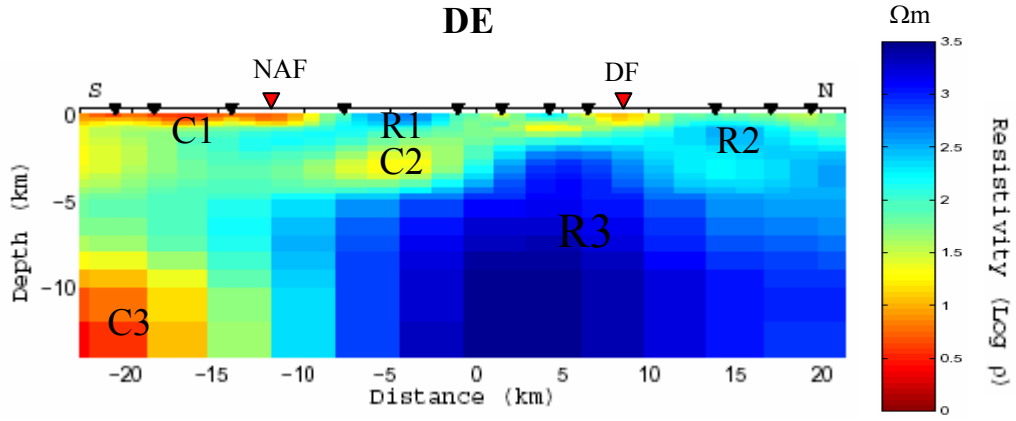

Figure 5.18. Final resistivity models for the DE profile obtained using joint inversion of the TE and TM mode data. Black triangles at the surface represent MT stations. Red triangles indicate NAF and Düzce fault from the south to the north, respectively. Color variation in models from red to blue denotes increase in resistivity.

To the north of the profile small resistive layer (R1) and beneath this resistive block, a small conductor layer C2 is observed. At the north of the profile, beneath the trace of the Düzce fault another small conductor layer is seen. At the north edge of the profile a resistive layer R2 is located. Through the deeper of the region a conductor layer (C3) takes place at ~10 km depth. A highly resistive layer R3 extends from the center of the profile to the north edge.

5.3. Analysis of Inversion Results

The final resistivity models for the DW and DE profiles have been investigated in previous part. Hereby, fitting of the observed and calculated data obtained as a result of inversion of the MT data using the parameters given in Table 5.1 will be analyzed.

In Figure 5.19, the pseudosections obtained from the calculated and observed apparent resistivity and phase values of TM (Figure 5.19-a) and TE (Figure 5.19-b) modes of the west profile are represented. The two Figures on the left hand side (a-1) show calculated (upper) and observed (bottom) apparent resistivity of the DW profile versus frequency. On these two Figures, apparent resistivity variation of the DW profile from the north to the south is shown from the right to the left. The same illustration for the calculated and observed phase variation of this profile as a function of frequency is given on the right hand side (Figure 5.19-a2). Below the apparent resistivity and phase pseudosections of the TM mode, the same Figure configuration related to calculated and observed apparent resistivity and phase variation of the TE mode is presented (Figure 5.19-b1 and 5.19-b2). In TM and TE pseudosections, it is observed that apparent resistivity and phase amplitudes are almost well recovered. However, shape recovery is better than the amplitude recovery. The TM and TE pseudosections also well represent the variation of the apparent resistivities of the region in three groups mentioned in the previous chapters from the north to the south.

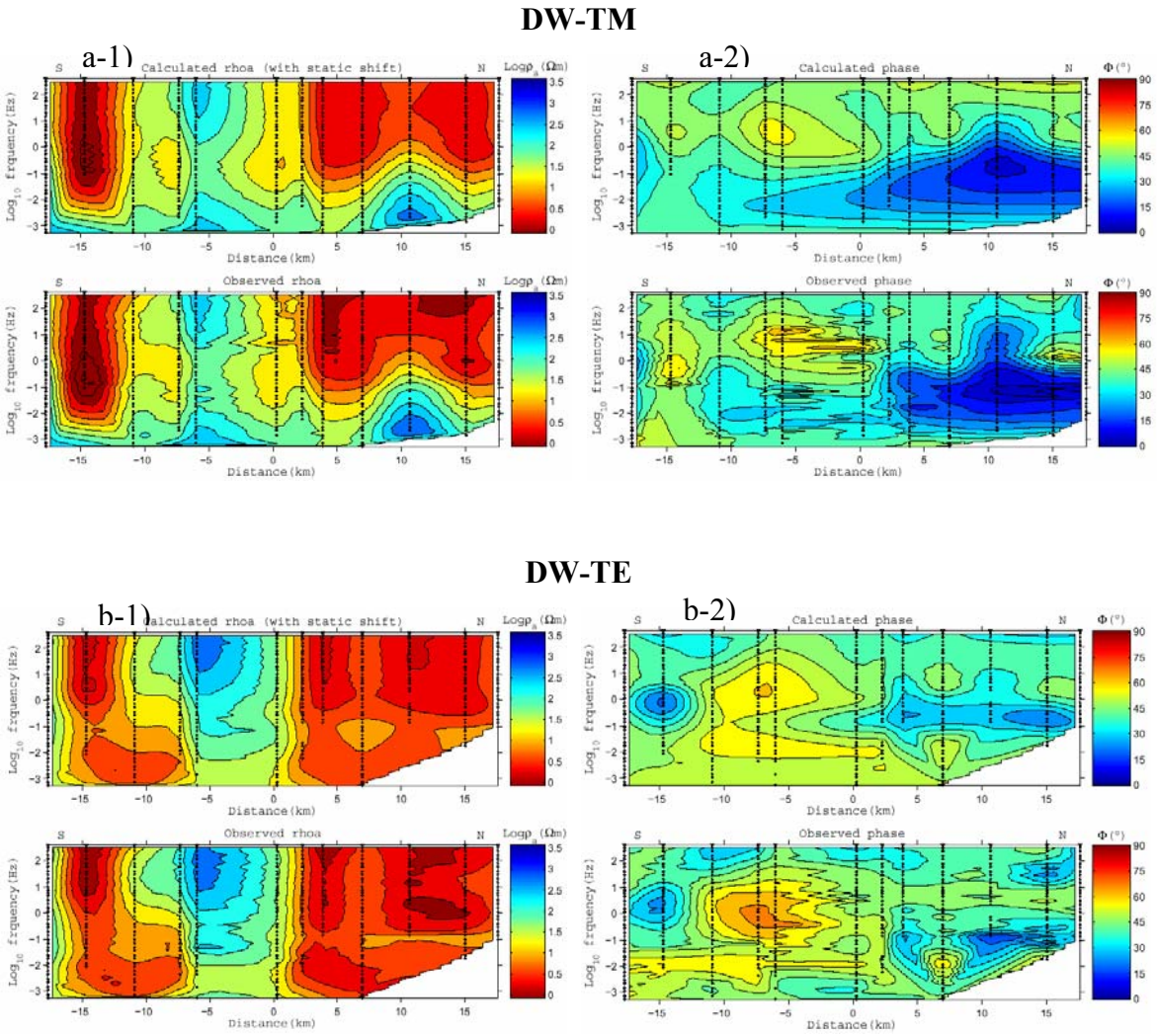

Figure 5.19. Calculated and observed apparent resistivity and phase pseudosections. a-1 and a-2 represent apparent resistivity and phase pseudosections of TM mode respectively for calculated (upper) and observed (bottom) data. b-1 and b-2 represent the same situation for TE mode. In pseudosections high resistivity is indicated by blue whereas low resistivity is indicated by red color.

In Figure 5.20, calculated and observed apparent resistivity and phase pseudosections of TM and TE modes are given for the DE profile. The Figure configuration for the DE profile is the same with the DW profile. It is seen in both TM and TE modes that the fit of apparent resistivity data as shape and amplitude is good. Although generally there is a good agreement between the observed and calculated phase values on both TM and TE modes, the effect of noise still exists in some parts of the phase pseudosections.

DE-TM

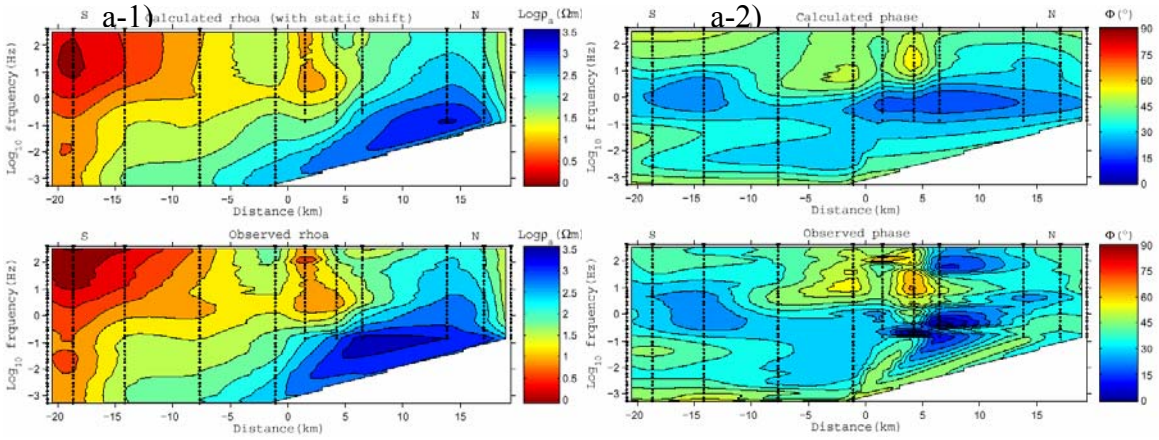

DE-TE

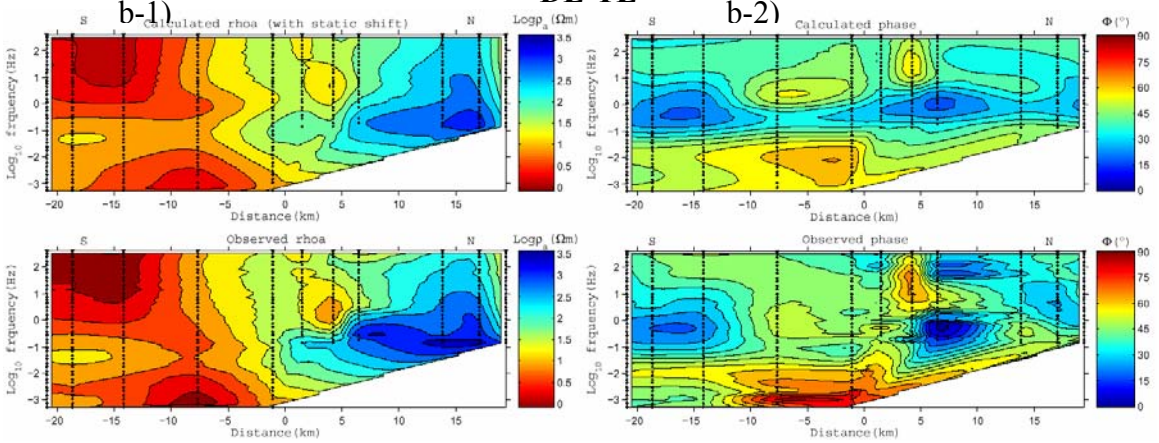

Figure 5.20. Calculated and observed apparent resistivity and phase pseudosections. a-1 and a-2 represent apparent resistivity and phase pseudosections of TM mode respectively for calculated (upper) and observed (bottom) data. b-1 and b-2 represent the same situation for TE mode. In pseudosections high resistivity is indicated by blue whereas low resistivity is indicated by red color.

The correlation of the observed and calculated apparent resistivity and phase values was also observed in fitting curves of TE and TM modes. In Figure 5.21, TE fitting curves for all stations from the north to the south of the DW profile are shown. Well coherency between the calculated and model response data is observed on the all stations except a few. And generally, as it's seen from the Figures, the coherency of apparent resistivity is

better than the phase. On the other hand, TM fitting curves (Figure 5.22) indicate greater coherency between the observed and calculated data for both apparent resistivity and phase variations. It is mostly because of the fact that TE mode is more affected by the galvanic distortion caused by the three-dimensional features located at the near surface (Wannamaker *et al.*, 1984). For instance; the fitting in TE mode at station Dzc1-N02 is poor until 0.1 sec. and after this period fitting gets better. Whereas fitting of the same station is better for TM mode. In TM mode phase fittings, though the model response is out of the error bars of the observed data at some of the stations, the shape of the data curve is recovered.

In Figure 5.23 and 5.24, correlation of the model response with the observed data of the DE profile is represented for the TE and TM modes, respectively. Well fitting in apparent resistivity and phase curves at southern five stations, which were settled during the first field campaign, is appreciable in both modes, especially in TM mode. As it is observed at DW profile, TE mode fittings are poor than the TM mode's as a result of the same cause mentioned for the DW profile. Apparent resistivity responses along the all stations fit better than the phase responses at all stations. It stems from the smaller standard error used for phase fitting according to the apparent resistivity fittings. However shape recovery on phase fittings is generally well.

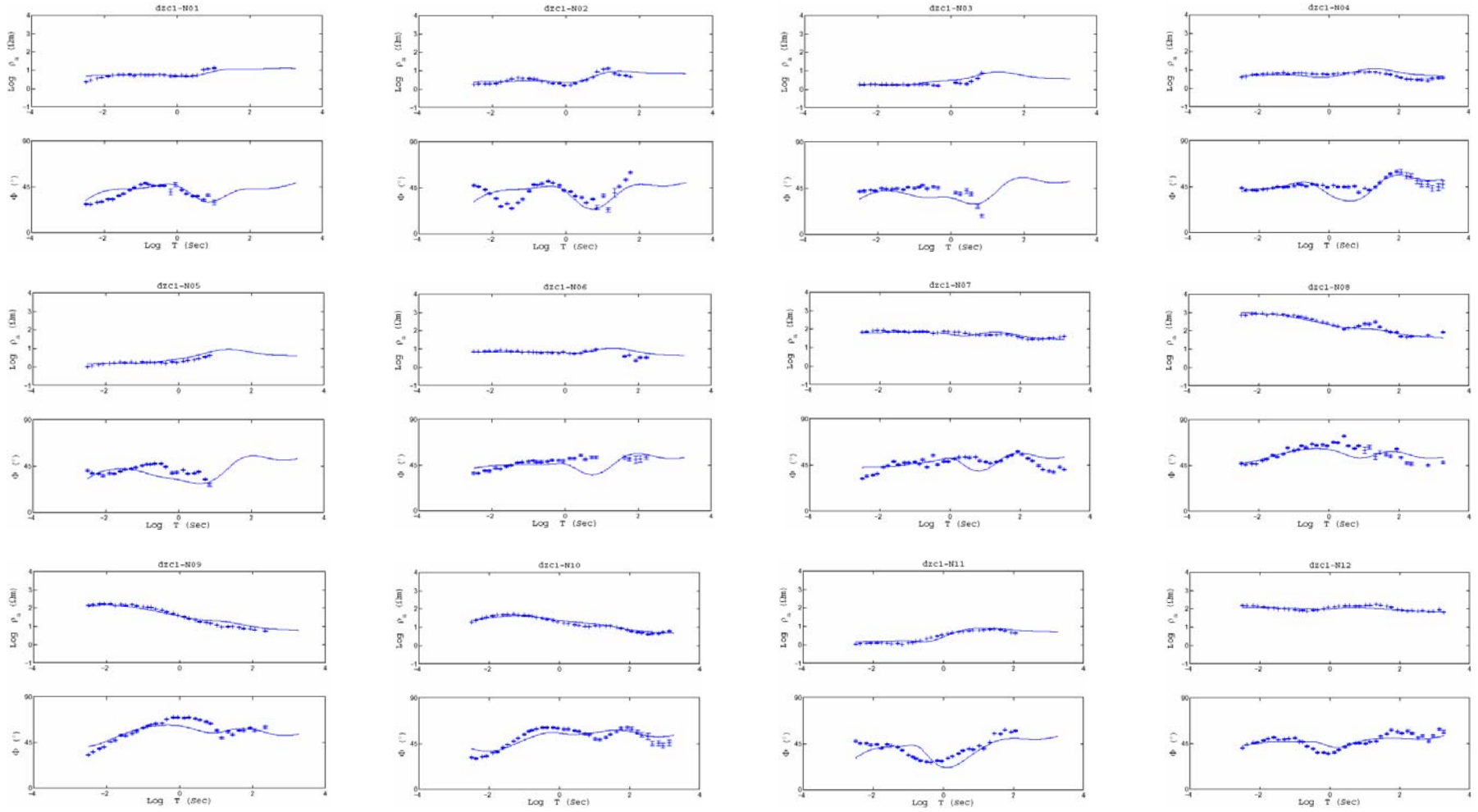

Figure 15.21. Fitting curves of observed and calculated data obtained from TE mode of the DW profile. Dotted lines with error bars demonstrate observed data while solid lines represent the model response.

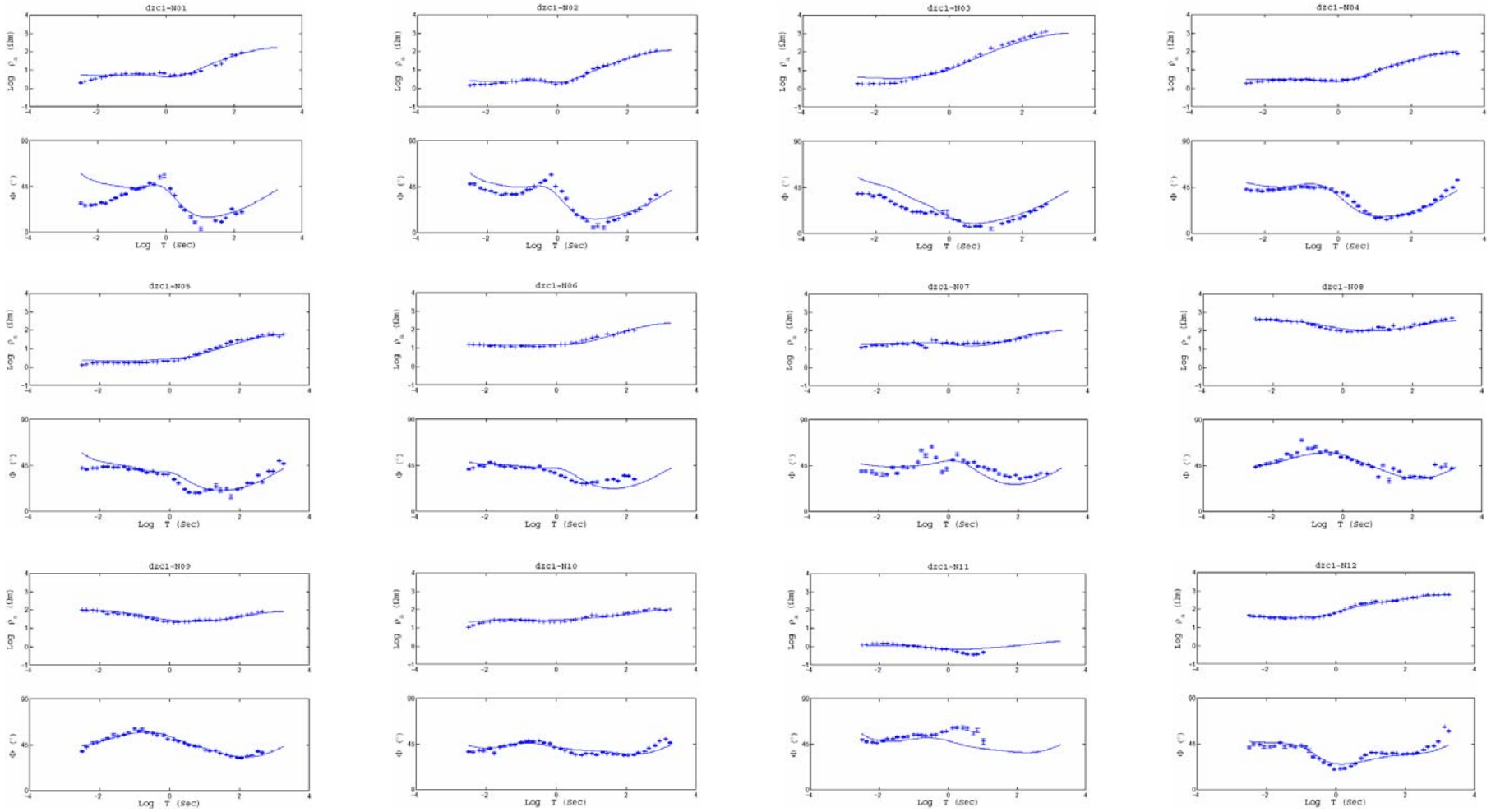

Figure 15.22. Fitting curves of observed and calculated data obtained from TM mode of the DW profile. Dotted lines with error bars demonstrate observed data while solid lines represent the model response.

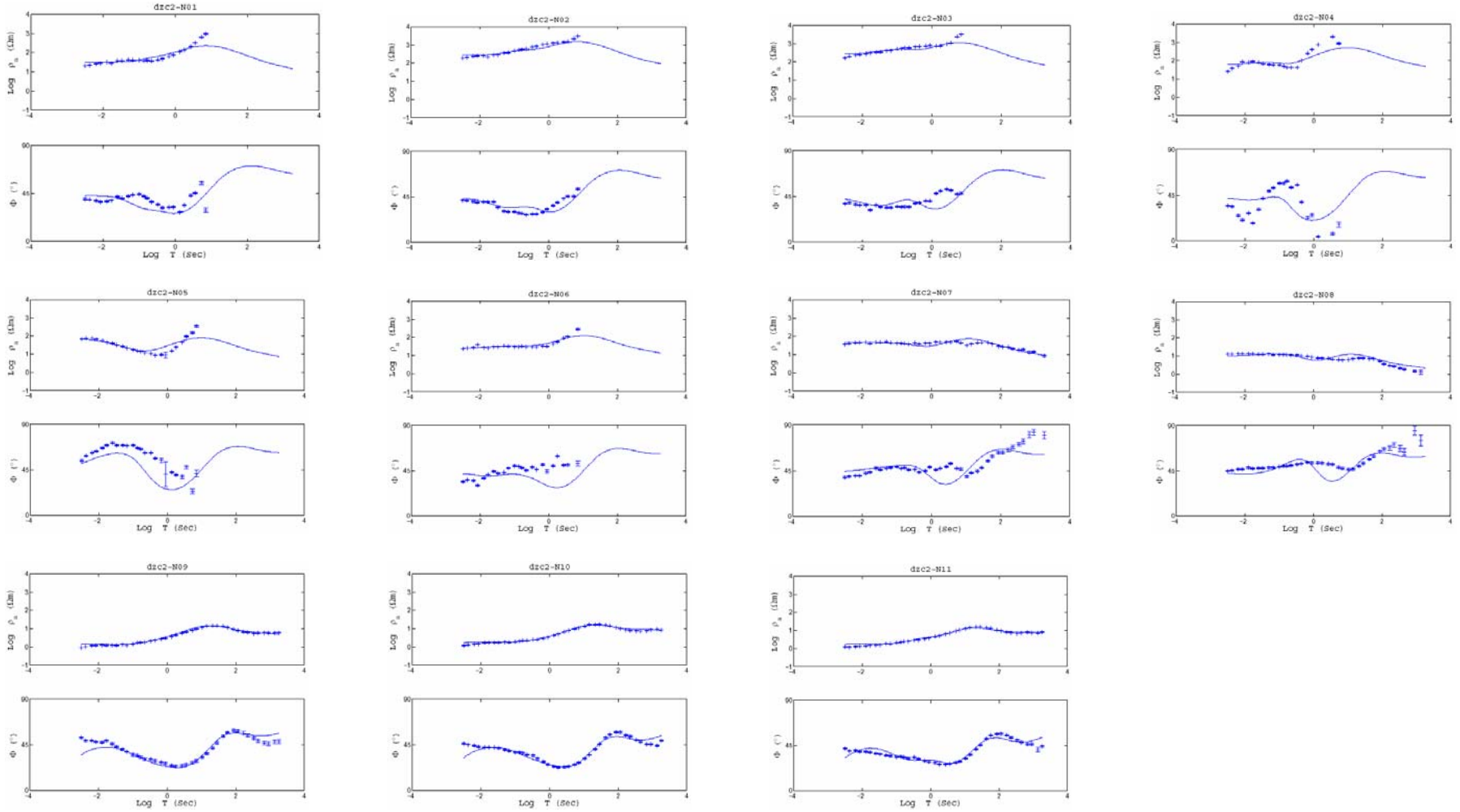

Figure 15.23. Fitting curves of observed and calculated data obtained from TE mode of the DE profile. Dotted lines with error bars demonstrate observed data while solid lines represent the model response.

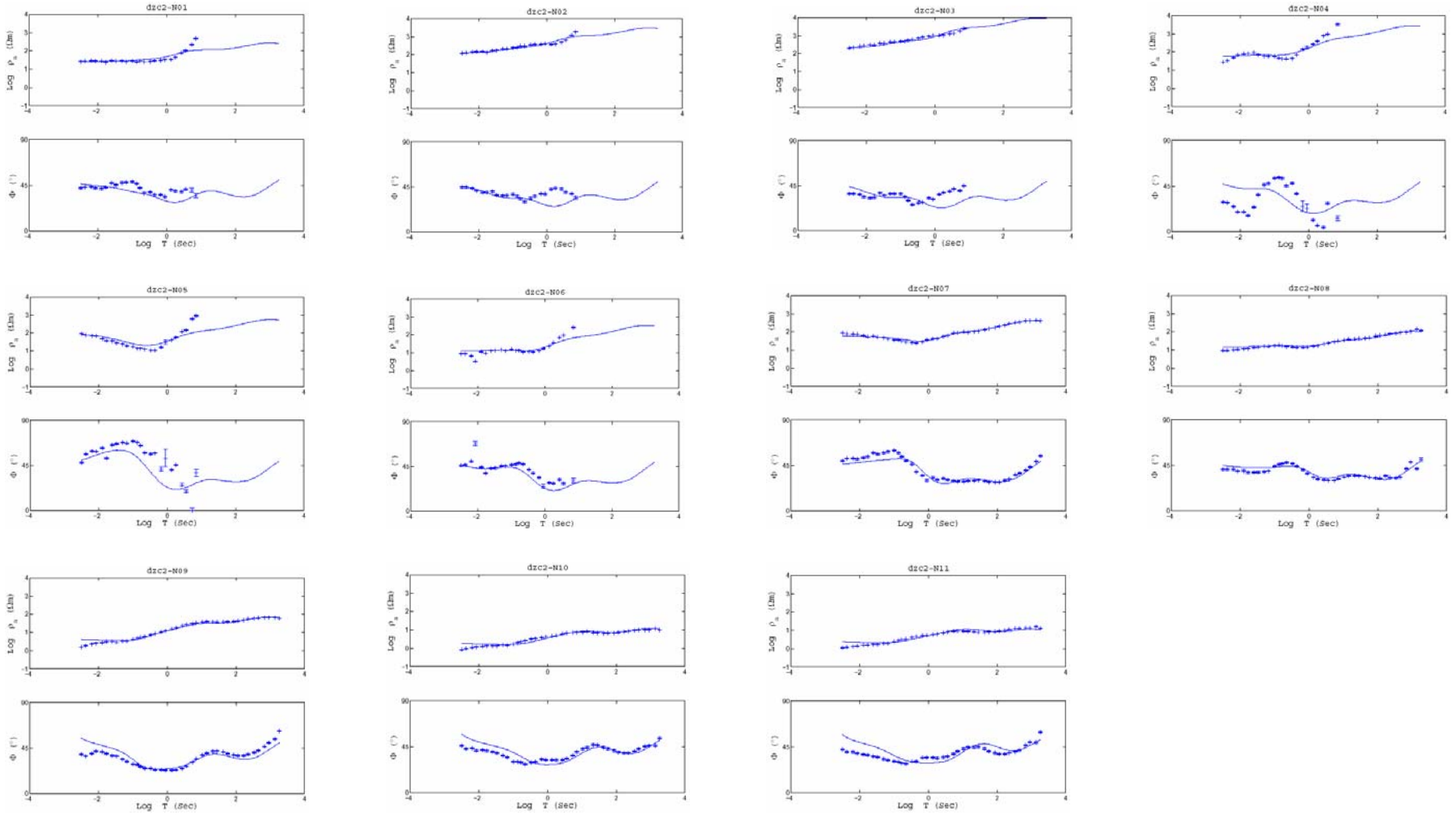

Figure 15.24. Fitting curves of observed and calculated data obtained from TM mode of the DE profile. Dotted lines with error bars demonstrate observed data while solid lines represent the model response.

6. DISCUSSION

Turkey is the one of the seismically active region in the World. With the aim of investigating earthquake and fault parameters, lots of methods such as geological, seismological and geodetic methods are used. A widely used method in examining the fault zone structure is MT method because of its high capability in structural imaging of the fault zones.

Once the devastating Düzce earthquake occurred in 1999 (Mw:7.2), the parameters of the earthquake and fault were well investigated by geoscientists using seismological, and geodetic data (Ayhan *et al.* 2001; Bouchon *et al.*, 2001; Bürgmann *et al.*, 2002; Çakır *et al.,* 2004; Bouin *et al.*, 2004; Birgören *et al.*, 2004). Some results of the studies about the Düzce earthquake and Düzce fault were interesting such that the Düzce fault rupture had a dip to the north. During the earthquake, the rupture velocity on eastern side of the earthquake's epicenter was much greater than the rupture velocity on western side (Bouchon *et al.*, 2001; Bouin *et al.*, 2004; Birgören *et al.*, 2004). Additionally, there were two asperity zones in the region that the larger one observed near the hypocenter and the smaller one existed at shallow part of the eastern side of the epicenter (Birgören *et al.*, 2004). Therefore, the MT method was applied to image the Düzce fault's electrical resistivity structure in order to examine resistivity contrast on the western side with the eastern side of the epicenter. Thus, MT data on both sides of the epicenter were obtained.

Once observed apparent resistivity and phase curves of XY and YX modes in frequency domain (Figures 5.2 and 5.3) were investigated, it is seen that the region separates into three distinct groups from the north to the south due to the electrical resistivity variation in the region (Figure 5.4-5.5). These three groups represent parts of the western Pontides in the region which are the İstanbul-Zonguldak zone, Armutlu-Almacık zone, and Sakarya continent form the north to the south. (Yılmaz *et al.*, 1997; Yiğitbaş *et al.*, 1999).

Another significant point noticed from the investigation of observed data is that the data is 1D until 0.1 sec. This condition is also confirmed by the dimensionality parameters. Both Swift's (1967) skewness parameter and Bahr's (1991) dimensionality parameters denote one-dimensionality at the surface. Once Bahr's parameters and skewness parameter considered for the all period range, the results of the dimensionality estimation show that MT data obtained along two parallel profiles on the western and eastern parts of the Düzce earthquake's epicenter are generally two dimensional (Figure 5.7-5.10).

Geo-electric strike of the data is an important concept for the MT method. According to the strike estimation methods, the strikes were obtained as N72˚E and N70˚E for the DW and DE profiles, respectively, (Figure 5.10, and 5.11). Akyüz *et al.*, (2002) determined the geological strike by using field observations and found out that the geo-electric strike varies a range between N75˚E-N105˚E. Geodetic and seismologic studies also give the geological strike within this range (Ayhan *et al.* 2001; Bürgmann *et al.*, 2002; Çakır *et al.,* 2003; Bouin *et al.*, 2004). The geo-electric strike obtained by means of Groom-Bailey and McNeice and Jones approaches in the region is consistent with the geologic strike. Higher strike values which have better consistency with the geologic strike were also obtained at nearer stations to the Düzce fault and NAF (Figure 5.11) but these values do not represent the regional geo-electric strike of the region.

The apparent resistivity and phase pseudosections obtained after decomposition and rotation well denote the electrical resistivity transition in three parts (Figure 5.19-5.20). High conductivity values in the apparent resistivity pseudosections indicate surface conductive layers in the earth-models because of the skin depth definition. One-dimensionality of the data at surface which is also determined by the dimensionality parameters is noticed once TE and TM apparent resistivity and phase pseudosections are compared.

The electrical resistivity models represented in Figures 5.17 and 5.18 clearly show that the same surface structures except Düzce basin are observed on the DW and DE earth-models until the depth of ~3-4 km. North of the DW profile, Düzce basin composed of young sediments is observed at a depth of ~3 km as surface conductor (C2 in Figure 5.17). Şengör *et al*., (2005) determined thickness of the sedimentary layer as nearly 260 m. The continuation of the conductor until the depth of ~3-4 km was interpreted as the effect of Eocene volcanogenic flysch extending beneath the Düzce basin (Şengör *et al*., 2005). However, a low resistivity zone is seen at the same depth of the DE profile (R2 in Figure 5.18). The reason of this situation is that northern stations of the DE profile do not take place within the Düzce basin. This resistive layer observed northern DE profile is most probably controlled by the Paleozoic successions mudstone and sandstone in the region (Yılmaz *et al.*, 1997). South of the profiles, a 2-3 km thick conductor, which is composed of late Cretaceous age ophiolitic mélange (Yılmaz *et al.*, 1997; Yiğitbaş *et al.*, 1999), exist beneath the Düzce fault trace. This conductor is followed by the low conductive layer almost overlain by the resistive layer (C3 - R1 in Figure 5.17 and C2 - R1 in Figure 5.18) at the highland between Düzce fault and NAF. These two layers represent the variation of the metamorphics in the Almacık mountains. A conductive layer at a depth of 1 km is present below the NAF trace which is followed by another conductive layer to the south, until the end of the profiles (C1 in Figure 5.17 and 5.18). These two conductors are interpreted as younger sediments located near the fault zone and Mudurnu Valley.

At deeper parts, the DW and DE electrical resistivity models represent different structures. From ~7 km to ~14 km depth, a conductive layer becoming deeper to the north extends from the south edge to the center of the DW profile. This conductor layer with resistivity of ~20 Ωm was also observed on apparent resistivity and phase curves for higher periods at southern stations of the DW profile and represent İzmit metamorphic sequence which also observed north of the Sakarya continent (Yılmaz *et al.*, 1997). At a depth from ~4 km to ~10 km, a resistive layer (R2 in Figure 5.17) with resistivity of a few hundred Ωm extends from the center to the northern edge of the DW profile and to the depth its resistivity gets lower. On the other hand, southern edge of the DE profile indicates a smaller conductive layer which has higher conductivity according to the conductive layer at the south end of the DW profile. From shallow depths to the 14 km, the high resistive

layer extends almost along the DE profiles with resistivity of a few thousand Ωm (R3 in Figure 5.18). The resistivity (R3 in Figure 5.18) obtained on deeper parts of the DE profiles is greater than the resistivity (R2 in Figure 5.17) of the DW profile which both represent Istanbul-Zonguldak zone.

Once the crustal fluid resistivity is assumed as 0.04 (Nesbitt, 1993) and *m* is taken as 2, the porosities of the resistive (R3 and R2) and conductive (C3) layer on the DE model (Figure 5.18) are estimated from Archie's law (Equation 2.1) as 0.3%, 1.4%, and 10%, respectively. At western side, R2 and C4 have the porosities of 0.7% and 5%, respectively. Sharp porosity variations in the models represent the sudden variation of the geologic structures in the region.

As it is seen from the Figures (5.17, 5.18) the 2-D electrical resistivity models well denote the structures of the western Pontides. Resistive layers at northern part of the both models represent İstanbul-Zonguldak zone which is the northernmost part of the western Pontides. In the DW model, this resistive layer R2 sharply last near the Düzce fault and low resistive layer starts. This vertical boundary is observed until the depth of 10 km. To the deeper after this depth, the conductive layer dips to the north beneath R2. Çakır *et al.*, (2003) mentioned a possibility in their study that Düzce fault is a vertical fault and it crosses an old trust fault dipping to the north. Transition from the resistive layer to the conductive near Düzce fault may be the indicator of this structure.

In the DE model, the resistive layer (R3) which is an extension of Istanbul-Zonguldak zone, starts at the northern edge of the profile and extends until the north of the NAF where Armutlu-Almacık zone of the western Pontides ends and Sakarya continent begins. Vertically this layer continues to the deeper due to the R2 in DW profile. This fundamental difference between two resistive layers may be the reason of higher rupture velocity observed eastern part of the epicenter during Düzce earthquake. Additionally, Birgören *et al.*, (2004) determined two-asperity zones in the region that the larger one is located near hypocenter and small one is located at shallow part. These asperity zones are

interpreted as high seismic velocity zones and location of them mach with the high (R3) and low (R2) resistive layers which represent high seismicity in the eastern Düzce earthquake epicenter.

The models of the MT study applied by Elmas and Gürer (2004) at eastern İzmit give similar outcomes to 2D inversion results of DW profile. The MT data used in the study of Elmas and Gürer (2004) were acquired from a profile which crosses İstanbul-Zonguldak and Armutlu-Ovacık zones and Sakarya continent from the north to the south. Their results show higher resistive layer beneath the Istanbul-Zonguldak zone and Sakarya continent. Between these zones, similar electrical resistivity transition is observed from surface to depth on both models. Similar to the results of DW profile, they represent high conductivity beneath the Sakarya continent and this layer is interpreted as an identification of partial melting or related to age difference between the geologic structures of the region.

2D electrical resistivity models also good correlate with the MT study of Tank *et al.*, (2005) on western part of the NAF. These two regions have similar geologic and tectonic structure (Yılmaz *et al.*, 1997). Both of these regions cross western Pontides from the north to the south. Their results denote resistive Istanbul-Zonguldak zone like 2D electrical resistivity model of Düzce region. To the south, there is a transition to the conductor layer in both İznik and Düzce models. However, at Sakarya continent their results differ from our results. The difference between two models may arise from that their profiles are longer than ours. Most probably our results represent part of the Sakarya continent near the Armutlu-Almacık zone, but their results include greater part of this continent.

2D resistivity models include the information from both apparent resistivity and phase data of the TM and TE modes, therefore, these final models well image the resistivity distribution of the region. High consistency between observed and calculated apparent resistivity and phase curves (Figure 5.19-5.20) and match of fitting curves on most of the stations (Figure 5.21-5.24), and low r.m.s. values obtained as result of inversion represent accuracy of the final models.

7. CONCLUSION

MT data were acquired at 23 stations along two parallel profiles on western and eastern sides of the Düzce earthquake epicenter with the aim of imaging electrical resistivity distribution of the region and revealing resistivity contrast between the western and eastern sides.

According to the magnetotelluric method data processing, the geoelectric strike for the DW and DE profiles were calculated as N72˚E and N70˚E, respectively. This strike angle is consistent with the geologic strike. The final electrical resistivity models that agree well with the tectonic and geologic structure in the region were obtained as a result of 2D inversion. As it is noticed from the DW and DE Earth models, MT method is a useful tool imaging transition of tectonic zones. DW and DE final models well represent the transition of the geologic units and resistivity distribution of the Istanbul-Zonguldak zone and Sakarya continent and their tectonic mixture Armutlu-Almacık zone. In the electrical Earth model of the DW profile, transition from the resistive to the conductive layer from the north to the south to a depth of ~10 km beneath the Düzce fault and dipping of this conductive layer to the north beneath this resistive layer (Figure 5.19) may be the indicator of vertical Düzce fault and north dipping structure as claimed by Çakır *et al.*, (2003). However, dense station coverage is necessary to confirm this situation. The high (R3) and low (R2) resistive layers in the DE model (Figure 5.20) indicate asperity zones in the region and high seismic velocity zones. According to this circumstance, existence of higher resistive layer on eastern side (DE profile) of the epicenter relative to the western side (DW) and its continuation to the deeper parts may be the reason of both high seismic activities in the region, which is confirmed by the aftershock distribution of Düzce earthquake, and relatively high rupture velocity of eastern side occurred during the Düzce earthquake.

APPENDIX A: APPARENT RESISTIVITY AND PHASE CURVES OF THE WEST PROFILE BEFORE GB DECOMPOSITION

The following pages (93-98) denote the apparent resistivity and phase curves of the west (DW) profile before decomposition and rotation. In figures, site names are termed according to station numbers in the profile from the north to the south. For instance, Dzc1-N01 represents the northernmost station of the DW profile. Dzc is the abbreviation of Düzce and number 1 following the abbreviation means that this is the first, in other words DW profile. XY and YX mode apparent resistivity and phase curves are indicated with doth and cross symbols, respectively.

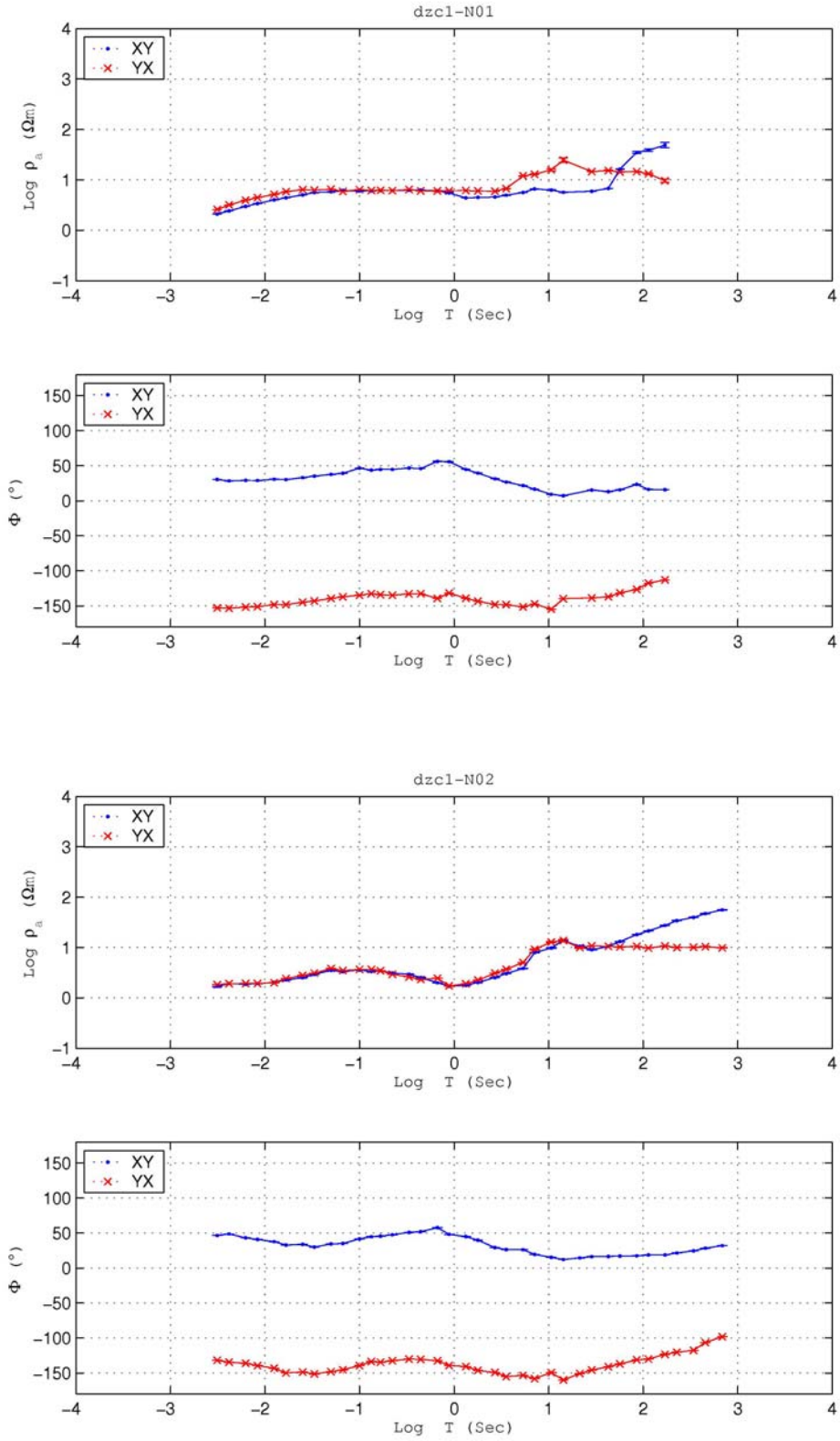

Figure A.1. Apparent resistivity and phase curves before decomposition and rotation for the stations Dzc1-N01 and Dzc1-N02 of the DW profile, respectively.

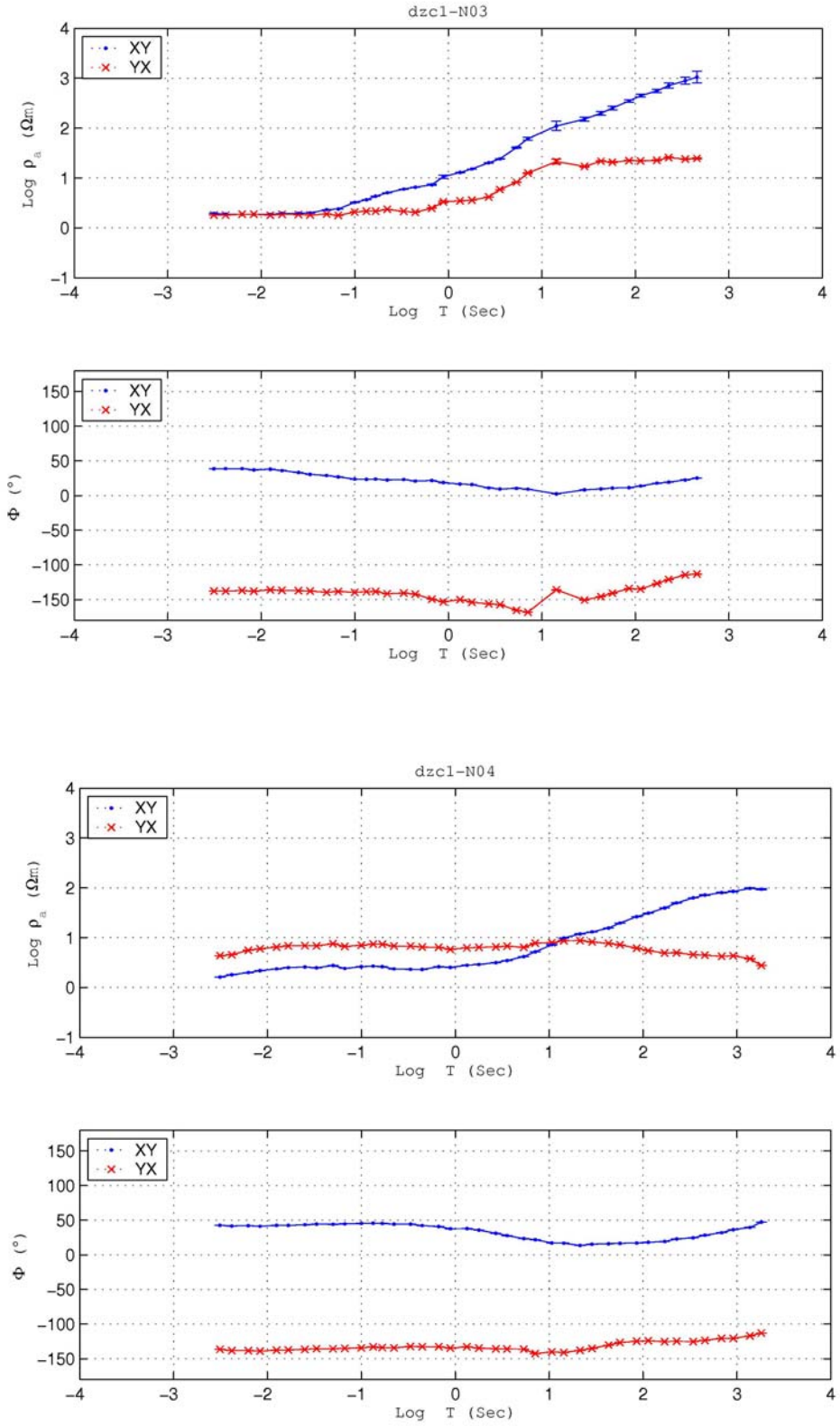

Figure A.2. Apparent resistivity and phase curves before decomposition and rotation for the stations Dzc1-N03 and Dzc1-N04 of the DW profile, respectively.

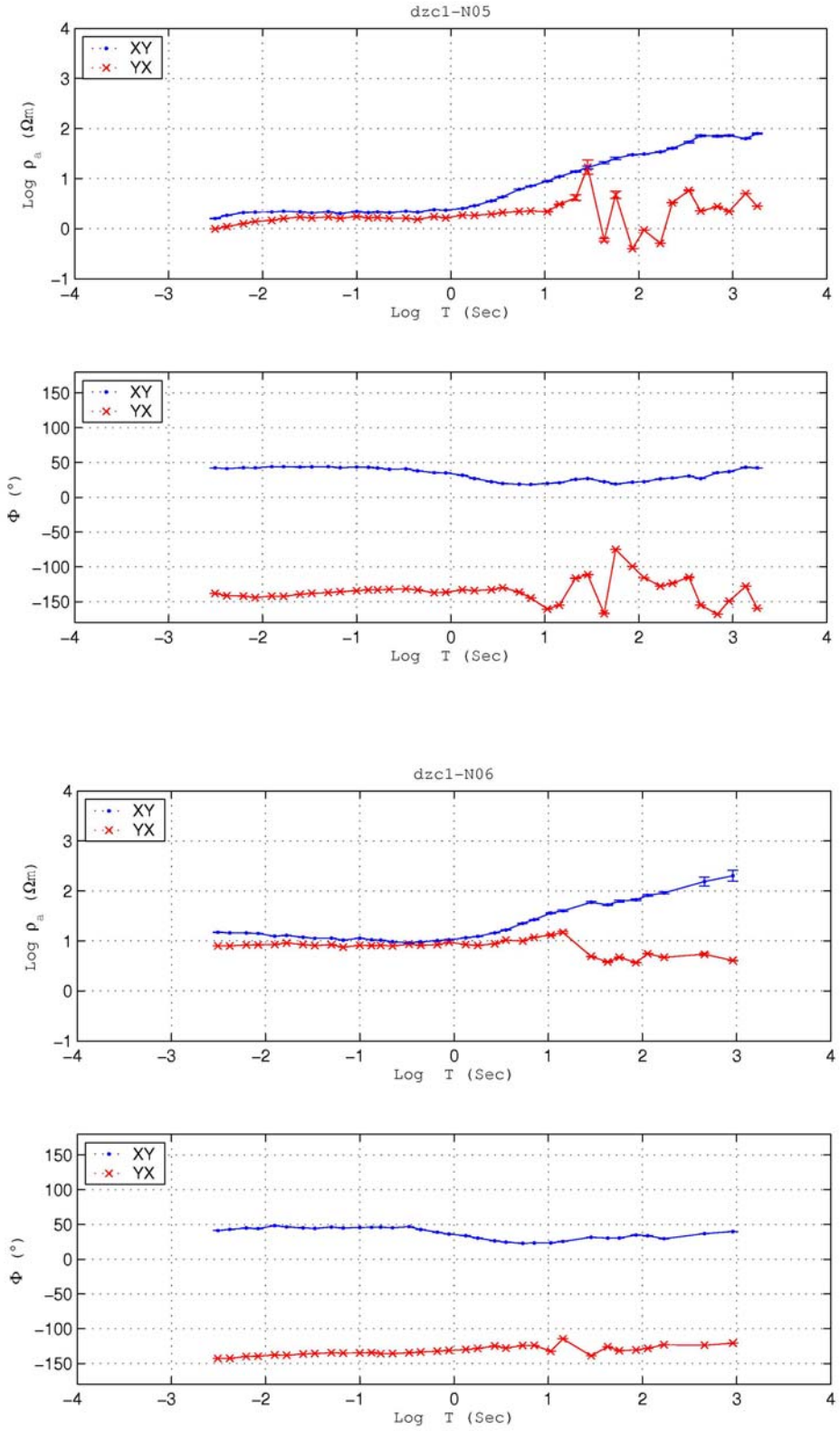

Figure A.3. Apparent resistivity and phase curves before decomposition and rotation for the stations Dzc1-N05 and Dzc1-N06 of the DW profile, respectively.

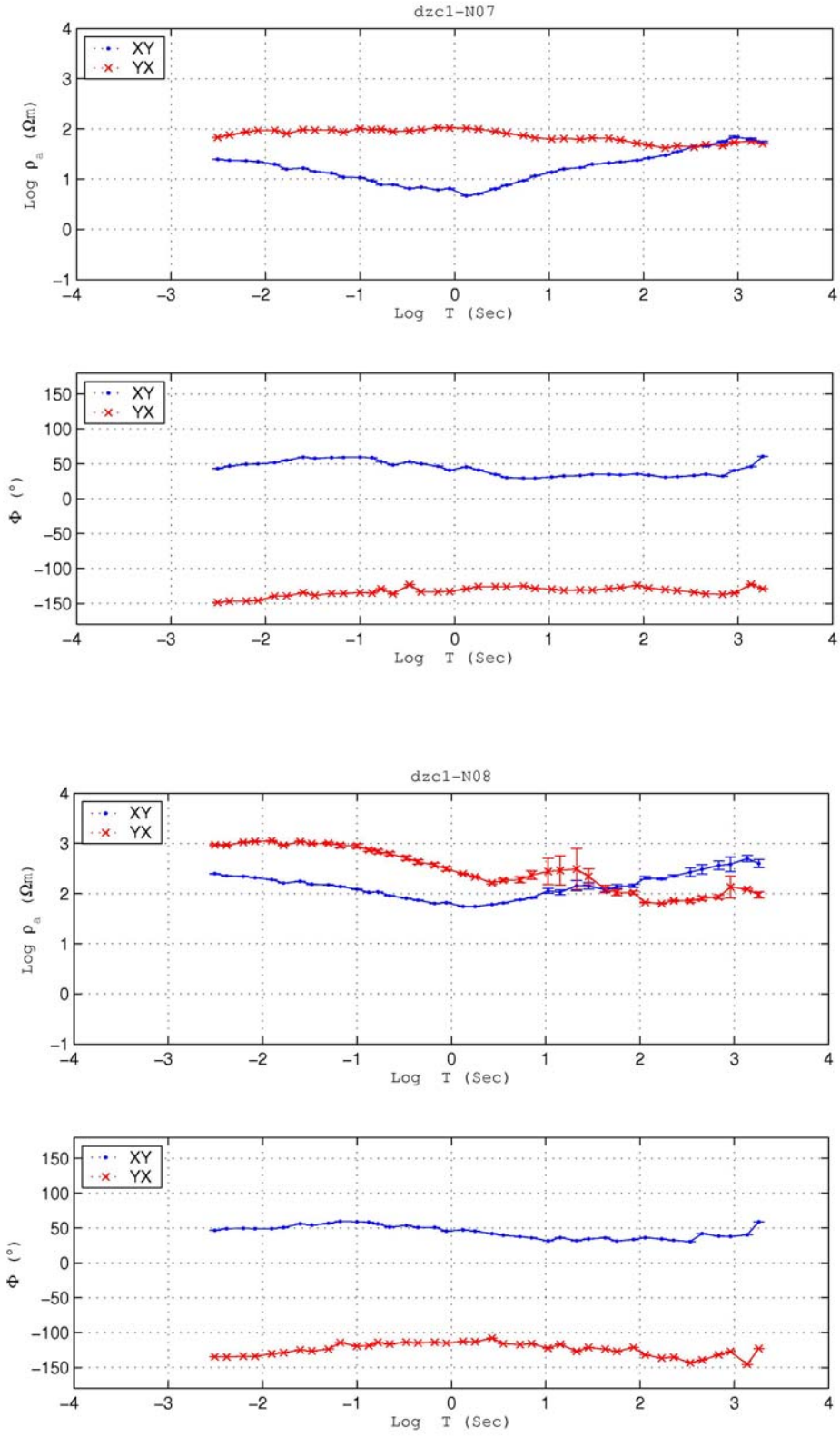

Figure A.4. Apparent resistivity and phase curves before decomposition and rotation for the stations Dzc1-N07 and Dzc1-N08 of the DW profile, respectively.

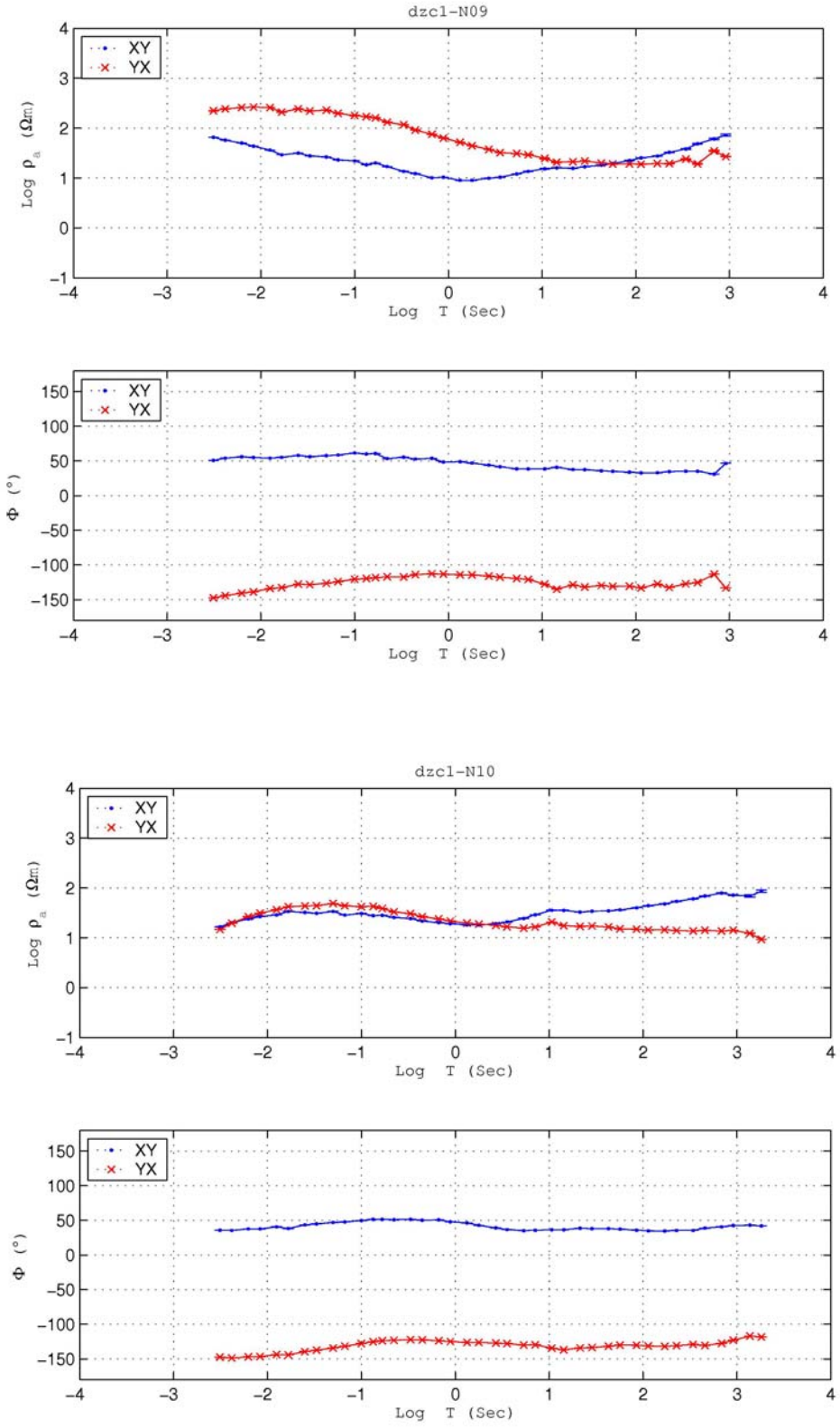

Figure A.5. Apparent resistivity and phase curves before decomposition and rotation for the stations Dzc1-N09 and Dzc1-N10 of the DW profile, respectively.

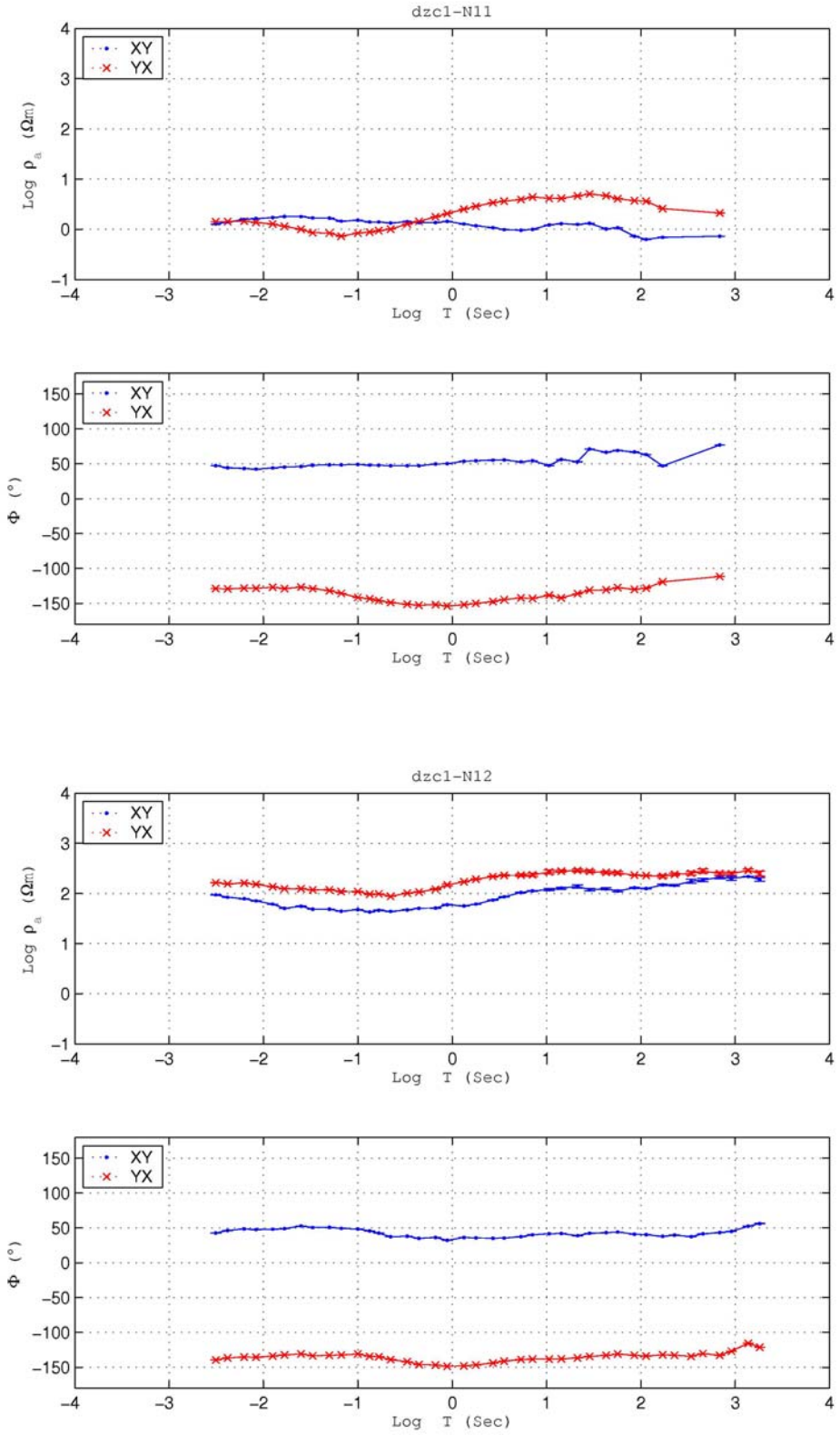

Figure A.6. Apparent resistivity and phase curves before decomposition and rotation for the stations Dzc1-N11 and Dzc1-N12 of the DW profile, respectively.

APPENDIX B: APPARENT RESISTIVITY AND PHASE CURVES OF THE WEST PROFILE AFTER GB DECOMPOSITION

The following pages (100-105) denote the apparent resistivity and phase curves of the west (DW) profile after decomposition and rotation. Figure in this part have the same representation with the figures given for the apparent resistivity and phase curves before decomposition in Appendix A. TE and TM mode apparent resistivity and phase curves are indicated with doth and cross symbols, respectively.

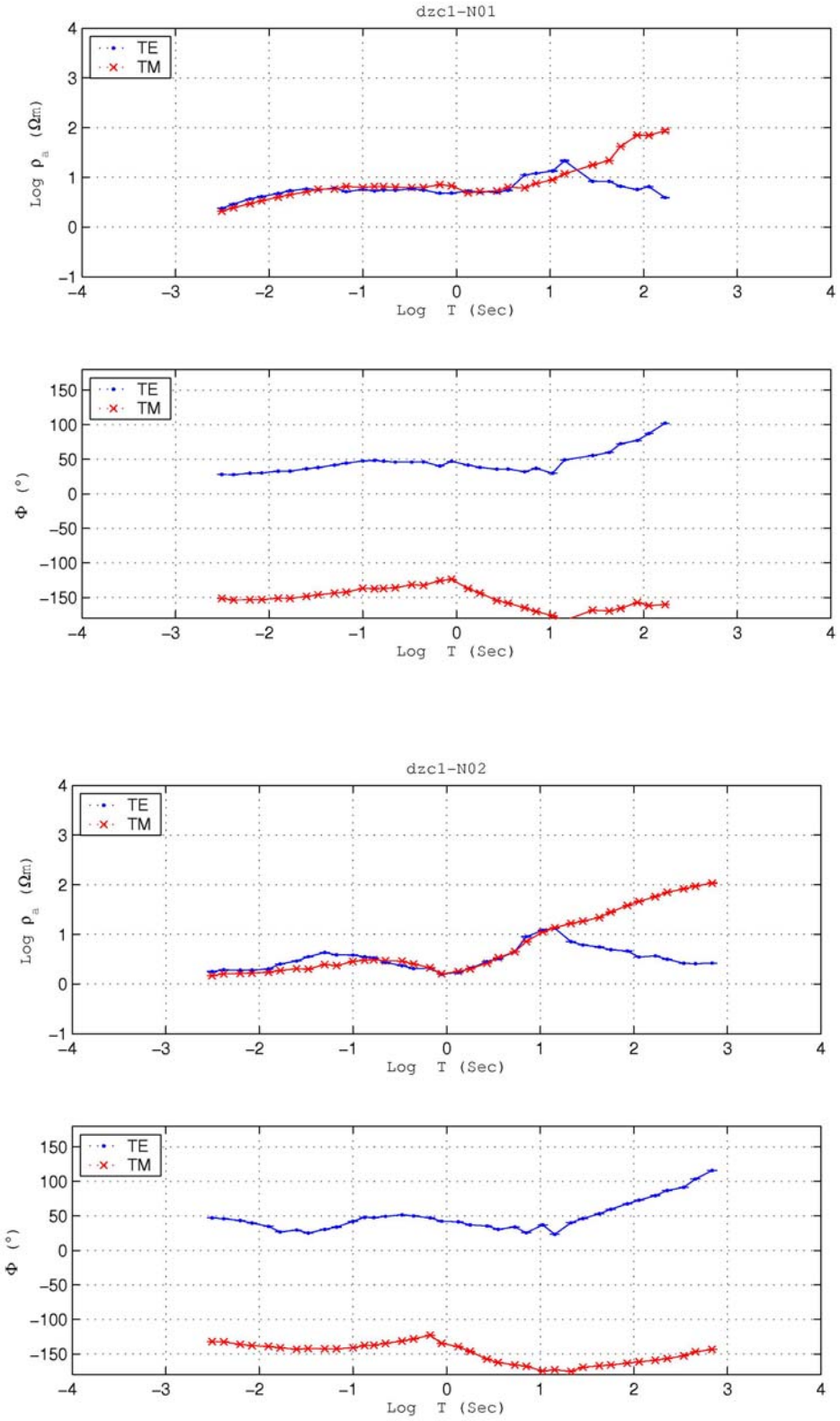

Figure B.1. Apparent resistivity and phase curves after decomposition and rotation for the stations Dzc1-N01 and Dzc1-N02 of the DW profile, respectively.

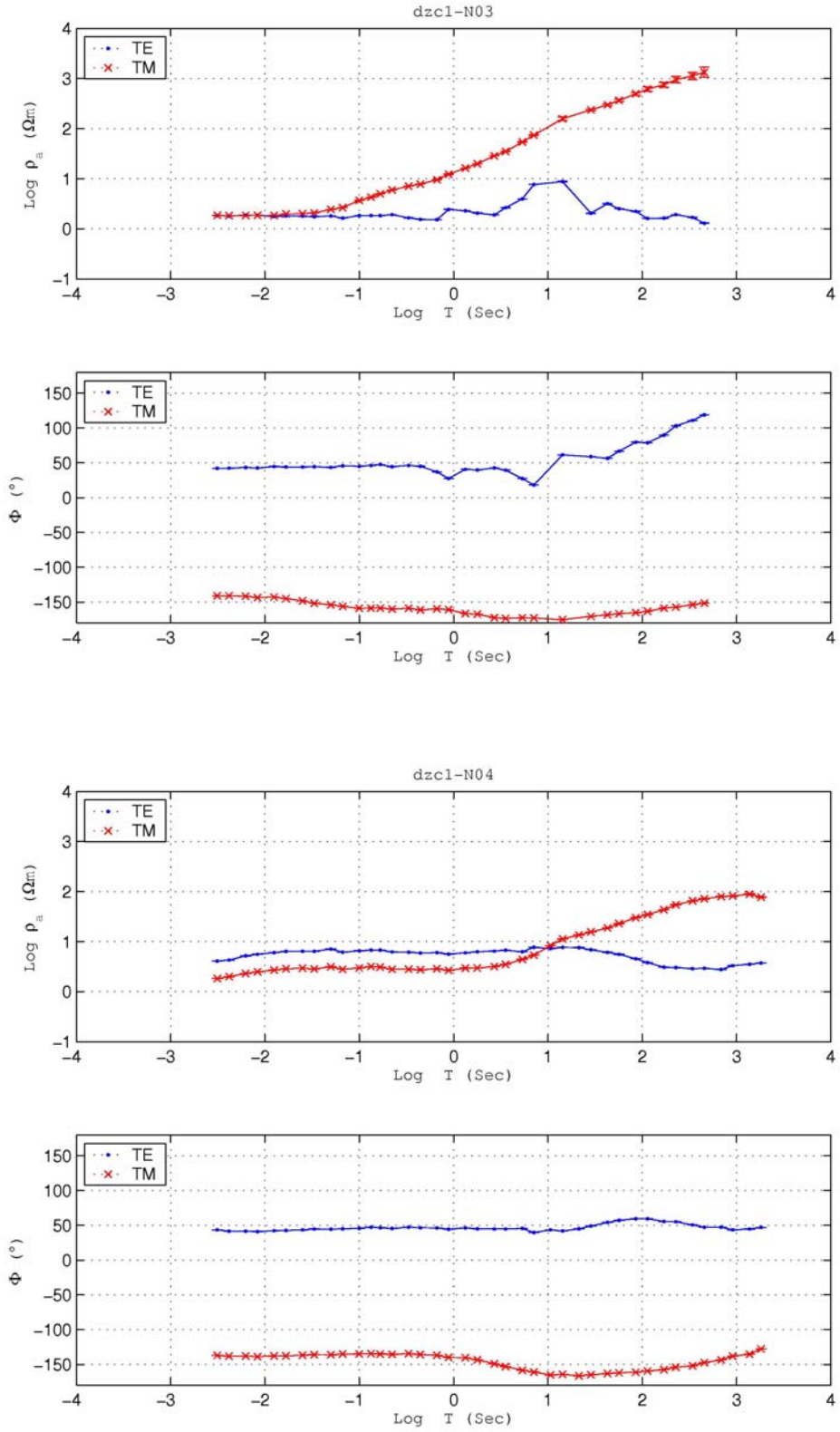

Figure B.2. Apparent resistivity and phase curves after decomposition and rotation for the stations Dzc1-N03 and Dzc1-N04 of the DW profile, respectively.

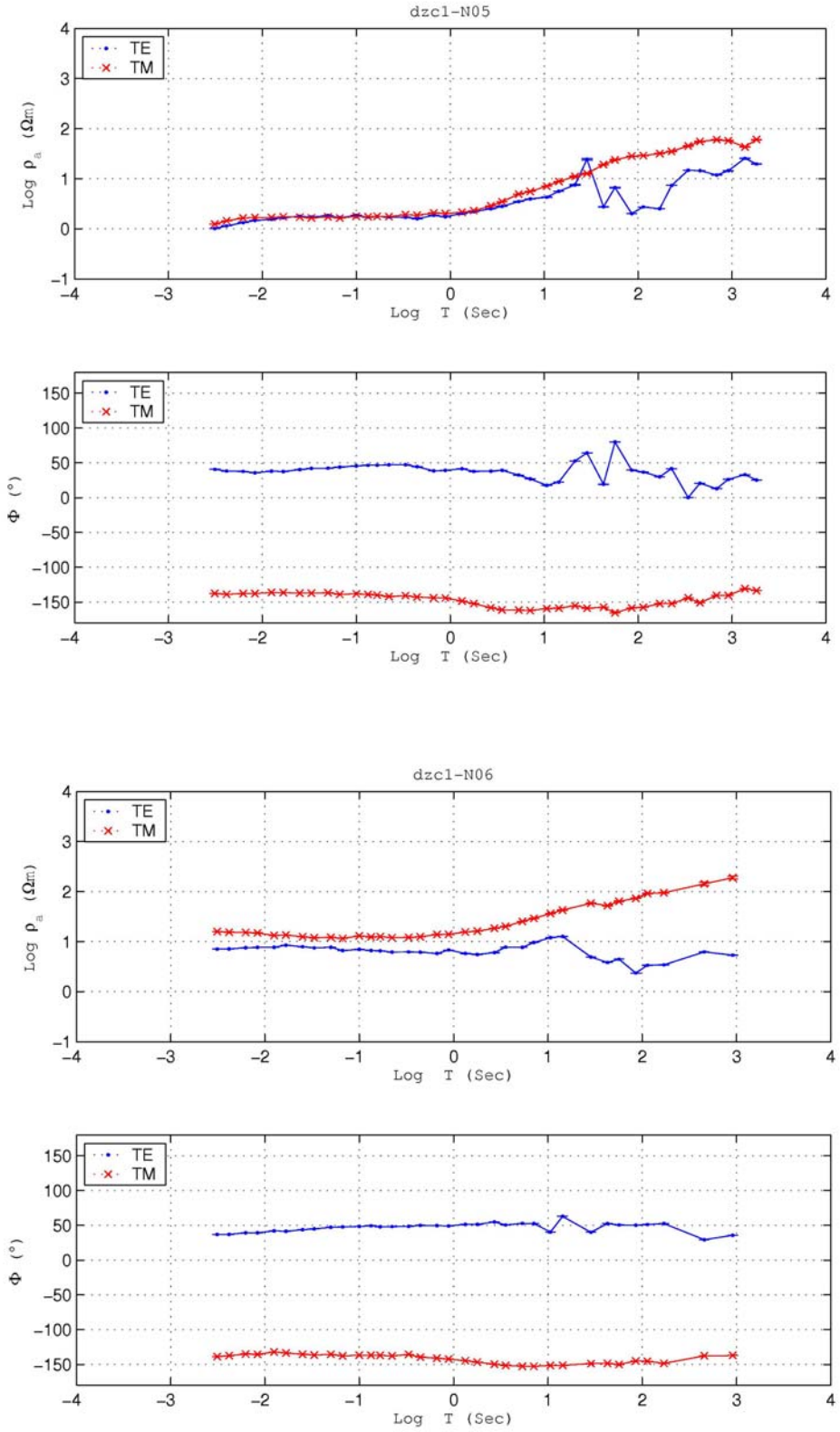

Figure B.3. Apparent resistivity and phase curves after decomposition and rotation for the stations Dzc1-N05 and Dzc1-N06 of the DW profile, respectively.

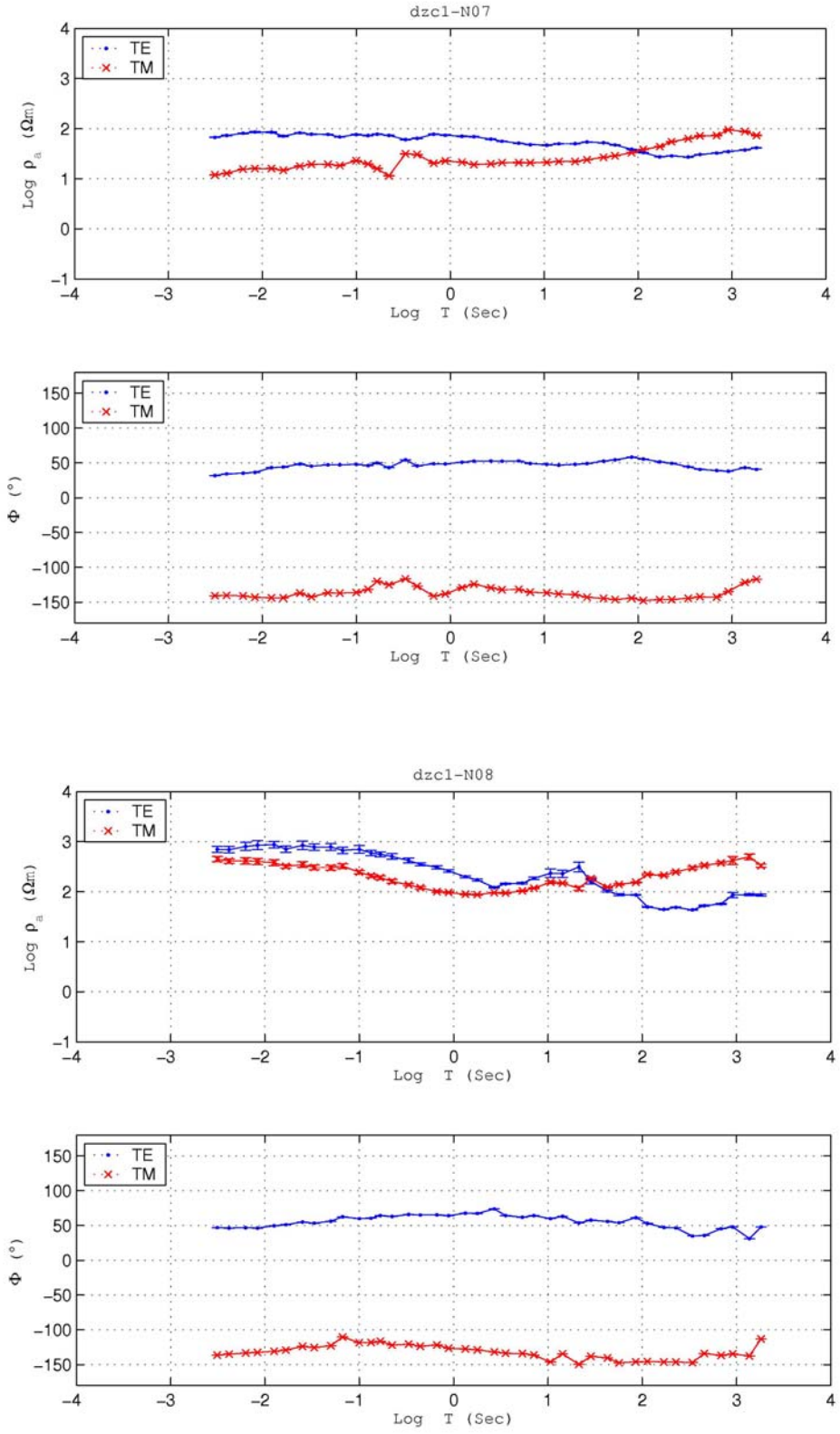

Figure B.4. Apparent resistivity and phase curves after decomposition and rotation for the stations Dzc1-N07 and Dzc1-N08 of the DW profile, respectively.

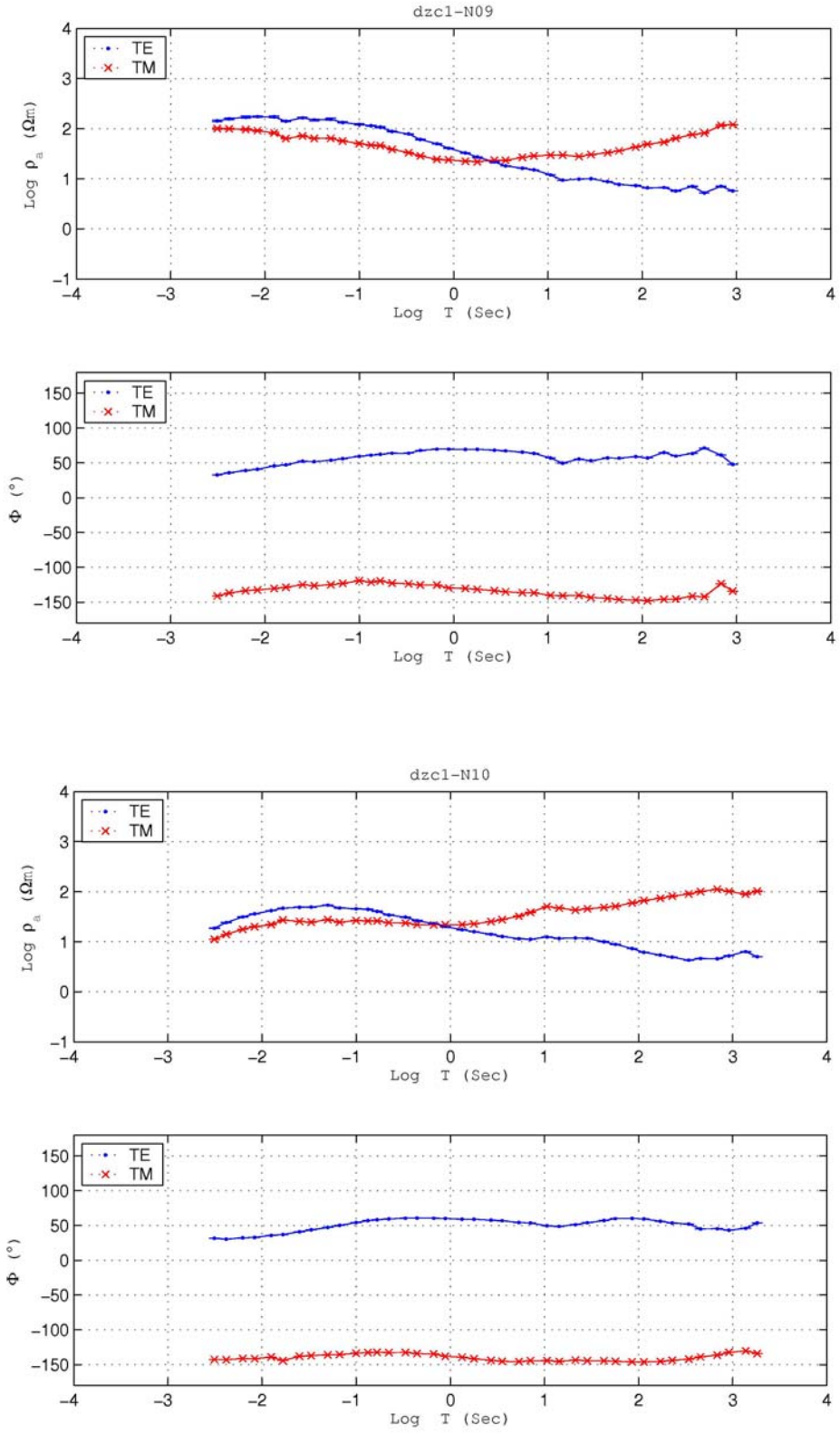

Figure B.5. Apparent resistivity and phase curves after decomposition and rotation for the stations Dzc1-N09 and Dzc1-N10 of the DW profile, respectively.

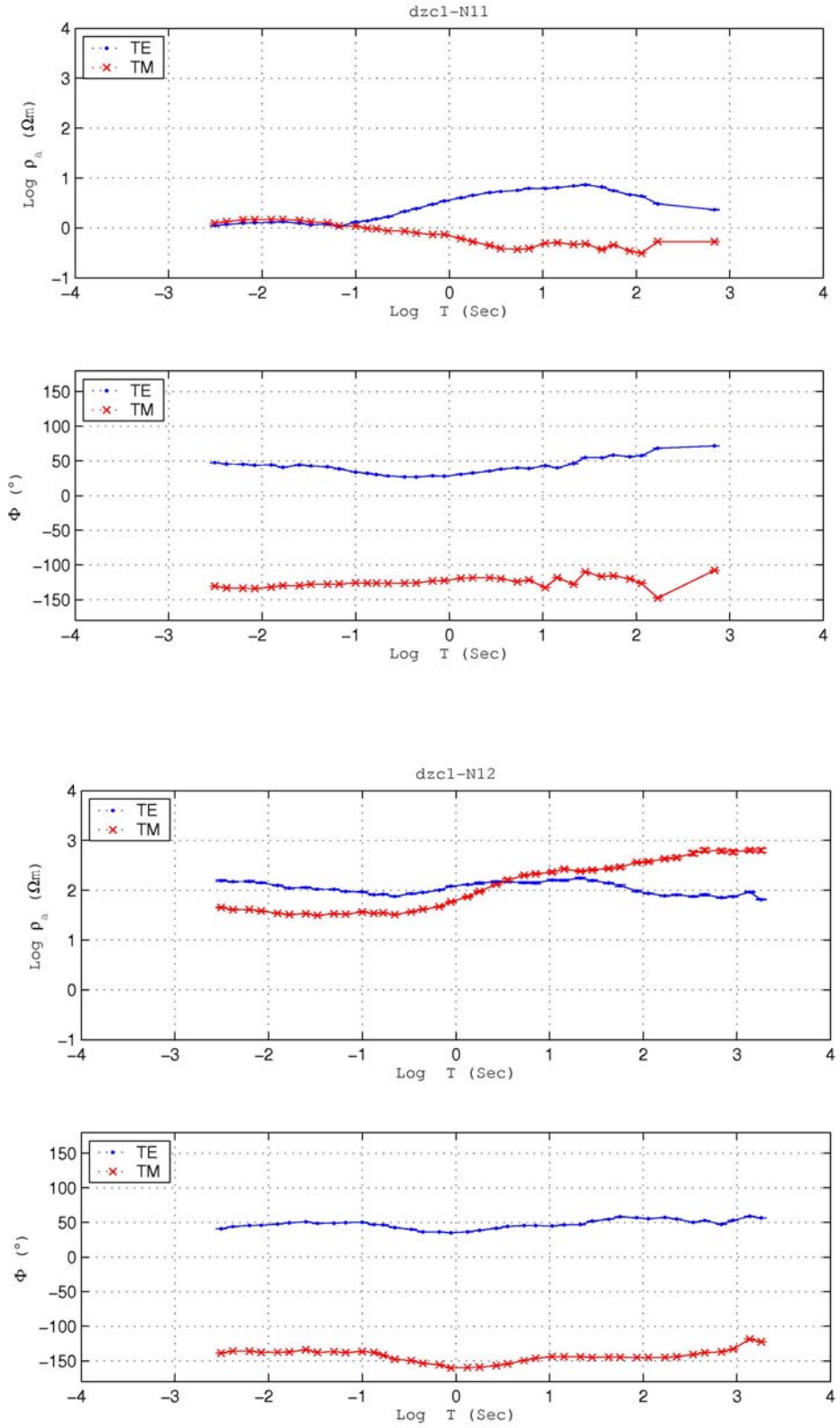

Figure B.6. Apparent resistivity and phase curves after decomposition and rotation for the stations Dzc1-N11 and Dzc1-N12 of the DW profile, respectively.

APPENDIX C: APPARENT RESISTIVITY AND PHASE CURVES OF THE EAST PROFILE BEFORE G&B DECOMPOSITION

The following pages (107-112) denote the apparent resistivity and phase curves of the east (DE) profile before decomposition and rotation. In figures, site names are termed according to station numbers in the profile from the north to the south as performed in Appendix A and B. For instance, Dzc2-N01 represents the northernmost station of the DE profile. Dzc is the abbreviation of Düzce and number 2 following the abbreviation means that this is the second, in other words the DE profile. XY and YX mode apparent resistivity and phase curves are indicated with doth and cross symbols, respectively.

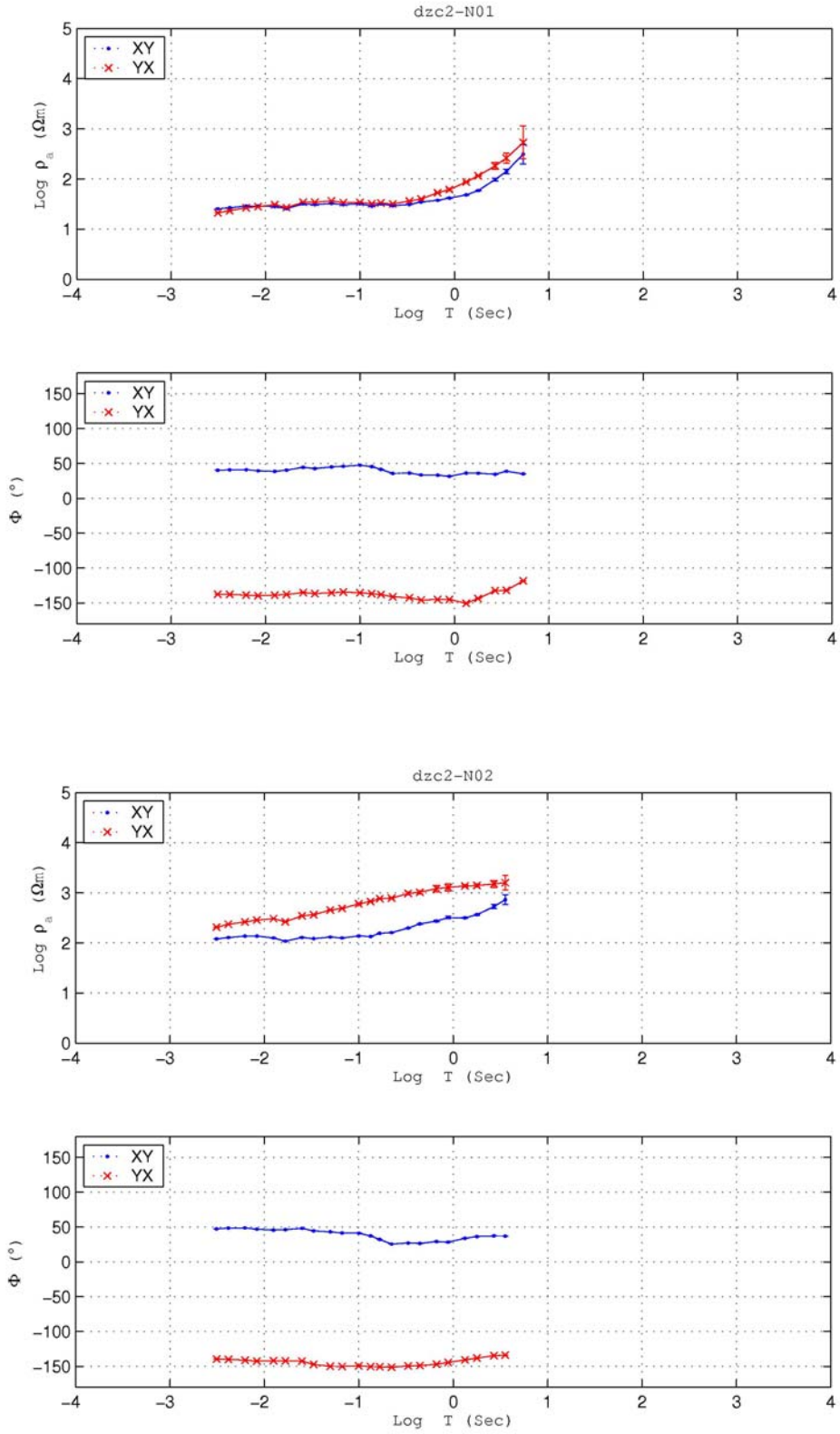

Figure C.1. Apparent resistivity and phase curves before decomposition and rotation for the stations Dzc2-N01 and Dzc2-N02 of the DE profile, respectively.

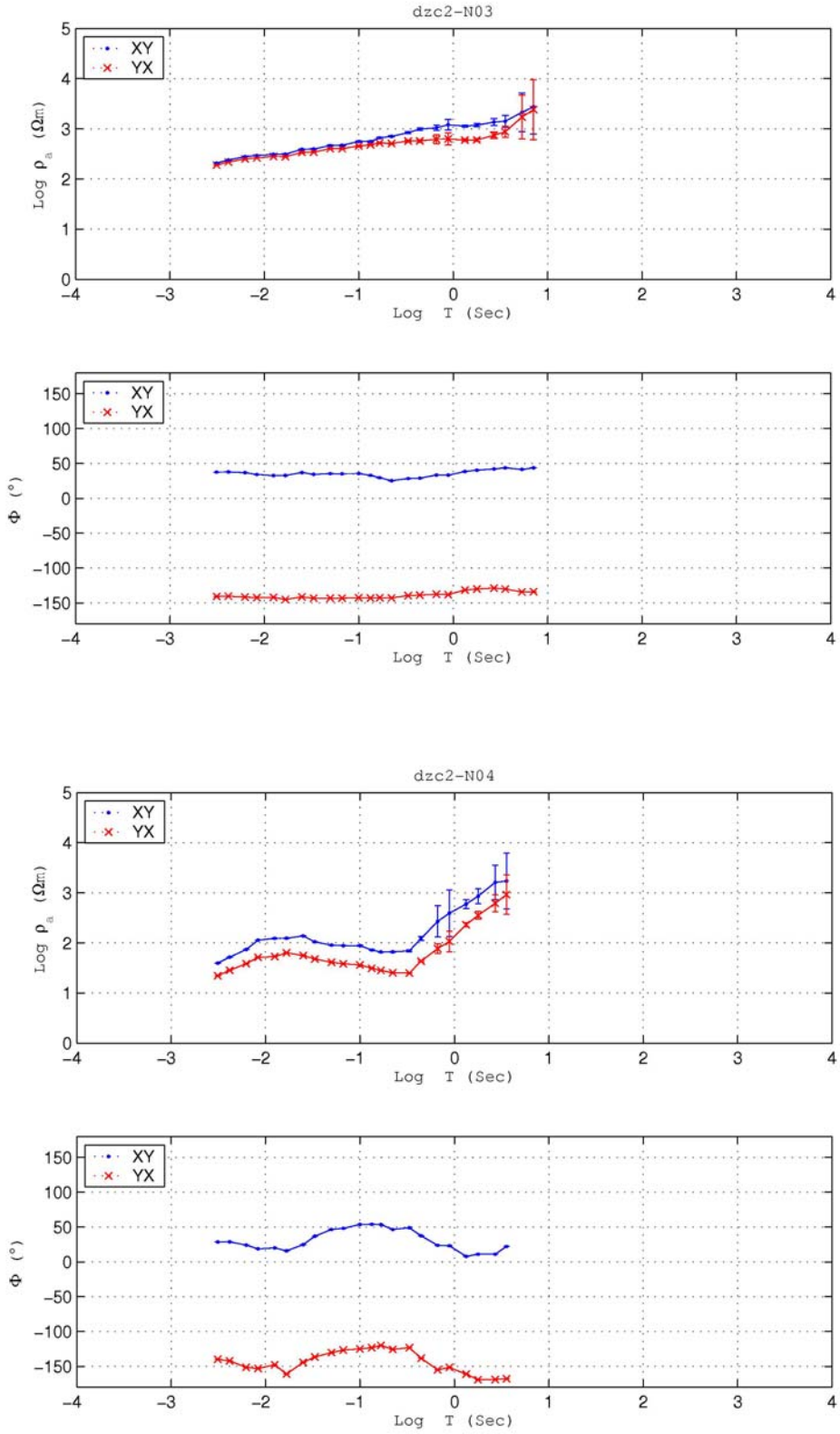

Figure C.2. Apparent resistivity and phase curves before decomposition and rotation for the stations Dzc2-N03 and Dzc2-N04 of the DE profile, respectively.

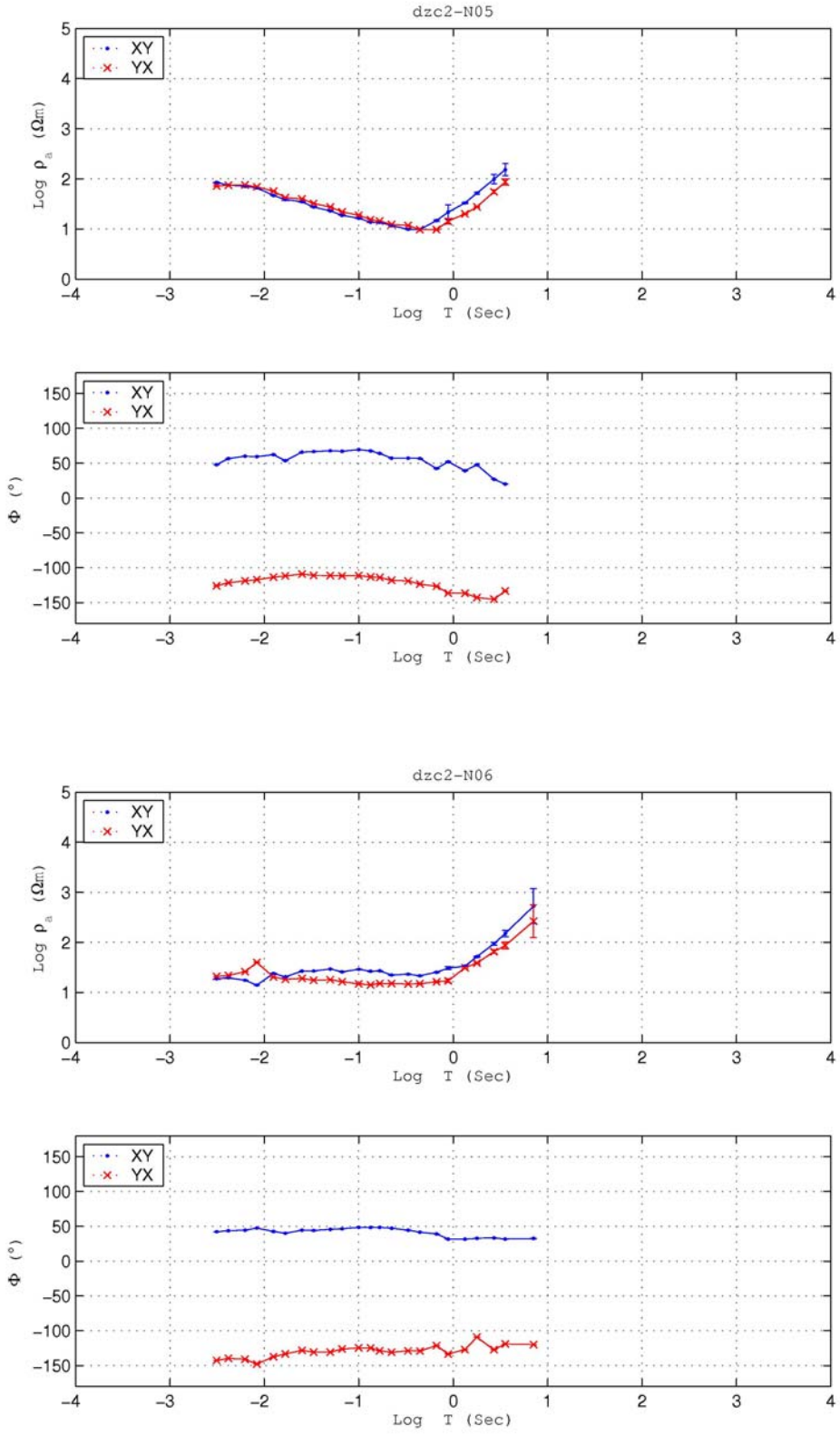

Figure C.3. Apparent resistivity and phase curves before decomposition and rotation for the stations Dzc2-N05 and Dzc2-N06 of the DE profile, respectively.

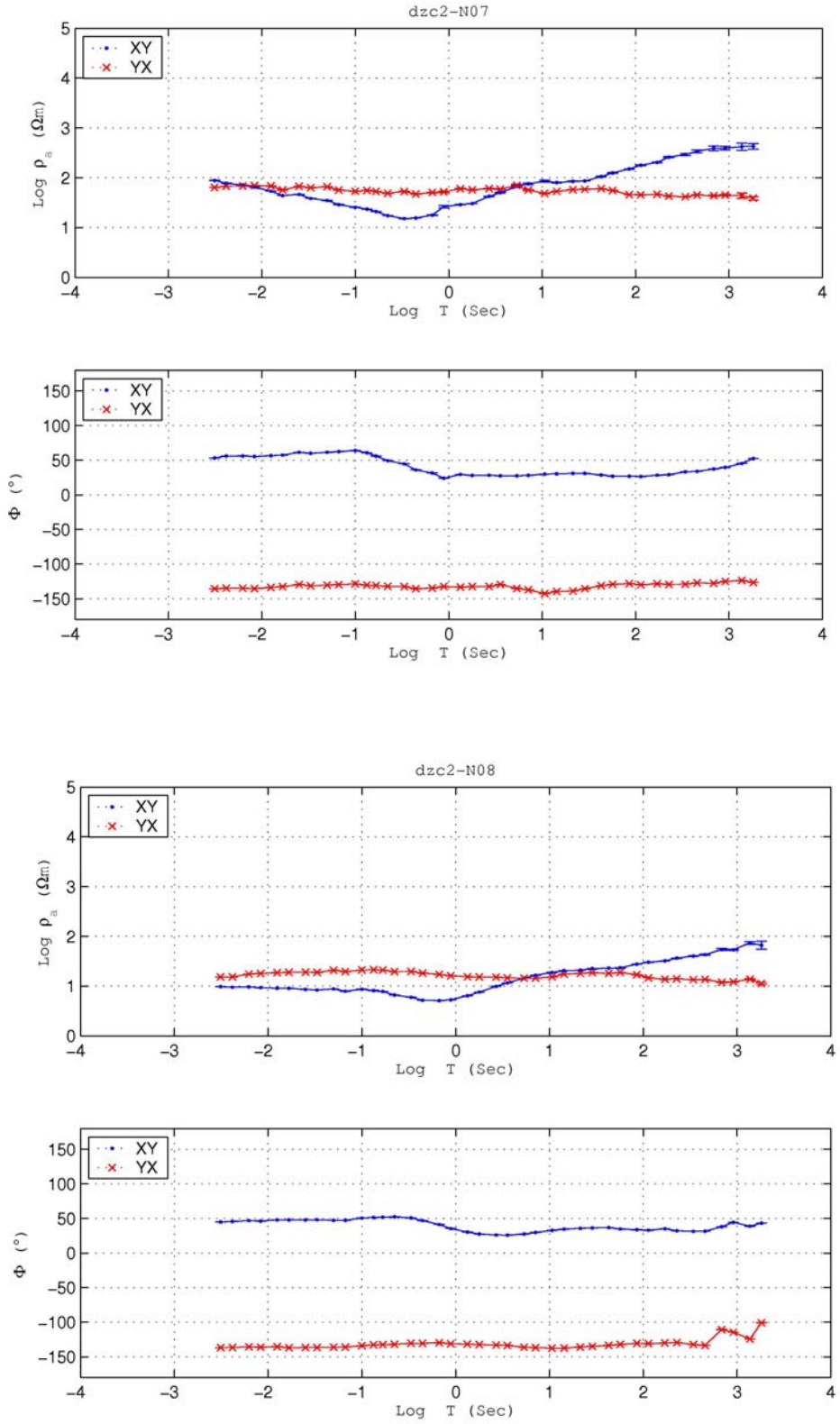

Figure C.4. Apparent resistivity and phase curves before decomposition and rotation for the stations Dzc2-N07 and Dzc2-N08 of the DE profile, respectively.

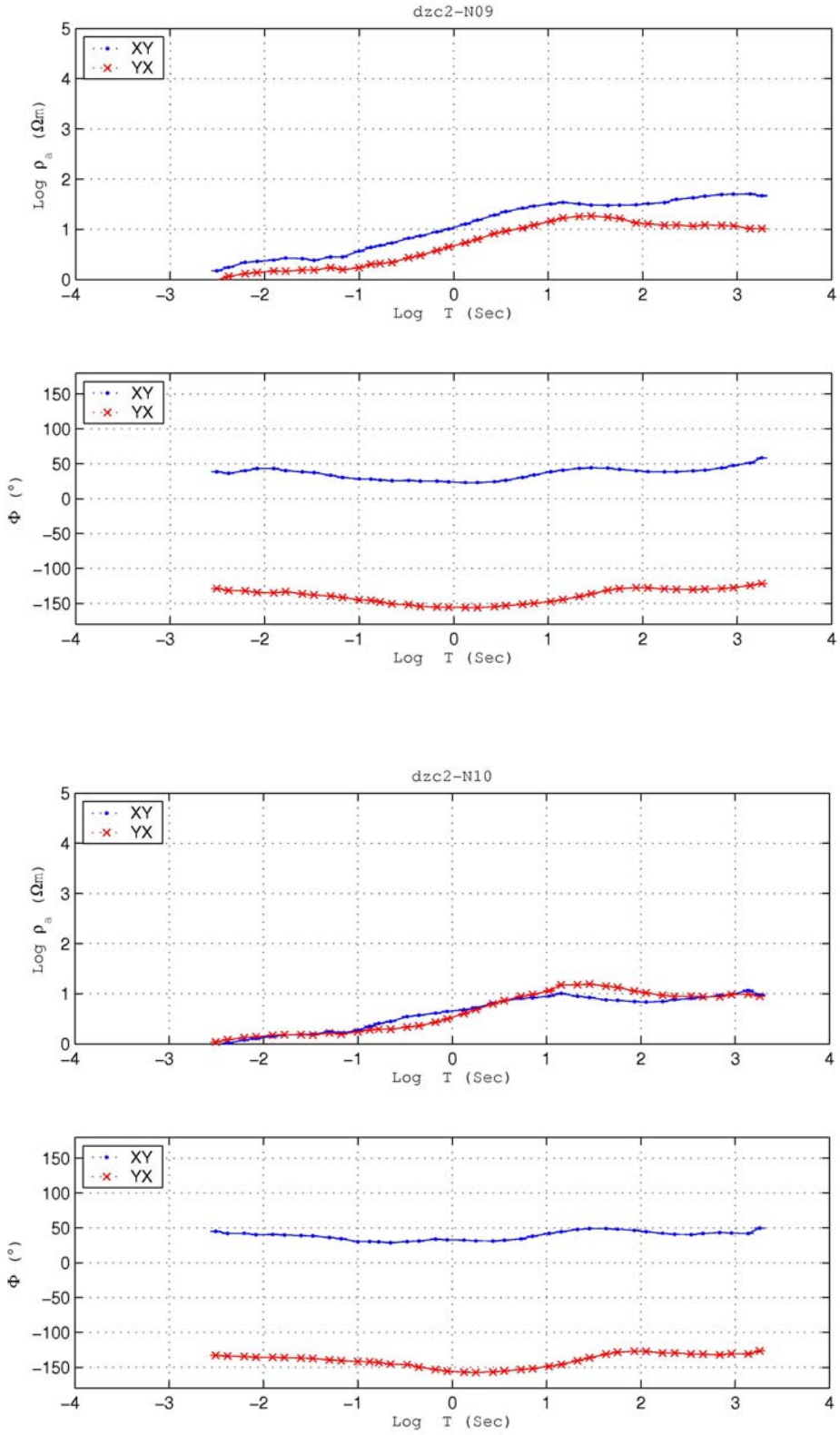

Figure C.5. Apparent resistivity and phase curves before decomposition and rotation for the stations Dzc2-N09 and Dzc2-N10 of the DE profile, respectively.

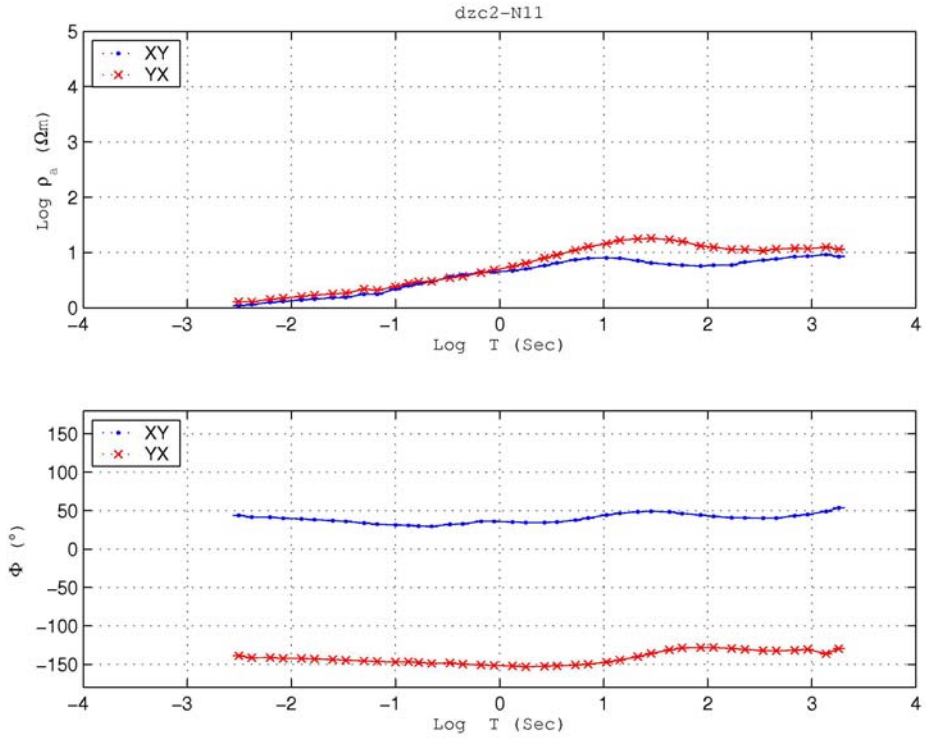

Figure C.6. Apparent resistivity and phase curves before decomposition and rotation for the station Dzc2-N11 of the DE profile.

APPENDIX D: APPARENT RESISTIVITY AND PHASE CURVES OF THE EAST PROFILE AFTER GB DECOMPOSITION

The following pages (114-119) denote the apparent resistivity and phase curves of the east (DE) profiles after decomposition. Figure in this part have the same representation with the figures given Appendix C. TE and TM mode apparent resistivity and phase curves are indicated with doth and cross symbols, respectively.

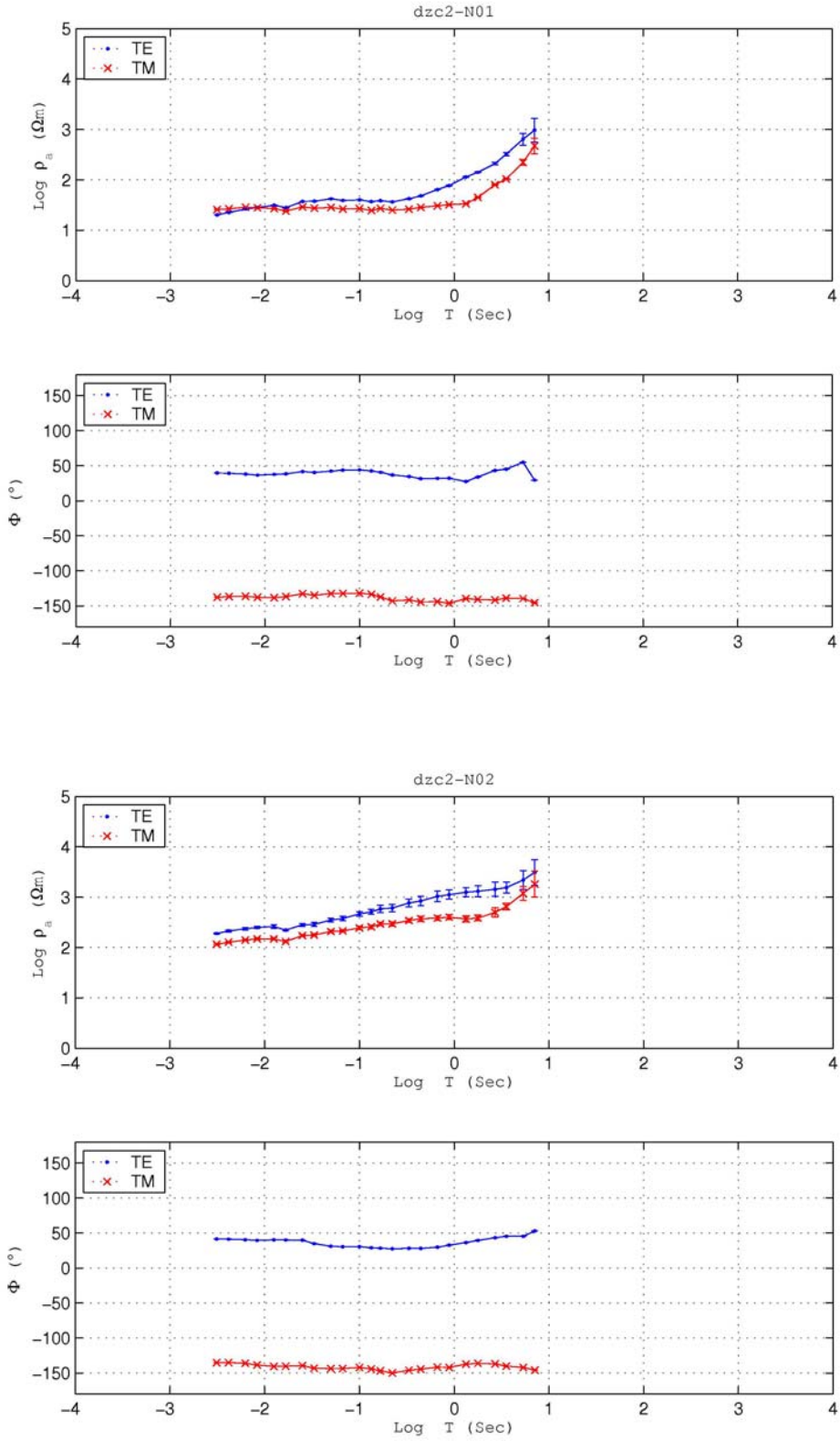

Figure D.1. Apparent resistivity and phase curves after decomposition and rotation for the stations Dzc2-N01 and Dzc2-N02 of the DE profile, respectively.

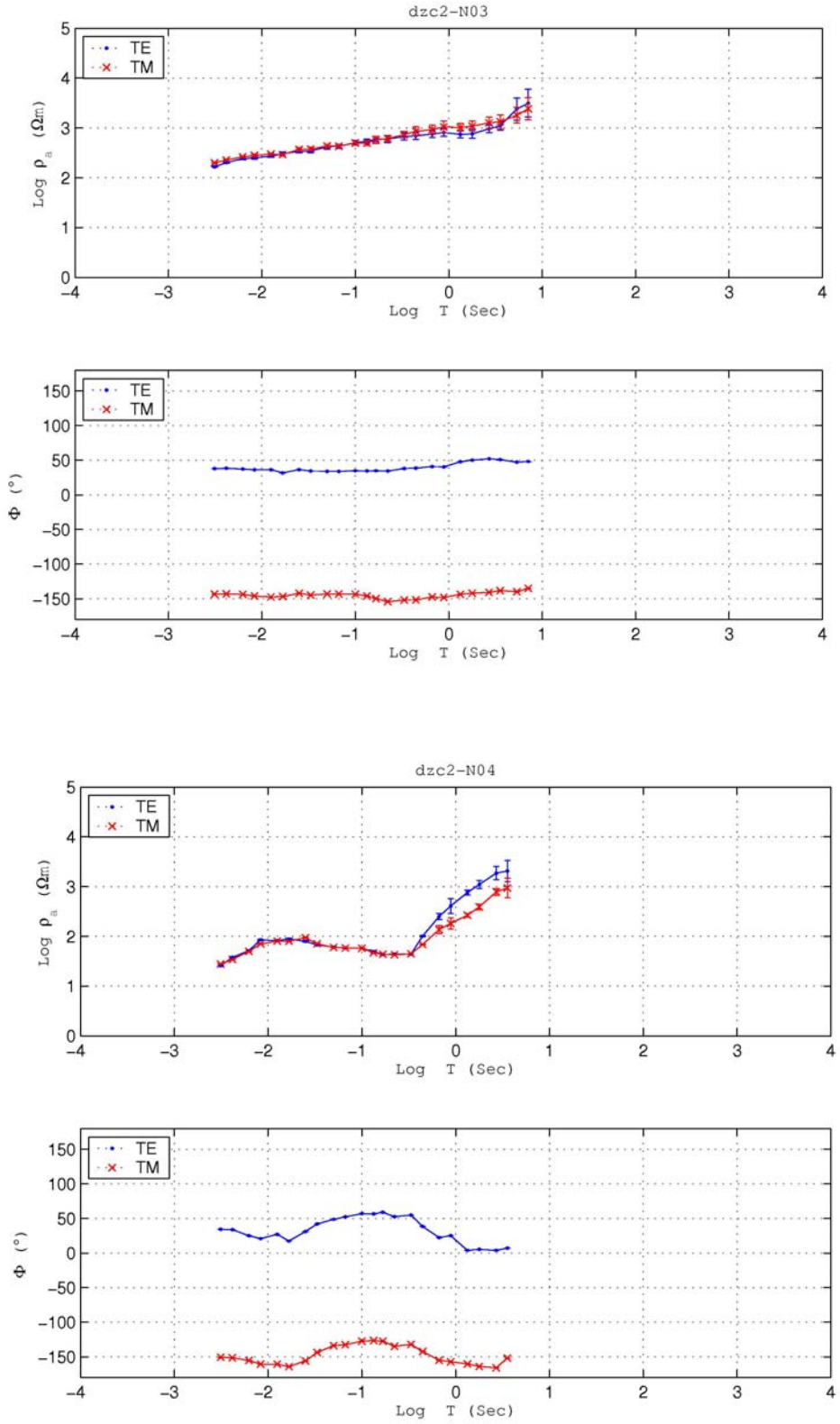

Figure D.2. Apparent resistivity and phase curves after decomposition and rotation for the stations Dzc2-N03 and Dzc2-N04 of the DE profile, respectively.

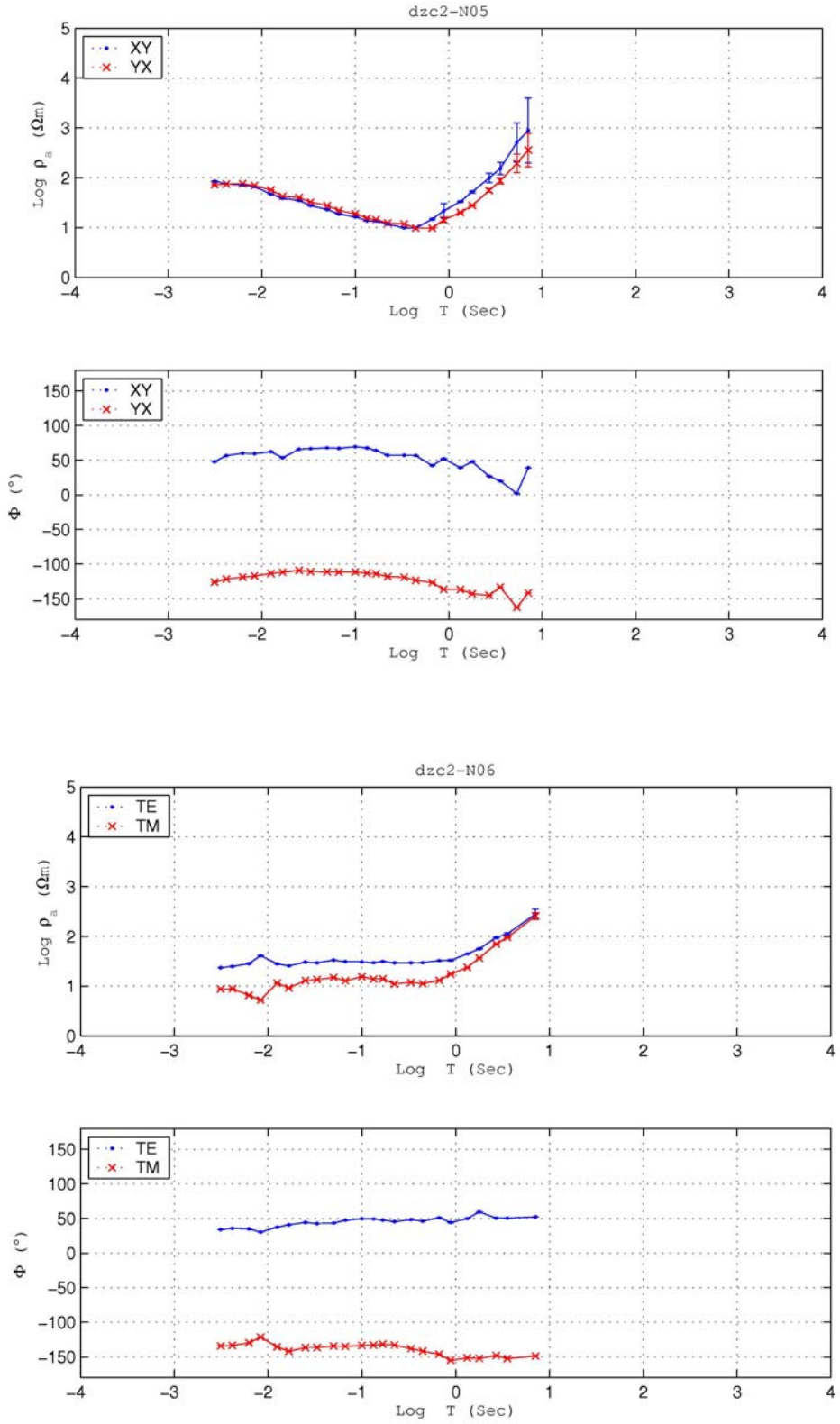

Figure D.3. Apparent resistivity and phase curves after decomposition and rotation for the stations Dzc2-N05 and Dzc2-N06 of the DE profile, respectively.

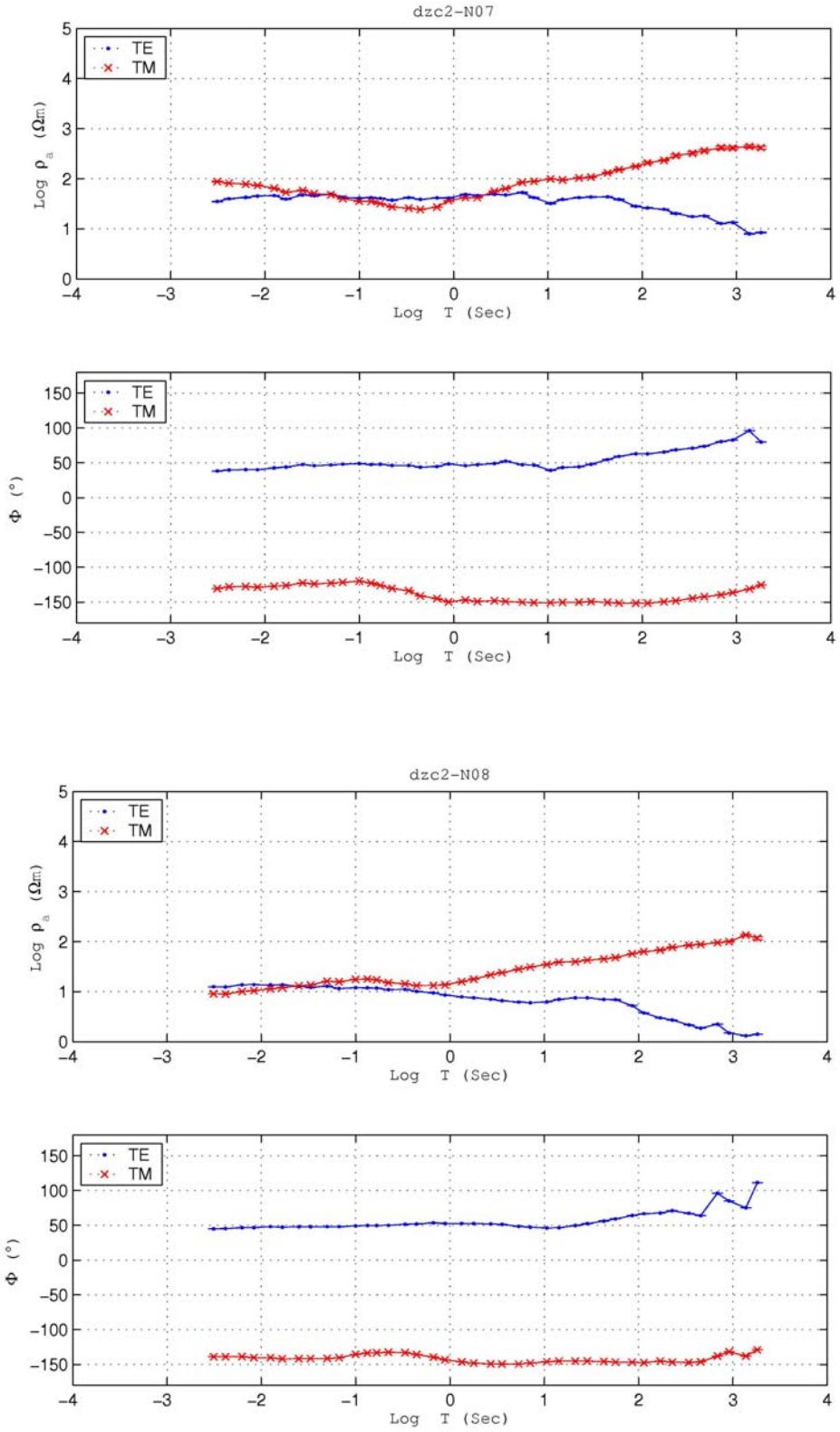

Figure D.4. Apparent resistivity and phase curves after decomposition and rotation for the stations Dzc2-N07 and Dzc2-N08 of the DE profile, respectively.

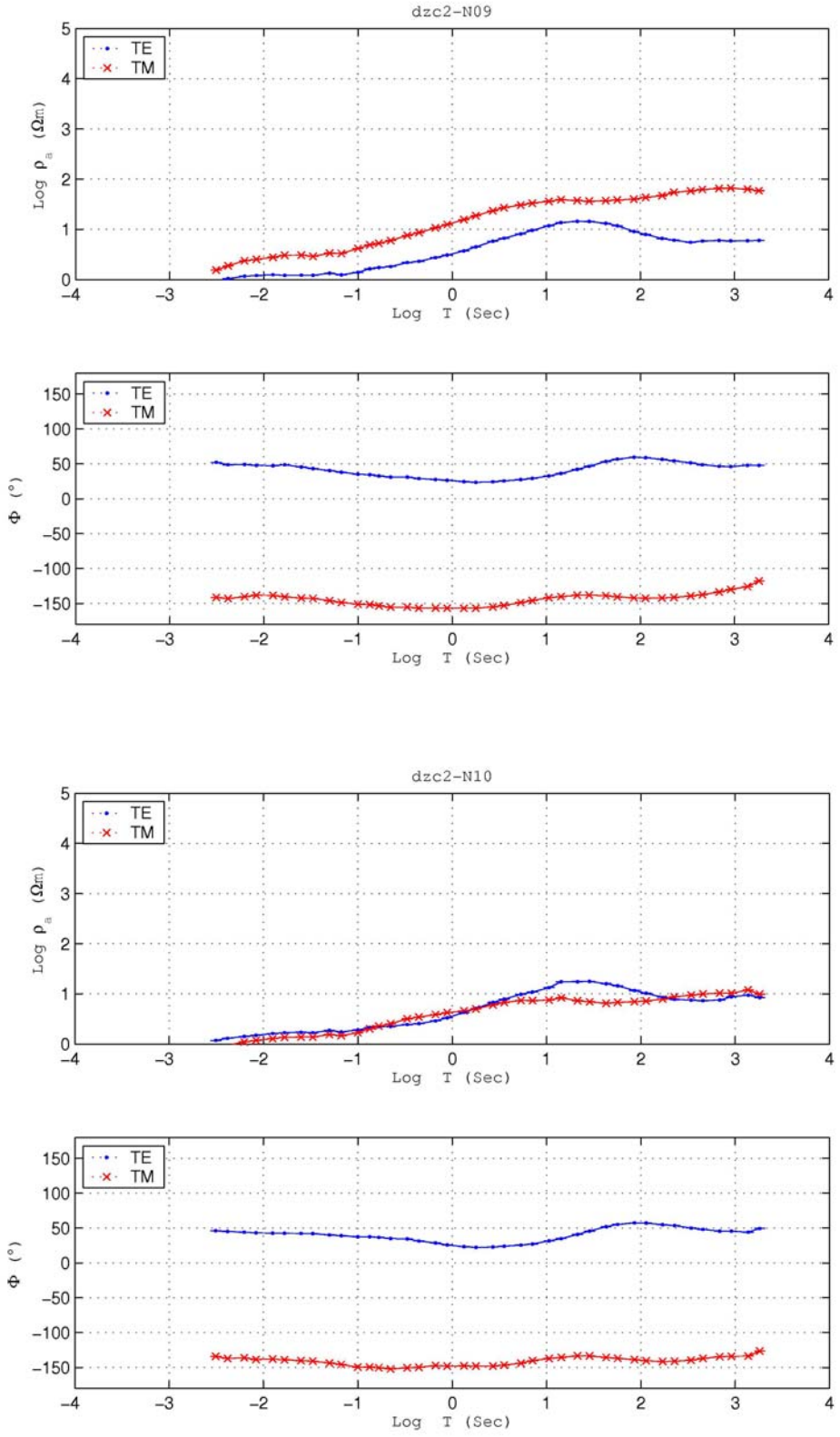

Figure D.5. Apparent resistivity and phase curves after decomposition and rotation for the stations Dzc2-N09 and Dzc2-N10 of the DE profile, respectively.

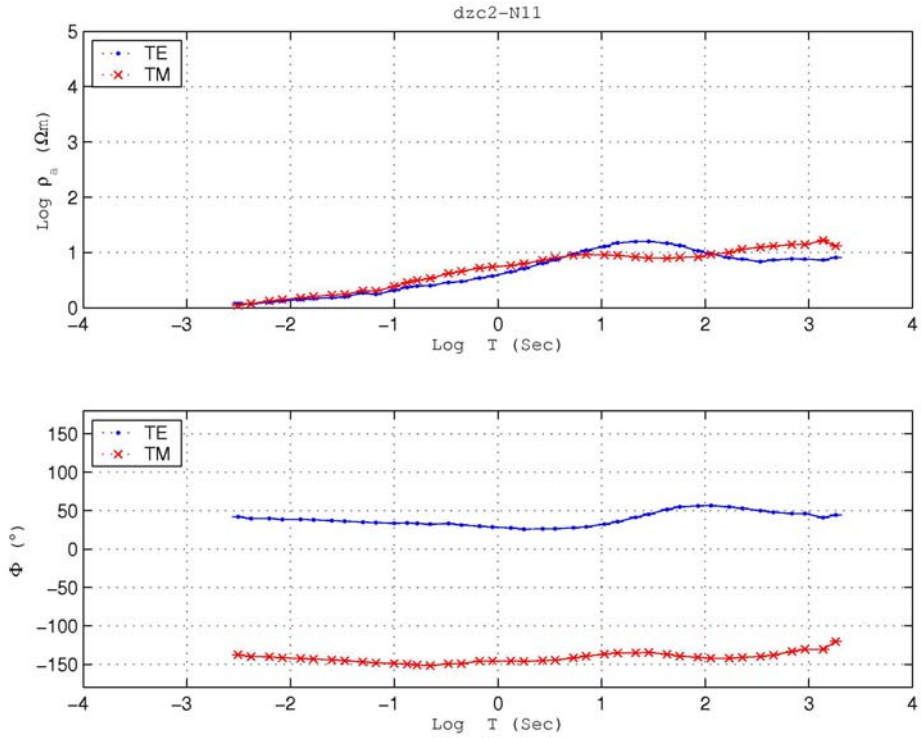

Figure D.6. Apparent resistivity and phase curves after decomposition and rotation for the station Dzc2-N11 of the DE profile.

REFERENCES

Aizawa, K., R. Yoshimura, N. Oshiman, K. Yamazaki, T. Uto, Y. Ogawa, S. B. Tank, W. Kanda, S. Sakanaka, Y. Furukawa, T. Hashimoto, M. Uyeshima, T. Ogawa, I. Shiozaki, T. Hurst, 2005, "Hydrothermal system beneath Mt. Fuji volcano inferred from magnetotellurics and electric self-potential", *Earth Planet. Sci. Lett.*, 235, 343-355.

Akyüz, H. S., R. Hartleb, A. Barka, E. Altunel, G. Sunal, B. Meyer, ve R. Armijo, 2002, "Surface Rupture and Slip Distribution of the 12 November 1999 Düzce Earthquake (*M* 7.1), North Anatolian Fault, Bolu, Turkey", *Bull. Seism. Soc. Am.*, 92, 1, 61–66.

Archie, G.E., 1942, "The electric resistivity log as an aid in determining some reservoir characteristics" *Trans. Am. Inst. Min. Metall. Petr.* Eng., 146, 54-62.

Arpat, E., E. Herece, T. Komut, N. Özgül, "*12 Kasım 1999 Düzce Depremi Ilk 3 Günlük Jeolojik Saha Verilerinin Ön Değerlendirilmesi*", http://193.140.203.16/duzce/duzce.html

Ayhan M. E, R. Bürgman, S. McClusky, O. Lenk, B. Aktug, E. Herece, and R. E. Reilinger, 2001, "Kinematics of the Mw = 7.2, 12 November 1999, Düzce, Turkey earthquake", *Geophys. Res. Lett.*, 28 (2), 367-370.

Bahr, K., 1988, Interpretation of the magnetotelluric impedance tensor: regional induction and local telluric distortion. *J. Geophys.*, 62:119–127.

Bahr, K., 1991, "Geological noise in magnetotelluric data: a classification of distortion types*", Phys. Earth Planet. Inter.*, 66:24–38.

Berdichevsky, M.N., and V.I., Dmitriev, 1976, "Distortions of magnetic and electrical fields by near surface inhomogeneities", *Acta Geodaet. Geophys. Et Mantanist. Acad. Sci. Hung.*, 11, 447-483.

Birgören, G., H. Sekiguchi, and K. Irikura, 2004, "Rupture model of the 1999 Düzce, Turkey, earthquake deduced from high and low frequency strong motion data", *Geophys. Res. Lett*., 31, L05610.

Bouin, M. P., M. Bouchon, H. Karabulut, and M. Aktar, 2004, "Rupture process of the 1999 November 12 Düzce (Turkey) earthquake deduced from strong motion and Global Positioning System measurements", *Geophys. J. Int.*, 159, 207-211.

Bouchon, M., M. P. Bouin, H. Karabulut, M. N. Toksöz, M. Dietrich, and A. J. Rosakis, 2001, "How fast is Rupture during an earthquake? New Insights from the 1999 Turkey earthquakes", *Geophys. Res. Lett*., 28 (14), 2723-2726.

Bozkurt, E., 2001, "Neotectonics of Turkey – a synthesis", *Geodinamica Akta*, 14, 3-30.

Cagniard, L., 1953, "Basic theory of the magnetotelluric method in geophysical prospecting", *Geophysics*, 18, 605-635.

Caldwell, T. G., 2004, "The magnetotelluric phase tensor", *Geophys. J. Int.,*158, 457-469.

Cantwell, T., 1960, "Detection and analysis of low frequency magnetotelluric signals", *Phd. Thesis*, *Mass. Inst. Tech*.

Chave, A.D., and T.J. Smith, 1994, "On electric and magnetic galvanic distortion tensor decompositions", *J. geophys. Res*. 99, 4669-4682.

Constable, S. C., A. S. Orange*z*, G. M. Hoversten, and H. F. Morrison, 1998, "Marine magnetotellurics for petroleum exploration", *Part I: A sea-floor equipment system*, *Geophysics*, 63 (3), 816–825.

Çağlar, I. and T. İşseven, 2004, "Two-dimensional geoelectrical structure of the Göynük geothermal area, northwest Anatolia, Turkey", *J. Volcano. Geotherm. Res.*, 134, 183-197.

Çakır Z., A. A. Barka, J. B. De Chabalier, R. Armijo, B. Meyer, 2003, "Kinematics of the November 12, 1999 (Mw=7.2) Düzce Earthquake Deduced from SAR Interferometry", *Turkish Journal of Earth Sciences (Turkish J. Earth Sci.)*, 12, 105-118.

Gamble, T.D., W.M., Goubau, and J., Clark, 1979, "Magnetotelluric with a remote magnetic reference", *Geophysics*, 44, 53-68.

Groom, R.W., and, R.C. Bailey, 1989, "Decomposition of magnetotelluric impedance tensor in the presence of local three-dimensional galvanic distortion", *J. Geophys. Res*., 94, 1913-1925.

Gürer, A., 1996, "Deep conductivity structure of the North Anatolian fault zone and the Istanbul and Sakarya Zones along the Gölpazarı-Akçaova profile, northwest Anatolia", *International Geology Review*, 38, 727-736.

Haak V., and Hutton V. R. S., 1986, "Electrical resistivity in continental lower crust", *The nature of the Lower Continental Crust*, 24, 35-49.

Hickman, S., 1995, "Introduction to special section: Mechanical involvement of fluids in faulting", *J. Geophys. Res*., 100, B7, 12.831-12.840.

Hitchcock, C., E. Altunel, A. Barka, J. Bachhuber, W. Lettis, Ö. Kozacı, J. Helms, and S. Lindvall, 2003, "Timing of Late Holocene Earthquakes on the Eastern Düzce Fault and Implications for Slip Transfer between the Southern and Northern Branchs of the North Anatolian Fault System, Bolu, Turkey", *Turkish Journal of Earth Sciences (Turkish J. Earth Sci.)*, 12, 119-136.

Jiracek, J., 1990, “Near surface and topographic distortions in electromagnetic induction”, *Surv. Geophys.*, 11, 163-203.

Jones, , A. G., 1986, “Parkinson's pointers' potential perfidy!”, *Geophysical Journal of the Royal Astronomical Society*, 87, 1215-1224.

Jones, A. G., 1988, “Static shift of magnetotelluric data and its removal in a sedimentary basin environment”, *Geophysics*, 53, 967-978.

Jones, A. G., 1999, “Imaging the continental upper mantle using electromagnetic methods”, *Lithos*, 48, 57–80.

Kaufman A. A. and G.V. Keller, 1981, “The magnetotelluric sounding method”, methods in geochemistry and geophysics, *Elsevier scientific publishing company*, 15.

Keller, G. V. and F. C., Frischknecht, 1970. “Electrical methods in geophysical prospecting”. *Pergamon Press, Oxford*

Key, K., and S., Constable, 2002, “Broadband Marine MT exploration of the East Pacific Rise at 9˚ 50' N”, *Geophys. Res. Lett*., 29 (22), 2054.

Larsen, J.C., 1977, “Removal of local surface conductivity effects from low frequency mantle reponse curves”, *Acta Geodaet. Geophys. Et Mantanist. Acad. Sci. Hung.*, 12, 183-186.

Ledo, J., P. Queralt, and J. Pous, 1998, “Effects of galvanic distortion on magnetotelluric data over a three-dimensional regional structure”, *Geophys. J. Int.*, 132, 2, 295.

McNeice, G.W., and A.G., Jones, 2001, “Multisite, multifrequency tensor decomposition of magnetotelluric data”, *Geophysics*, 66, 1, 158-173.

MTA, *Türkiye Jeoloji haritası*, 1999, http://www.mta.gov.tr/mta_web/500.000/image/zonguldak.asp

Ogawa, Y., and Uchida, T., 1996, "A two-dimensional magnetotelluric inversion assuming Gaussian static shift", *Geophys. J. Int.,* 126, 69-76.

Ogawa, Y., H. M. Bibby, T. G. Caldwell, S. Takakura, T. Uchida, N Matsushima, S. L. Bennie, T. Tosha, and Y. Nishi, 1999, "Wide-band magnetotelluric measurements across the Taupo Volcanic Zone, New Zealand - Preliminary Results", *Geophys. Res. Lett*., 26, 3673-3676.

Ogawa, Y., 2002, "On two dimensional modeling of magnetotelluric field data", *Surveys in Geophysics*, 23, 251-272

Okay A., A. Kaşlılar-Özcan, A. Boztepe-Güney, ve İ. Kuşçu, "Marmara depreminde İstanbul'u tehdit eden kırıklar", *Cumhuriyet Bilim Teknik*, 648/9, 1999.

Parsons, T., T. Shinji, R. S. Stein, A. Barka, and J. A. Dieterich, 2000, "Heightened odds of large Earthquakes near Istanbul: an interaction-based probability calculation", *Science*, 228, 661-665.

Reilinger, R.E., S. Ergintav, R. Burgmann, S. Mcclusky, O. Lenk, A. A. Barka, O. Gürkan, L. Hearn, K. Feigl, R. Cakmak, B. Aktu., H. Özener, & M. N. Toksöz, 2000, "Coseismic and postseismic Fault slip for the 17 August 1999, M=7.5, İzmit, Turkey Earthquake", *Science*, 289, 1519–1524.

Ritter, O., T. Ryberg, U. Weckmann, A. Hoffmann-Rothe, A. Abueladas, Z. Garfunkel, and DESERT Research Group, 2003, "Geophysical images of the Dead Sea Transform in Jordan reveal an impermeable barrier for fluid flow", *Geophys. Res. Lett*., 30 (14), 1741.

Ritter, O., A. Hoffmann-Rothe, P. A. Bedrosian, U. Weckmann and V. Haak, 2005, "Electrical conductivity images of active and fossil fault zones", *The Geological Society of Londan, special Publications,* 245, 165-186.

Simpson F., 2002, "Intensity and direction of lattice-preferred orientation of olivine: are electrical and seismic anisotropies of the Australian mantle reconcilable?", *Earth Planet. Sci. Lett.*, 203, 535-547.

Swift, C. M. Jr., 1967, "*A magnetotelluric investigation of an electrical conductivity anomaly in the south-western United States*", PhD thesis, M.I.T.

Stratton, J. A., 1941, "Electromagnetic Theory", *McGraw-Hill Book. Co*.

Şengör, A.M.C., O. Tüysüz, C. İmren, M. Sakınç, H. Eyidoğan, N. Görür, X. Le Pichon, C. Rangin, 2005, "The North Anatolian Fault: A new look, Annu. Rev.", *Earth Planet. Sci*., 33, 37-112.

Tank, S. B., Y. Honkura, Y. Ogawa, M. Matsushima, N. Oshiman, M. K. Tunçer, C. Çelik, E. Tolak, and A. M. Işıkara, 2005, "Magnetotelluric imaging of the fault rupture area of the 1999 İzmit (Turkey) earthquake", *Phys. Earth Planet. Inter*., 150, 213–225.

Tezkan, B., 1999, "A review of environmental applications of quasi-stationary electromagnetic techniques", *Surveys in Geophysics*, 20 (3-4), 279-308.

Tikhonov, A. N., 1950, "On determining electrical characteristics of he deep layers of the Earth's crust. *Doklady,* 73, 281-285.

Unsworth, M., B. Bedrosian, M. Eisel, G. Egbert and W. Siripunvaraporn, 2000, "Along strike variations in the electrical structure of the San Andreas fault at Parkfield, California", *Geophys. Res. Lett*., 27, 18, 3021-3024.

Vozoff, K., 1972, "The magnetotelluric method in the expolaration of sedimentery basins", *Geophysics*, 37, 1, 98-141.

Vozoff, K., 1991, "The magnetotelluric method", *in Nabighian, M. N., Ed., Electromagnetic methods in applied Geophysics: SEG., 2B*, 641-711.

Wannamaker, P. E. and W. M. Doerner, 2002, "Crustal structure of the Ruby Mountains and southern Carlin Trend region, Nevada, from magnetotelluric data", *Ore Geology Reviews*, 425.

Ward, Stanley H., and G. W., Hohmann, 1987, "Electromagnetic Theory for Geophysical Applications", *Electromagnetic Methods in Applied Geophysics*, 1, 130-311.

Wei, W., M. Unsworth, A. Jones, J. Booker, H. Tan, D. Nelson, L. Chen, S. Li, K. Solon, P. Bedrosian, S. Jin, M. Deng, J. Ledo, D. Kay, and B. Roberts, 2001, "Detection of widespread fluids in the Tibetan Crust by magnetotelluric studies", *Science*, 292 (5517), 716-719.

Yılmaz, Y., O. Tüysüz, E. Yiğitbaş, C. Genç, and A.M.C. Şengör, 1997, "Geology and tectonic evolution of the pontides", *In: Robinson, A. G. (ed.) Regional and Petroleum Geology of the Black Sea and surronding region. American Ass. of. Petrol. Geol., Memoirs* 68, 138-226.

Yiğitbaş, E., A. Elmas, and Y. Yılmaz, 1999, "Pre-Cenozoic tectono-stratigraphic components of the Western Pontides and their geological evolution", *Geol. J.*, 34, 55-74.